



Universidad de Guanajuato

División de Ciencias e Ingenierías

**Effect of long-range interactions in dynamic and
transport properties of liquid crystals using
DMC simulations and the reaction field method.**

T E S I S

Que para obtener el título de:

DOCTORA EN FISICA

Presenta:

DANIELA CYWIAK CORDOVA

Directores de tesis:

Dr. ALEJANDRO GIL-VILLEGAS MONTIEL

Departamento de Ingeniería Física de la Universidad de Guanajuato

Dr. ALESSANDRO PATTI

Departamento de Física Aplicada

Universidad de Granada

León, Gto.

March 2025

Thesis to obtain the: **Doctor in Physics' Degree**

Title of the work: *Effect of long-range interactions in dynamic and transport properties of liquid crystals using DMC simulations and the reaction field method.*

Author: Daniela Cywiak Córdoba

Supervisors: Dr. Alejandro Gil-Villegas Montiel and Dr. Alessandro Patti

The thesis evaluation committee selected for the evaluation of the work, conformed by the following members:

President:

Committee member:

Secretary:

Substitute:

Agrees to grant the grade of

Resumen

Las propiedades dinámicas y viscoelásticas de los sistemas coloidales son fundamentales para comprender el comportamiento de materiales complejos en diversas aplicaciones, incluyendo sistemas biológicos, liberación de fármacos y materiales avanzados. En entornos biológicos, estas propiedades juegan un papel crucial en la mecánica celular, el transporte intracelular y los procesos de difusión, influyendo en cómo las partículas se desplazan en medios confinados o heterogéneos. En la liberación de fármacos, la viscosidad local y la viscoelasticidad del medio pueden afectar la agregación de nanopartículas, su difusión y su interacción con fluidos biológicos, lo cual es esencial para optimizar terapias dirigidas. Más allá de la biomedicina, estas propiedades también son relevantes en nanotecnología, optoelectrónica, cristales fotónicos y dispositivos de cristales líquidos.

Esta tesis se centra en el análisis de las propiedades dinámicas y viscoelásticas de sistemas de cristales líquidos coloidales compuestos por partículas esferocilíndricas, con un enfoque particular en el efecto de interacciones dipolares sobre estas propiedades. El trabajo se enfoca principalmente en la simulación de dos fases de cristal líquido: nemática y esméctica, utilizando el método de Dinámica Monte Carlo (DMC).

Este método, basado en el algoritmo de Metrópolis, genera movimientos aleatorios de las partículas, cuyos desplazamientos están restringidos de acuerdo con el coeficiente de difusión en el límite de dilución infinita. Para ello, se emplean las ecuaciones de Einstein para el movimiento browniano, lo cual impide que las partículas presenten movimientos no físicos, como el intercambio de posiciones entre partículas o el movimiento colectivo de clústeres. Debido a esta formulación, el método DMC reproduce de manera efectiva la evolución temporal de sistemas con dinámica browniana, permitiendo estudiar su comportamiento sin necesidad de resolver explícitamente ecuaciones de movimiento. Así, el re-escalamiento adecuado de los pasos de Monte Carlo permite acceder a escalas temporales comparables con los tiempos de relajación característicos del sistema.

A partir de estas simulaciones, es posible analizar diversas propiedades estructurales y dinámicas del sistema, tales como los desplazamientos cuadráticos medios, los coeficientes de difusión y los tiempos de relajación del sistema. Sin embargo, en sistemas de cristales líquidos, la viscoelasticidad juega un papel crucial en sus respuestas mecánicas y tienen aplicaciones directas en el diseño de materiales. Por esta razón, además de analizar propiedades dinámicas, en este trabajo exploramos las propiedades reológicas del sistema mediante la técnica de microreología pasiva, que permite estimar los módulos viscoelásticos del sistema a partir del análisis del movimiento espontáneo de partículas trazadoras. A diferencia de la reología convencional, que mide la respuesta promedio de un material a nivel macroscópico, la microreología pasiva proporciona información local, lo cual es particularmente relevante en sistemas de cristales líquidos, donde la viscoelasticidad puede variar espacialmente debido a la anisotropía del sistema.

Los sistemas de cristal líquido estudiados inicialmente interactúan mediante el potencial de Kihara. Para analizar cómo las interacciones de largo alcance modifican las propiedades del sistema, se introdujeron interacciones dipolares empleando el método de campo de reacción. Esto permitió evaluar su impacto en las propiedades viscoelásticas y dinámicas, incluyendo el coeficiente viscoelástico, los desplazamientos cuadráticos medios y los coeficientes de auto-difusión. Dado que las interacciones dipolares modifican la organización estructural de los cristales líquidos, su estudio proporciona información relevante para comprender cómo estas interacciones afectan la respuesta mecánica del sistema y sus posibles aplicaciones en sistemas anisotrópicos.

Si bien este trabajo se centra en el estudio de cristales líquidos coloidales, entender las interacciones locales puede ayudar a hacer inferencias sobre las propiedades macroscópicas, ya que las interacciones a escala microscópica pueden influir en el comportamiento global del sistema y en propiedades clave para el diseño de dispositivos tecnológicos.

Esta relación entre estructura y propiedades macroscópicas es clave en diversas aplicaciones tecnológicas, incluyendo materiales para displays y dispositivos ópticos. Durante mi estancia en AlphaMicron, una empresa especializada en cristales líquidos moleculares para eyewear y pantallas, adquirí experiencia en la fabricación y caracterización de celdas de cristales líquidos. Los sistemas que estudié durante mi estancia en AlphaMicron, si bien de naturaleza molecular, comparten principios clave con los cristales líquidos coloidales simulados en esta tesis, como el autoensamblaje, la anisotropía en el transporte y la respuesta viscoelástica. Esta experiencia me permitió conectar la teoría con desafíos prácticos en la fabricación y diseño de dispositivos, reforzando la importancia de comprender las propiedades locales y dinámicas en materiales anisotrópicos.

En este trabajo, se contribuye al entendimiento de las propiedades dinámicas y viscoelásticas en cristales líquidos coloidales, explorando cómo la estructura y las interacciones afectan la difusión, los tiempos de relajación y la viscoelasticidad local del sistema. En particular, se analiza la influencia de las interacciones dipolares en estos materiales, proporcionando una base para futuras investigaciones sobre el impacto de interacciones de largo alcance en sistemas anisotrópicos. Estos resultados pueden ser relevantes en el estudio de materiales funcionales para aplicaciones como sensores, dispositivos ópticos y tecnologías fotónicas, así como en el diseño de sistemas de liberación de fármacos más eficientes, donde en ambos casos la respuesta dinámica y viscoelástica desempeña un papel fundamental en el rendimiento del sistema.

Summary

The dynamic and viscoelastic properties of colloidal systems are essential for understanding the behavior of complex materials in various applications, including biological systems, drug delivery, and advanced materials. In biological environments, these properties play a crucial role in cellular mechanics, intracellular transport, and diffusion processes, influencing how particles move within confined or heterogeneous media. In drug delivery, local viscosity and viscoelasticity can impact nanoparticle aggregation, diffusion, and interactions with biological fluids, which is essential for optimizing targeted therapies. Beyond biomedicine, these properties are also relevant in nanotechnology, optoelectronics, photonic crystals, and liquid crystal devices.

This thesis focuses on the analysis of the dynamic and viscoelastic properties of colloidal liquid crystal systems composed of spherocylindrical particles, with particular emphasis on the effect of dipolar interactions on these properties. The study primarily explores the simulation of two liquid crystal phases, nematic and smectic, using the Dynamic Monte Carlo (DMC) method.

This method, based on the Metropolis algorithm, generates random particle displacements, which are constrained according to the diffusion coefficient in the infinite dilution limit. To achieve this, Einstein's equations for Brownian motion are employed, preventing unphysical movements such as particle exchanges or collective cluster translations. Due to this formulation, the DMC method effectively reproduces the temporal evolution of systems governed by Brownian dynamics, allowing their behavior to be studied without explicitly solving equations of motion. By appropriately rescaling Monte Carlo steps, it is possible to access time scales comparable to the system's characteristic relaxation times.

These simulations allow for the analysis of various structural and dynamic properties of the system, such as the mean squared displacement (MSD), diffusion coefficients, and relaxation times. However, in liquid crystal systems, viscoelasticity plays a crucial role in their mechanical responses and has direct applications in material design. For this reason, in addition to analyzing dynamic properties, this work also explores the system's rheological properties using the passive microrheology (MR) technique. This approach estimates the system's viscoelastic moduli by analyzing the spontaneous motion of tracer particles. Unlike conventional rheology, which measures a material's macroscopic response, passive microrheology provides local information, which is particularly relevant in liquid crystal systems where viscoelasticity can vary spatially due to anisotropy.

The studied liquid crystal systems initially interacted via the Kihara potential. To investigate how long-range interactions modify the system's properties, dipolar interactions were introduced using the reaction field method. This allowed for an assessment of their impact on viscoelastic and dynamic properties, including the viscoelastic coefficient, mean squared displacement, and self-diffusion coefficients. Since dipolar interactions influence the structural organization of liquid crystals, their study provides valuable insight into how they

affect the mechanical response of the system and their potential applications in anisotropic materials.

Although this work focuses on colloidal liquid crystals, understanding local interactions can help infer macroscopic properties, as microscopic interactions influence the global behavior of the system and key properties relevant to technological applications.

This relationship between structure and macroscopic properties is key to various technological applications, including materials for displays and optical devices. During my internship at AlphaMicron, a company specializing in molecular liquid crystals for eyewear and display technologies, I gained experience in the fabrication and characterization of liquid crystal cells. The systems I worked with at AlphaMicron, although molecular in nature, share fundamental principles with the colloidal liquid crystals simulated in this thesis, such as self-assembly, transport anisotropy, and viscoelastic response. This experience allowed me to bridge theoretical knowledge with practical challenges in the fabrication and design of devices, reinforcing the importance of understanding local and dynamic properties in anisotropic materials.

This work contributes to the understanding of dynamic and viscoelastic properties in colloidal liquid crystals, exploring how structure and interactions affect diffusion, relaxation times, and local viscoelasticity. In particular, it analyzes the influence of dipolar interactions in these materials, providing a foundation for future research on the impact of long-range interactions in anisotropic systems. These findings may be relevant for studying functional materials in applications such as sensors, optical devices, and photonic technologies, as well as in the design of more efficient drug delivery systems, where dynamic and viscoelastic responses play a fundamental role in system performance.

Acknowledgments

First and foremost, I would like to express my sincere gratitude to my advisors, Dr. Alejandro Gil-Villegas and Dr. Alessandro Patti, for their continuous guidance, insightful discussions, and invaluable support throughout this research. Their expertise and encouragement have been fundamental in shaping this work.

I am deeply grateful to CONAHCYT for providing financial support throughout my PhD studies. Additionally, I extend my appreciation to the University of Guanajuato for funding my research stay at AlphaMicron, USA, where I had the opportunity to expand my knowledge and gain valuable experience. I also thank AlphaMicron for welcoming me into their team and providing the resources necessary for my internship, especially Pedro Coutino for his guidance and support during my stay.

I would also like to express my gratitude to Dr. Robin L. B. Selinger for hosting me during my research stay at Kent State University. Although this work was not directly part of my thesis, the experience significantly contributed to my understanding of molecular simulations. Presenting my research to her group and engaging in discussions there helped broaden my perspective and strengthen my skills in computational modeling.

I am also thankful to my colleagues and friends who have accompanied me on this journey, sharing knowledge, discussions, and moments of both struggle and success.

Finally, and on a personal level, I am profoundly grateful to my family for their unconditional love and support, which has been my source of strength and motivation. Special thanks to my partner, whose encouragement and patience have been invaluable throughout this process.

This thesis would not have been possible without the support of all those mentioned above, and I am truly grateful for their contributions.

INDEX

1	Introduction	11
2	Colloidal Systems and Liquid Crystals Definition and Properties	13
2.1	Colloidal Systems	13
2.2	Liquid Crystals	14
2.3	Nematic Liquid Crystals	16
2.3.1	Chiral Nematics	20
2.4	Smectic Liquid Crystals	20
2.5	LC properties	23
2.5.1	Dielectric Properties	23
2.5.2	Viscoelastic Properties	24
2.6	Brownian Motion	25
2.7	Einstein's theory of Brownian Motion	26
2.8	Self-diffusion	29
2.9	Statistical Mechanics resources	30
2.10	Canonical ensemble	34
3	Computational Simulation Method	37
3.1	Monte Carlo method	37
3.2	Metropolis Algorithm	38
3.3	Radial Distribution Function	41
3.3.1	Additional details Periodic boundary conditions	44
3.4	Model and MC simulation details	45
3.5	Order parameter	48
3.6	Dynamic Monte Carlo method	49
3.7	Van Hove and intermediate scattering functions	53
4	Microrheology in Liquid Crystals	54
4.1	Introduction to Microrheology	54
4.1.1	Active vs Passive Microrheology	56

4.2	Generalized Stoke-Einstein Relation (GSE).....	56
4.3	Mason Approach	58
4.4	Implementation of Microrheology in DMC Simulations	60
5	Long- range interactions	62
5.1	Dipolar potential.....	63
5.2	Onsager reaction field.....	65
6	Results for the non-dipolar case	72
6.1	Structural properties	72
6.2	Dynamic properties.....	75
6.3	Self-diffusion.....	78
6.4	The Van Hove function	79
6.5	Intermediate scattering function	82
6.6	Effect of modifying the Kihara potential on phase behavior.....	84
7	Results for the dipolar case	86
7.1	Effect of Dipolar Interactions at High Temperatures	90
7.2	Transition from Nematic to Smectic Phase	93
7.3	Nm and Sm at temperature 1.46	103
8	Applications of liquid crystals and practical experience during internship	116
8.1	Applications of liquid crystals in the industry.....	117
8.2	Applications of liquid crystals in eyewear	117
8.3	Internship experience: Liquid crystals eyewear	118
8.4	Internship experience: Liquid crystals photoalignment.....	126
9	Conclusions and Perspectives	131
	Appendix I	134
	Appendix II.....	136
	Appendix III.....	137
	Appendix VI	139
9.1	Bibliography	144

1 Introduction

Colloidal systems play a crucial role in various technological applications, spanning nanotechnology, optoelectronics, and biological systems, including proteins, blood cells, and microorganisms [1.1]. Understanding, predicting, and controlling the microstructural and dynamic properties of these systems is fundamental to advancing both theoretical knowledge and practical applications where processes such as self-assembly and nucleation play a crucial role [1.2], for instance, in systems like liquid crystals [1.3][1.4].

One of the key aspects of colloidal liquid crystals research is the study of their dynamic behavior, which has led to critical insights across multiple fields in physics and technology. For example, self-assembling systems of rod-like particles exhibit novel optical characteristics due to their anisotropic shapes, making them relevant for fundamental research in liquid crystal phases. Additionally, in biological systems, colloidal interactions govern processes in active matter, such as bacterial motion and cellular organization [1.5].

While experimental techniques provide valuable information on colloidal dynamics, computational simulations are essential for studying these systems at different time and length scales. A widely used simulation approach is Brownian Dynamics (BD), which models colloidal motion by solving the overdamped Langevin equation. However, BD simulations require careful selection of the time step to balance computational efficiency and accuracy in long-time dynamics [1.6][1.7].

An alternative approach is Dynamic Monte Carlo (DMC), a stochastic method based on the Metropolis algorithm, which updates the system state through probabilistic moves rather than integrating differential equations. Each move is accepted or rejected based on an energy criterion dictated by the Boltzmann distribution, allowing the system to evolve while maintaining detailed balance. DMC has been widely applied in studying colloidal suspensions, glassy materials, and self-assembling structures, including silica dynamics [1.8], demonstrating its versatility in modeling equilibrium and non-equilibrium phenomena. In this work, DMC is employed to study the dynamics of spherocylindrical rods in liquid crystal phases, capturing their diffusive and structural properties efficiently.

Beyond their diffusive behavior, colloidal systems also exhibit viscoelastic properties, which describe their ability to store and dissipate mechanical energy. Understanding these properties is crucial in multiple fields, including soft matter physics, biomimetic materials, microfluidics, and drug delivery [1.9-1.13] where controlling local viscosity and elasticity provides insight into self-organization and transport phenomena. In colloidal liquid crystals, the viscoelastic response is particularly relevant, as these systems exhibit anisotropic mechanical properties that influence their collective behavior.

To investigate these local viscoelastic properties, microrheology has emerged as a powerful tool, allowing the measurement of viscosity and elasticity by analyzing the thermal motion of an

embedded probe particle. In this work, we implement passive microrheology within DMC simulations, tracking the mean squared displacement (MSD) of a spherical probe particle to extract the complex shear modulus of the surrounding liquid crystal medium. This study contributes to the fundamental understanding of viscoelasticity in anisotropic colloidal suspensions, providing a theoretical framework for future experimental and numerical investigations in the field.

In addition to short-range interactions, dipolar interactions play a fundamental role in determining the properties of liquid crystalline colloidal phases. These long-range interactions influence the rheological behavior of the system, modifying its local viscoelastic response. Unlike molecular liquid crystals used in commercial applications, colloidal liquid crystals represent a class of systems where mesoscopic interactions drive self-assembly and structural organization.

In this work, dipolar interactions are introduced using the reaction field method, enabling a detailed study of how they affect local viscoelastic properties. By comparing systems with and without dipolar interactions, we analyze modifications to viscoelastic coefficients, mean squared displacements, and self-diffusion properties. The results obtained in this study provide a theoretical basis for understanding how long-range interactions influence viscoelastic behavior in colloidal liquid crystals, contributing to the broader investigation of soft condensed matter systems.

The thesis is divided into ten chapters, which are described as follows: Chapter 2 describes the fundamental concepts of colloids and liquid crystals. Chapter 3 introduces Monte Carlo (MC) and Dynamic Monte Carlo (DMC) methods. Chapter 4 explains the microrheology method implemented in the simulations. The details for the reaction field method, essential for incorporating dipolar interactions, are described in Chapter 5. Chapter 6 describes the process for visualizing the particles derived from the results of the simulations. Chapters 7 and 8 discuss the structural, dynamic and viscoelastic results obtained for dipolar and non-dipolar systems. Chapter 9 presents practical applications based on an internship project in the liquid crystal industry. Chapter 10 summarizes the conclusions and future perspectives.

2 Colloidal Systems and Liquid Crystals Definition and Properties

Soft matter physics comprises a diverse range of materials that exhibit properties intermediate between solid and liquid states. Among these, liquid crystals stand out for their ability to combine fluidity of liquids and ordering of solids. These unique properties make them ideal for numerous applications, from display technologies to advanced functional materials.

In colloidal liquid crystal systems, the building blocks are colloidal particles suspended in a medium that self-organize into ordered phases under the influence of thermal fluctuations and external forces. The motion and interactions of these particles are governed by Brownian dynamics.

Colloidal liquid crystals are particularly interesting because they help us understand how small-scale interactions can lead to large-scale structures and properties, for example phase transitions and ordering phenomena.

This chapter introduces the basic concepts of liquid crystals and their connection to colloidal systems, which is important for understanding the behavior of the materials studied in this thesis.

2.1 Colloidal Systems

Colloidal systems consist of particles with sizes typically ranging from 1 nm to 10 μm , placing them at the interface between molecular and macroscopic scales [2.1]. In this regime, their behavior is strongly influenced by a combination of thermal fluctuations, Brownian motion, and interparticle interactions. Unlike molecular systems, where interactions are often dominated by short-range forces, colloidal particles experience effective interactions that can extend over longer distances due to excluded volume effects, electrostatic forces, or external fields.

A key characteristic of colloidal particles is their Brownian motion, which arises from random thermal displacements due to collisions with surrounding molecules [2.2]. This diffusive behavior, combined with their relatively slow dynamics compared to atomic or molecular systems, makes colloidal suspensions ideal for studying phase transitions, self-assembly, and emergent ordering phenomena.

In particular, colloidal liquid crystals represent an important class of anisotropic colloidal systems. Here, the phase behavior is dictated by the shape and interactions of the particles themselves, rather than by the presence of an explicit solvent. The equilibrium phases, such as isotropic, nematic, and smectic states, emerge from the collective organization of rod-like colloidal particles, which interact primarily through excluded volume effects and soft repulsive interactions [2.3]. The stability and transitions between these phases are highly sensitive to the specific nature of the

interparticle potential, making them an ideal model system for investigating how microscopic interactions influence macroscopic ordering.

2.2 *Liquid Crystals*

Liquid crystals (LCs) are materials that exhibit properties of both liquids and solids. Like liquids, they can flow and adapt to the shape of their container, but they also display ordering characteristics typical of solids. However, unlike conventional solids, their molecular arrangement is not fully rigid or periodic. This intermediate nature defines liquid crystals as mesophases, existing between the crystalline solid and isotropic liquid states.

To better understand liquid crystals, it is useful to first consider the fundamental differences between solids and liquids. Crystalline solids maintain a fixed shape with molecules arranged in a regular, periodic lattice. This structure grants them both positional order (particles are spatially fixed) and orientational order (molecules align in specific directions), leading to anisotropic physical properties, such as variations in optical, mechanical, or thermal behavior depending on the measurement direction.

In contrast, liquids exhibit neither positional nor orientational order. Molecules move freely, rotate, and flow, resulting in an isotropic state where physical properties remain the same in all directions. Although there are no long-range correlations in a typical liquid, short-range correlations exist due to intermolecular forces, such as van der Waals interactions or hydrogen bonding.

Liquid crystals are a unique intermediate state between liquids and solids. They exhibit orientational order, where molecules preferentially align along a common direction, defined by the nematic director, but may lack full positional order, depending on the phase. Some liquid crystal phases, such as smectics, maintain partial positional order, whereas nematic phases only retain orientational alignment. [2.4][2.5].

A defining characteristic of liquid crystals is their anisotropic behavior. Properties such as refractive index, conductivity, and elasticity [2.6] depend on molecular orientation and external forces. This anisotropy is a direct consequence of molecular alignment, distinguishing liquid crystals from isotropic liquids.

Liquid crystals can form by heating a crystalline solid or cooling an isotropic liquid. These thermotropic transitions occur within specific temperature ranges and are reversible. Upon heating, a crystalline solid can transition into an isotropic liquid, but depending on molecular properties and temperature, it may pass through liquid crystalline phases such as nematic or smectic before becoming fully disordered. Similarly, cooling an isotropic liquid can lead to the formation of liquid crystal phases under appropriate conditions.

The molecular structure plays a key role in determining liquid crystal formation. Rod-like (calamitic) and disk-like (discotic) molecules are particularly well-suited for forming liquid crystal phases [2.5]. Their anisotropic shape allows them to align in preferred directions, giving rise to the

orientational order that distinguishes liquid crystals from ordinary fluids. However, unlike solid crystals, liquid crystals do not exhibit complete positional order but instead display local ordering with long-range correlations.

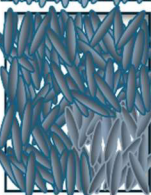
	Phase	Ordering description
	Crystal	3D positional order, Orientational order,
	Smectic LC	1D positional order, Orientational order,
	Nematic	No positional order, Orientational order,
	Isotropic liquid	No positional order, No orientational order

Figure 2.1 Description of molecular organization and ordering of different phases of matter.

LCs have several applications. Some of them are in the field of electro-optics [2.7]. LCs are used in displays, particularly in the technology behind them. Various types of displays can be created such as dynamic scattering, twisted nematic, supertwisted nematic, among others. Liquid crystal displays (LCDs) are commonly used in electronic devices such as televisions and smartphones. The alignment of the liquid crystal molecules can be manipulated by applying an electric field, which changes the optical properties of the material and produces an image [2.7]. LCs find applications in sensors. LCs are used to detect changes in temperature, pressure, or other physical properties. The alignment of the molecules changes with the input signal, which can be detected and used to measure the input. LCs are also used in materials science, since they have been used to produce materials with unique properties, such as high strength and toughness [2.7].

The study of liquid crystals has also led to new insights into fundamental physics and chemistry. The structure and behavior of liquid crystals have been used to explore phenomena such as chirality, phase transitions, and defects. The properties of liquid crystals can also be modified by

the addition of other molecules, leading to the development of new materials with tailored properties.

The significance of simulating and characterizing LCs has grown due to their extensive applications in fields such as electronics, materials science, and sensing. The unique properties of liquid crystals not only drive advancements in various technologies but also enhance our understanding of fundamental physics and chemistry.

2.3 *Nematic Liquid Crystals*

The defining characteristic of nematic liquid crystals is the alignment of their molecules along a preferred direction, known as the nematic director, or simply as the director, typically denoted as \mathbf{n} . In the nematic phase, molecules tend to align parallel to the director, but unlike solid crystals, they are not fixed in position and can move freely relative to one another [2.5]. As a result, nematic LCs exhibit long-range orientational order while retaining liquid-like dynamics [2.8].

The director is a unit vector that represents the average molecular orientation within the material and serves as the principal axis defining the system's symmetry. This concept is illustrated in Figure 2.3.2, where the director \mathbf{n} is shown as the preferred molecular orientation in a nematic liquid crystal phase. The angle θ represents the deviation of individual molecular axes from the director. Although the local orientation of the director can vary spatially, nematic phases can be easily aligned by weak external fields, such as electric or magnetic fields, or through interactions with surfaces. This alignment results in a monodomain configuration, where the entire sample exhibits a uniform molecular orientation.

An aligned nematic phase possesses uniaxial symmetry, meaning its physical properties remain unchanged under rotations around the director, assuming the system is isotropic in the perpendicular directions. This anisotropy is a key feature of nematic liquid crystals and is responsible for their unique optical and mechanical behaviors, making them highly useful in applications such as liquid crystal displays (LCDs).

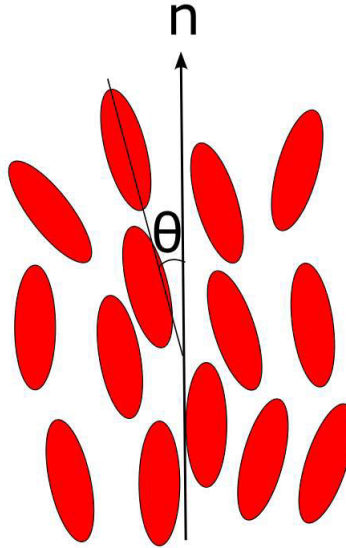


Figure. 2.3.1 Representation of the nematic liquid crystal phase and the director vector \mathbf{n} . The molecules tend to align along the director, represented by the unit vector \mathbf{n} . The angle θ indicates the deviation of individual molecular axes from the director.

The director is typically considered to be equivalent to its inverse, \mathbf{n} and $-\mathbf{n}$, reflecting the apolar nature of the molecules.

The alignment of the molecules forming the nematic phase, parallel to the director \mathbf{n} can be approximately quantified using the order parameter S_2 . First proposed by Tsvetkov in 1939, this parameter assumes that each mesogen behaves as a uniaxial particle, with its orientation described by a unit vector \mathbf{u}

$$\langle S_2 \rangle = \frac{3}{2} \langle (\mathbf{u} \cdot \mathbf{n})^2 \rangle - \frac{1}{2}$$

Where $\mathbf{u} \cdot \mathbf{n} = \cos\beta$, with β the angle between the molecular axis and the director, $S_2(\cos\beta)$ is the second Legendre polynomial and the angular brackets indicate an average over all the molecules comprising the system.

For a system where all molecules are perfectly aligned with respect to the director, $S_2 = 1$. Conversely, in a completely isotropic system, there is no preferential direction for the molecular orientations, meaning the molecules are oriented randomly in all directions. This results in the components of the molecular orientation along the X , Y and Z axes being equal on average. Mathematically, this can be expressed as

$$\langle \cos^2\beta \rangle = \langle u_z^2 \rangle = \langle u_x^2 \rangle = \langle u_y^2 \rangle = \frac{1}{3}$$

Where

$$u_z^2 + u_x^2 + u_y^2 = 1$$

Therefore, in a completely disordered system, the order parameter $S_2 = 0$, indicating no directional preference.

Nematic liquid crystals exhibit anisotropy due to their orientational order. This anisotropy affects different physical properties, including optical, dielectric, and rheological behavior, which are direction-dependent relative to the director. For example, nematics exhibit different macroscopic viscosities depending on the relative orientation of the flow velocity \mathbf{v} of the director as described in [2.9][2.10].

The liquid crystal molecules that form the nematic phase tend to have elongated, rod-like shapes that promote the alignment. This alignment is a result of molecular interactions such as van der Waals forces, which favor parallel orientations.

To further illustrate the nematic phase, Figure 2.3.2 presents a representative snapshot obtained from our Monte Carlo simulations. In this configuration, elongated particles exhibit long-range orientational order along a preferred direction, consistent with nematic behavior. However, unlike smectic or crystalline phases, positional order is absent, allowing for free translational motion of the particles while maintaining their alignment.

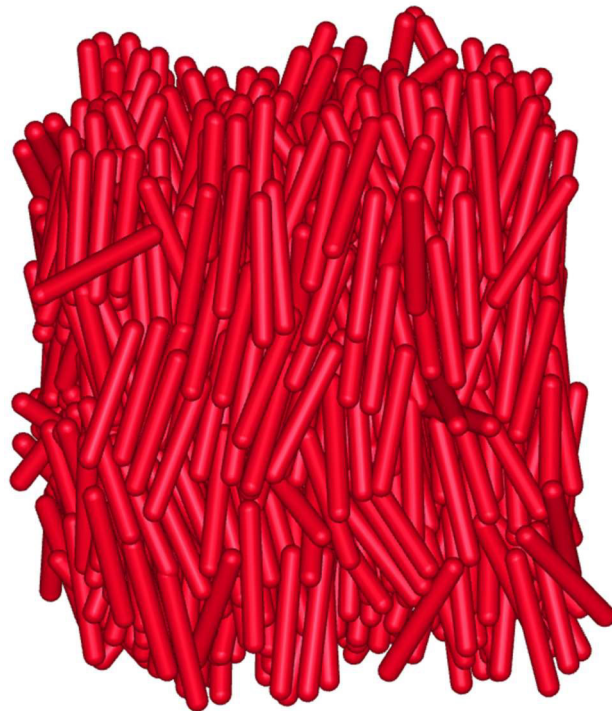


Figure 2.3.2 Snapshot of a nematic liquid crystal phase obtained from Monte Carlo simulations.

The elongated particles align along a common direction, forming a uniaxial nematic phase characterized by long-range orientational order without positional order.

Conventional nematic liquid crystals represented by an elongated or rod-like shape constitute a uniaxial medium, with nonpolar symmetry. A well-known example of a thermotropic nematic liquid crystal molecule is the 4-n-pentyl-4-cyano-biphenyl (5CB). The following figure presents the chemical structure of 5CB (a), (b) its coarse-grained representation and (c) illustrates its molecular shape.

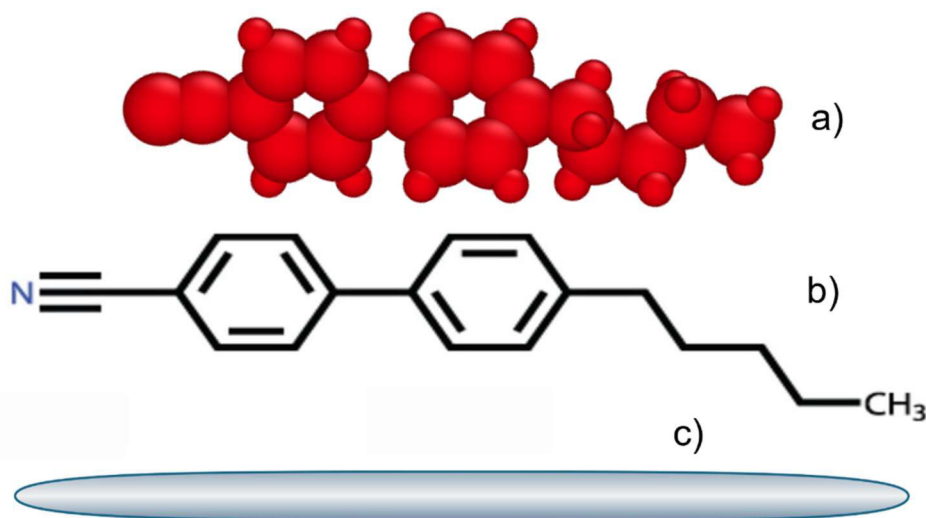


Figure 2.3.3 a) Molecular dynamics visualization (Ovito) with explicit atomic representation, showing hydrogen and carbon atoms, and at the top the cyanobiphenyl group (CN). b) Chemical structure of the 5CB molecule, showing its aromatic rings and chemical bonds. c) Simplified rod-like representation of the molecule, often used in coarse-grained models.

The molecule 5CB is a widely studied nematic liquid crystal due to its relatively simple structure and well-characterized physical properties. Its rod-like geometry and chemical composition make it a prototypical example for understanding the behavior of nematic phases. The representations in Figure 2.3.3 highlight its versatility, from detailed atomic models used in molecular dynamics simulations to simplified rod-like approximations employed in theoretical studies. These models serve as the foundation for exploring the alignment, order, and anisotropic properties characteristic of nematic liquid crystals

The ability of nematic molecules to move and reorient in response to external stimuli makes them highly dynamic systems. Despite the presence of orientational order, nematics exhibit behavior akin to fluids and share similar viscosities and densities with isotropic liquids

In addition to the flow behavior, nematics exhibit unique optical properties due to their anisotropic nature. For example, they can show birefringence, which is the difference in the refractive index

depending on the polarization direction of light relative to the director. As mentioned previously, these optical properties are essential for the development of display technologies.

2.3.1 Chiral Nematics

Chiral nematics, also known as cholesteric liquid crystals, are a special type of nematic phase where the director \mathbf{n} adopts a helical configuration. This twisted structure can occur naturally in systems composed of chiral molecules (chiral mesogens) or can be induced by adding a chiral dopant to a nematic liquid crystal. Cholesteric liquid crystals derive their name from cholesterol, the first liquid crystals discovered, in 1888 by Friedrich Reinitzer [2.11].

In cholesterics, the local alignment of molecules resembles that of nematics, but the director gradually rotates around a helical axis, forming a periodic structure. The distance over which the director completes a full 360° rotation is called the pitch p , which typically spans a few hundred nanometers. Although this gives cholesterics their unique optical properties, such as selective reflection of light, on a molecular scale they appear quite similar to nematics.

The pitch and handedness of the helix are determined by the chirality of the constituent molecules. For example, right-handed molecules produce a right-handed helical structure, while left-handed molecules create a left-handed one. This intrinsic twist can be visualized by considering threaded rods that cannot align perfectly parallel but instead adopt a twisted orientation when in contact, ultimately forming a helical arrangement.

Cholesteric liquid crystals are notable for their striking visual effects, including their vibrant, iridescent colors, which arise from the interaction of light with the helical structure. Due to these characteristics, cholesterics are useful for applications such as liquid crystal displays, temperature sensors, and optical filters.

2.4 Smectic Liquid Crystals

Smectic liquid crystal (LC) phases are characterized by a combination of orientational and positional order. In these phases, particles self-organize into a layered structure [2.5], with each layer having an average thickness L approximately equal to the particle length. This representation is shown in Figure 2.4.1. Compared to nematic phases, smectics exhibit a higher degree of order and, despite retaining fluidity, they are more viscous and share greater similarities with crystalline phases than nematics and cholesterics.

The layered structure in smectic phases represents a form of positional order that is less rigid than the three-dimensional periodicity found in solid crystals. A wide variety of smectic phases exist [2.12], each with distinct molecular arrangements within the layers, leading to unique structural properties. In general, a smectic phase is denoted as Sm , while specific types, such as Sm_A , Sm_B , Sm_C , etc., are identified with additional subscripts to distinguish between different subphases.

Among smectic phases, the simplest and most studied is the smectic A (Sm_A) phase. In Sm_A , particles are arranged into layers and, on average, remain oriented perpendicular to these layers (Figure 2.4.1). Within each layer, the molecules lack long-range positional order, behaving like a two-dimensional liquid. This simplified description captures the essential nature of the Sm_A phase, though molecular interactions and fluctuations in orientation may introduce additional complexities. Moreover, smectic layers are often flexible, and the phase exhibits anisotropic properties that are influenced by external fields or surface interactions.

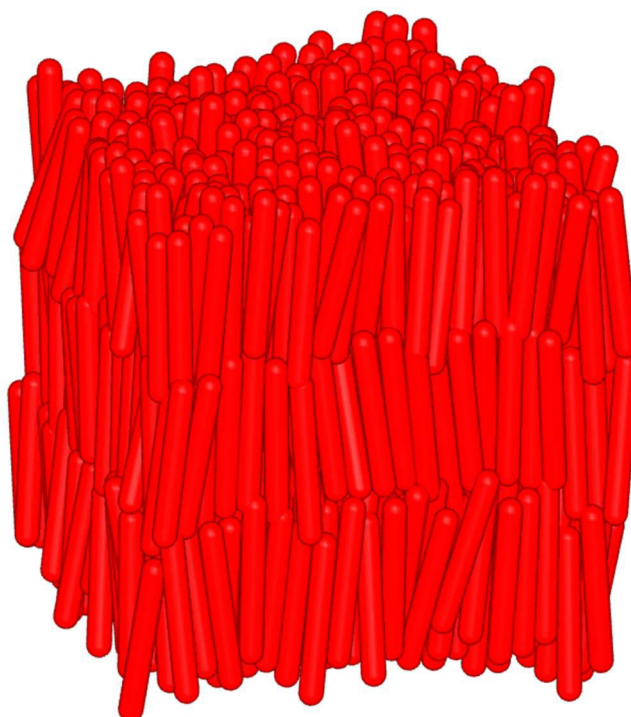


Figure 2.4.1. Snapshot of a smectic liquid crystal phase obtained from Monte Carlo simulations. The elongated particles self-organize into distinct layers while maintaining long-range orientational order. Within each layer, the molecules behave as a two-dimensional liquid, exhibiting no long-range positional order.

The smectic phase depicted in Figure 2.4.1 illustrates the characteristic layering of molecules, where long-range orientational order is preserved while translational order remains confined within individual layers.

The extent of translational order, characterized by a periodicity d , corresponds to the smectic layer spacing, which is approximately equal to the length L of a mesogen. This ordering is quantified by the smectic order parameter [2.14] given by

$$\Psi = \left\langle \frac{3\cos^2\theta - 1}{2} \cos\left(\frac{2\pi}{d_p} z_i\right) \right\rangle \quad (2.4.1)$$

In equation 2.4.1 z_i is the position of the center of mass of the particles and it includes the orientational order term S_2 multiplied by the positional order term, which corresponds to the first term in the Fourier expansion of the positional order distribution function.

While the Sm_A maintains molecules on average perpendicular to the layers, resulting in a phase that is optically uniaxial, other smectic phases exhibit molecular tilt relative to the layer normal. One such example is the Sm_C , where molecules adopt a characteristic tilt angle θ with the layer normal, as illustrated in Figure 2.4.2. Depending on whether the molecules in neighboring layers exhibit a helical arrangement or not, the Sm_C phase can be classified as chiral or non-chiral. [2.13]

This tilt angle can vary with temperature and molecular interactions, influencing the material's optical and structural properties. The degree of tilt plays a crucial role in distinguishing between smectic subphases and is a defining characteristic of Sm_C systems. In some cases, this ordering can lead to additional symmetry breaking, giving rise to chiral or non-chiral smectic phases, depending on the relative orientation of neighboring layers

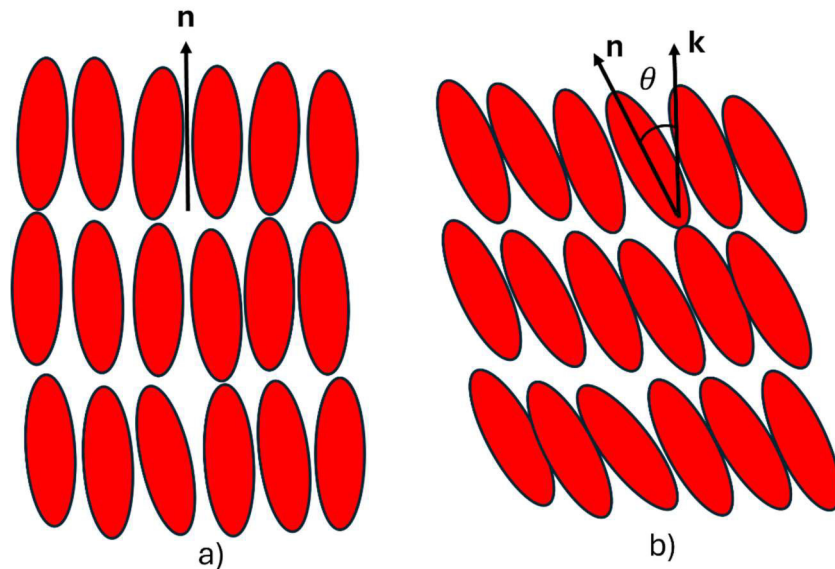


Figure 2.4.2 Representation of smectic liquid crystal phases. (a) Sm_A phase, where molecules remain perpendicular to the layers. (b) Sm_C phase, where molecules exhibit a characteristic tilt angle θ relative to the normal layer.

Beyond the Smectic A and Smectic C phases, additional smectic subphases exist, characterized by increased molecular organization within the layers. One such example is Sm_B . This phase has a layered structure similar to Sm_A , where the molecules are, on average, perpendicular to the layer

normal. However, Sm_B exhibits higher viscosity than Sm_A and feature hexagonal arrangements of molecular centers within each layer, resulting in a biaxial symmetry. This type of arrangement is referred to as bond order, making the Sm_B phase a bond-orientationally ordered variant of Sm_A . These hexagonal clusters may be orientationally ordered or disordered relative to one another, depending on the specific Sm_B phase.

2.5 LC properties

Liquid crystals exhibit unique physical properties that arise from their intermediate state between solid and liquid phases. Their molecular structure leads to a combination of fluidity and anisotropic ordering, resulting in macroscopic behaviors that differ significantly from those of isotropic liquids or crystalline solids.

Among the most relevant properties that characterize liquid crystals are their dielectric response, viscosity, and elasticity, which are intrinsically linked to the orientational and positional order of their constituent molecules. These properties play a fundamental role in determining phase behavior, structural transitions, and the response of liquid crystals to external fields.

Understanding these physical properties is essential for characterizing the stability and dynamics of liquid crystalline phases. In particular, dielectric properties influence molecular interactions and polarization effects, while viscosity and elasticity are key to describing the flow and mechanical response of these materials. The following sections discuss these properties in more detail, with an emphasis on their role in liquid crystal phase behavior and how they are treated in theoretical and computational models.

2.5.1 Dielectric Properties

Pure organic liquids exhibit dielectric behavior (with conductivity $\sigma=0$) and are also diamagnetic, meaning their magnetic susceptibility can be expressed as $\mu = 4\pi\chi \approx 1$. The refractive index n , linked to the dielectric permittivity at optical frequencies, is given by $n^2 = \mu\epsilon \approx 1$. At these frequencies, the dielectric permittivity $\epsilon(\omega)$ is influenced by the average electronic and atomic polarizabilities of the molecules ($\langle\gamma^2\rangle$), and can be described by the Lorenz–Lorentz relation [2.15]:

$$\frac{n^2 - 1}{n^2 + 1} = \frac{4\pi}{3} \frac{\rho}{m} N_A \langle\gamma^E\rangle \quad (2.5.1)$$

Where ρ is the density of the substance, m is the molecular mass, N_A is the Avogadro number and $\langle\gamma^E\rangle$ is the average polarizability in the electric field E .

$$\frac{\varepsilon^2 - 1}{\varepsilon^2 + 1} = \frac{4\pi \rho}{3 m} N_A \left(\langle \gamma^E \rangle + \frac{\mu^2}{3k_B T} \right) \quad (2.5.2)$$

Where $\frac{\mu^2}{3k_B T}$ is the orientational component of the average static polarizability, which depends upon the size of the dipole moment μ .

The dielectric constant is a fundamental property of materials that describes their response to external electric fields, and its calculation can be approached from different perspectives. In classical theory, relationships such as the Clausius-Mosotti and Lorenz-Lorentz equations link macroscopic properties, like the dielectric constant, to molecular-scale parameters, such as electronic polarizability and dipole moment. These equations are widely used to understand and predict the behavior of dielectric materials at various frequencies

These relationships are particularly useful for describing macroscopic properties of homogeneous dielectric systems. In this work, the Clausius-Mosotti equation is used to compute the dielectric constant of the dielectric medium used in the reaction field method. The focus lies on describing local interactions at the molecular scale through Monte Carlo simulations. Specifically, the reaction field method is used, which determines the dielectric constant of the medium by simulating dipoles confined within a dielectric sphere without the need for an external electric field.

In this framework, the reaction field generated by the dipoles is sufficient to evaluate the dielectric properties of the system. This approach does not aim to derive macroscopic properties from global averages but rather explores how local interactions and the induced reaction field contribute to the effective dielectric constant of the medium.

This relationship will be revisited in detail in subsequent chapters to explore its implications for our systems.

2.5.2 Viscoelastic Properties

The viscoelastic properties of liquid crystals are fundamental in determining their dynamic response to external perturbations, such as electric or mechanical fields. These properties influence key behaviors, including molecular reorientation, flow dynamics, and deformation modes.

In nematic liquid crystals, deformations are primarily described by splay, twist, and bend distortions of the director \mathbf{n} , which represent local reorientations of the average molecular alignment. Unlike conventional fluids, these deformations do not involve translational displacements of molecules but instead result in variations in the elastic free energy. The elasticity of nematic liquid crystals is commonly described by the Frank free energy, which is governed by the elastic constants K_1 (splay), K_2 (twist), and K_3 (bend). Similarly, their viscous behavior follows an anisotropic Navier-Stokes formulation, incorporating viscosity coefficients that account for directional dependence in the viscous stress tensor [2.15]. Additionally, rotational viscosity coefficients (γ_1, γ_2) characterize the dissipation of energy associated with molecular reorientation, which can couple with flow effects, leading to phenomena such as backflow.

While these macroscopic models describe bulk rheological behavior, this thesis focuses on local viscoelastic properties, which are explored through passive microrheology in Monte Carlo simulations and will be described with more detail in the following section. Instead of characterizing large-scale flow or director deformations, a spherical tracer particle is introduced into the simulated liquid crystal system to probe the local viscoelastic environment. By analyzing the tracer's motion and its interactions with the surrounding medium, local viscosity and viscoelastic moduli are inferred.

This microrheological approach provides insight into spatial variations and heterogeneities in viscoelastic behavior that are not captured by macroscopic models. For instance, while classical elasticity theories assume uniform distortions of the director field, microrheology highlights how local molecular interactions, confinement effects, and anisotropic fluctuations shape the rheological response. These insights are particularly relevant in colloidal liquid crystals, where local effects strongly influence the overall dynamics and phase behavior.

2.6 *Brownian Motion*

Brownian motion refers to the erratic and random movement of microscopic particles suspended in a fluid. This phenomenon, first observed by Robert Brown in 1827 [2.16] while examining pollen grains in water, arises from the continuous collisions of fluid molecules with suspended particles. Since its discovery, Brownian motion has become a foundational concept in fields such as statistical mechanics, molecular biology, and materials science, contributing to our understanding of diffusion processes, particle dynamics, and the behavior of soft matter systems. The range of application of Brownian motion also includes modeling of stock prices, of thermal noise in electrical circuits and of random perturbations in a variety of other physical, biological, economic, and management systems [2.17].

The term Brownian motion describes the random movement of particles suspended in a medium. In Brownian motion a given particle is equally likely to move in any direction and further motion is totally unrelated to past motion. The motion is caused by the collisions of fluid or solvent molecules with the suspended particles, and it is affected by various physical factors, such as particle size, fluid viscosity, and temperature. The process in which the particles tend to move from a region of high concentration to a region of lower concentration is called diffusion.

The direction of the particle's collisions is constantly changing, and at different times the particle is hit more on one side than another, leading to the seemingly random nature of the motion. This explanation of Brownian motion served as convincing evidence that atoms and molecules exist and was further verified experimentally by Jean Perrin in 1908 [2.18].

The properties of Brownian motion have been extensively analyzed, including the mean square displacement, diffusion coefficient, and velocity autocorrelation function. The analysis of Brownian motion has led to the development of several models, including the Langevin equation, the Fokker-Planck equation, and the Einstein relation.

The theory of Brownian Motion was developed by Albert Einstein, and it is worth giving a general review to this theory to better explain some physical concepts used in liquid crystal simulations.

2.7 Einstein's theory of Brownian Motion

In 1905, Albert Einstein transformed this phenomenon into a cornerstone of statistical mechanics with his seminal paper, “*Über die von der molekularkinetischen Theorie der Wärme geforderte Bewegung von in ruhenden Flüssigkeiten suspendierten Teilchen*” [2.19]. In this work, Einstein provided the first probabilistic formulation of the motion of suspended particles, bridging thermodynamics and stochastic processes.

Einstein's analysis began with thermodynamic arguments and the concept of osmotic pressure, leading to the derivation of the particle diffusion constant by balancing diffusion and drift currents. This relationship, now known as the Einstein relation, connects the diffusion constant of particles to the viscosity of the surrounding fluid [2.18].

Einstein's insights into Brownian motion revolutionized the understanding of stochastic processes. He laid the foundation for the modern theory of diffusion, including the formulation of stochastic differential equations by Paul Langevin, which extended Newtonian mechanics to incorporate random, memory-less forces. This work enabled the development of a probabilistic framework for understanding particle dynamics

In his work about Brownian motion, Einstein proposed an infinitesimal time step, however, microscopically large enough, to permit a large number of collisions between the suspended particles. Many fluid molecules will collide with the Brownian particle within the time steps. Under these conditions, it is possible to define a function $f(x, t)$ for representing the probability density function of finding a particle within spatial and time intervals [2.17]. Therefore, $f(x, t)dxdt$ gives the probability of the number of Brownian particles, with spatial coordinates x and time coordinates t that fall within an interval between x and $x + dx$ and between a time t and $t + dt$.

In this derivation, we consider the diffusion equation in a single spatial dimension (x -direction) for simplicity. However, in the later analysis, the generalization to three dimensions will be used, as the simulations account for motion in all spatial directions.

The function $f(x, t)$ should satisfy the following differential equation [2.18]:

$$\frac{\partial f(x, t)}{\partial t} = D \frac{\partial^2 f(x, t)}{\partial x^2}. \quad (2.5.1)$$

Equation (2.5.1) is referred to as the diffusion equation. The constant D results equal to the half of the mean squared displacement (MSD) within a time dt , as demonstrated below.

To accomplish the above task and to find the analytical expression of the function $f(x, t)$ it is convenient to Fourier transform the spatial part of the differential equation 2.5.1 by means of the following Fourier relations,

$$F(u, t) = \int_{-\infty}^{\infty} f(x, t) e^{-i2\pi u x} dx, \quad (2.5.2)$$

$$f(x, t) = \int_{-\infty}^{\infty} F(u, t) e^{i2\pi u x} du. \quad (2.5.3)$$

Equations (2.5.2) and (2.5.3) represent the direct and inverse Fourier transforms of the function $f(x, t)$ in the spatial domain

Equation (2.5.3) is now substituted in equation (2.5.1). We obtain

$$\int_{-\infty}^{\infty} \frac{\partial F(u, t)}{\partial t} e^{i2\pi u x} du = D \int_{-\infty}^{\infty} (-4\pi^2 u^2) F(u, t) e^{i2\pi u x} du. \quad (2.5.4)$$

Equation (2.5.4) is satisfied if the integrands are equal. Therefore, we obtain the following equation

$$\frac{\partial F(u, t)}{\partial t} = (-4\pi^2 u^2 D) F(u, t). \quad (2.5.5)$$

Equation (2.5.5) represents equation (2.5.1) in the frequency-space time domain. Integrating equation (2.5.5) we find

$$\ln(F(u, t)) = (-4\pi^2 u^2 D)t + C. \quad (2.5.6)$$

Equation 2.5.6 leads to

$$F(u, t) = A_0 e^{(-4\pi^2 u^2 D)t}. \quad (2.5.7)$$

Now, considering the initial condition at $t = 0$, $F(u, 0) = A_0$. Therefore, we obtain,

$$F(u, t) = F(u, 0) e^{(-4\pi^2 u^2 D)t}. \quad (2.5.8)$$

Equation 2.5.8 represents the solution of the probability density function in Fourier space. Now, to find the solution in spatial coordinates and time, we will use the inverse Fourier transform given by equation (2.5.3), written for brevity as follows

$$f(x, t) = \mathcal{F}^{-1}\{F(u, 0) e^{(-4\pi^2 u^2 D)t}\}. \quad (2.5.9)$$

The product of functions inside of the inverse Fourier transform of equation (2.5.9), corresponds to a convolution in spatial domain. We obtain then,

$$f(x, t) = f(x, 0) \otimes \mathcal{F}^{-1}\{e^{(-4\pi^2 u^2 D)t}\}. \quad (2.5.10)$$

In equation (2.5.10) the symbol \otimes represents a one-dimensional convolution between the functions.

It still remains to calculate the Fourier transform of the second term and to accomplish that we use the properties of the Fourier transform of a gaussian function $\mathcal{F}\{e^{-\pi x^2}\} = e^{-\pi u^2}$ and $\mathcal{F}\{f(ax)\} = \frac{1}{a} \mathcal{F}\{f(\frac{u}{a})\}$ giving as a result

$$f(x, t) = f(x, 0) \otimes \frac{1}{\sqrt{4\pi Dt}} e^{\left(\frac{-\pi x^2}{4\pi Dt}\right)}. \quad (2.5.11)$$

Equation 2.5.11 represents the general expression of the probability density function for the Brownian motion and can be used for any physical initial conditions.

For our study, as we have an *a-priory* knowledge of our distribution, which is a Gaussian one, we consider the simple case of a Dirac delta function i.e. $f(x, 0) = \delta(x)$. Under this condition equation (2.5.11) leads to

$$f(x, t) = \frac{1}{\sqrt{4\pi Dt}} e^{\left(\frac{-\pi x^2}{4\pi Dt}\right)} \quad (2.5.12)$$

Equation 2.5.12 represents a probability density function with a spatial Gaussian profile and matches with our assumption at time $t = 0$

Using equation 2.5.12 it is deduced that the mean square displacement of the particle evolves with time calculating.

$$\langle x^2(t) \rangle = \frac{1}{\sqrt{4\pi Dt}} \int_{-\infty}^{\infty} x^2 e^{\left(\frac{-\pi x^2}{4\pi Dt}\right)} \quad (2.5.13)$$

Setting the appropriate variables changes as $A = \frac{\pi}{4\pi} = \frac{1}{4Dt}$, and using the known result of the integral $\int_{-\infty}^{\infty} x^2 e^{-Ax^2} dx = \frac{\sqrt{\pi}}{2A^{3/2}}$, we obtain the result for the mean square displacement of the particle evolving with time,

$$\langle x^2(t) \rangle = 2Dt \quad (2.5.14)$$

Where t must be large enough according to the previous assumptions.

Equation (2.5.14) leads to the definition of the diffusion coefficient D [2.17][2.18]. This equation will allow us to calculate the diffusion in liquid crystal systems which is crucial to understand their dynamical behavior.

2.8 Self-diffusion

The concept of self-diffusion refers to the process by which individual molecules or particles spread out spontaneously within a fluid due to their inherent kinetic energy [2.20]. This movement occurs without any external force or concentration gradient driving it.

Self-diffusion is closely related to Einstein's theory of Brownian motion. In Brownian motion, small, suspended particles exhibit random, jiggling movements in a fluid due to the constant collisions with fluid molecules. The random motion of these particles is a manifestation of self-diffusion at the microscopic level. The kinetic energy of the fluid molecules causes them to collide with and transfer their momentum to the suspended particles, leading to their dispersion throughout the fluid.

In essence, self-diffusion is the molecular-level process responsible for the Brownian motion observed on a macroscopic scale. Both phenomena are consequences of the random thermal motion of particles, but self-diffusion specifically refers to the movement of individual molecules or particles within a fluid.

In this thesis, the long-time self-diffusion coefficient is calculated using DMC simulations by analyzing the MSD of the particles over time. We track the position of the particles throughout the simulation and compute the MSD, which reflects how the positions deviate from their initial locations. By examining the linear region of the MSD versus time plot, where the displacement increases proportionally with time, we determine the self-diffusion coefficient. In the previous subsection, we derived the equation for MSD in terms of D for a single spatial direction, x . However, this result can be generalized to a three-dimensional system by considering the total displacement vector \mathbf{r} , where $r^2 = x^2 + y^2 + z^2$. In this case, the diffusion coefficient depends on the number of spatial dimensions d , such that

$$D = \frac{1}{2d} \frac{d\langle r^2(t) \rangle}{dt} \quad (2.6.1)$$

Where $d = 1, 2$ or 3 , depending on whether the diffusion is considered in one, two, or three dimensions, respectively.

This approach provides a measure of how quickly particles diffuse within the system, offering valuable insights into the dynamic behavior of the liquid crystal phases under investigation.

Self-diffusion exhibits distinct regimes characterized by the relationship between time and the mean square displacement of particles. In the short-time regime, the mean square displacement

increases quadratically with time, reflecting the restricted motion of particles due to spatial constraints and localized interactions. This behavior is typical in solids or dense liquids. As time progresses, the system enters the linear regime, where the mean square displacement becomes linearly proportional to time. In this regime, particles exhibit more free and unrestricted movement, characteristic of liquid states, leading to enhanced diffusion rates.

To quantify self-diffusion in liquid crystal phases, we compute the MSD along two distinct directions: parallel and perpendicular to the nematic director. This distinction is crucial because, in a nematic phase, particles are more likely to diffuse along the nematic direction due to the orientational order, while diffusion perpendicular to the director may be more restricted. In the smectic phase, additional positional order introduces further constraints, leading to a more anisotropic diffusion behavior.

The values of D_{\parallel} and D_{\perp} are extracted by fitting the linear regime of MSD curves over time. These results provide insight into how nematic and smectic order influence particle mobility.

The calculated self-diffusion coefficients will allow us to compare diffusion properties across nematic and smectic phases at different temperatures and subsequently evaluate the impact of dipolar interactions on their viscoelastic moduli. The concepts reviewed in this section will serve as a foundation for understanding the structural and rheological behavior of the system, as well as for interpreting the simulation data presented in the results section.

2.9 Statistical Mechanics resources

In this subsection we will introduce some aspects that will permit us to establish how the energy of a system is partitioned among the states of the ensemble that constitute it. This will allow us to introduce the concept of the partition function.

Let us consider a physical system composed by M states denoted as, $State_1, State_2 \dots State_M$. Each state has corresponding energies $E_1, E_2 \dots E_M$. In each one of the states there are $n_1, n_2 \dots n_M$ particles, respectively. The total number of particles N_T , corresponds to $N_T = n_1 + n_2 + \dots + n_M$, and that the total energy, E_T , corresponds to $E_T = n_1 E_1 + n_2 E_2 + \dots + n_M E_M$. We want to calculate the total number of ways to distribute the particles, assuming that each particle must be allocated in one of the M allowable states.

For the computation, we allocate n_1 particles in one of the M possible states, n_2 particles in one of the remaining $M - 1$ states and we continue in this manner until the last n_M particles are positioned in the last available state. In this way, there will be $n_1! \cdot n_2! \dots n_M = \prod_{i=1}^M n_i!$ possible configurations. However, as the configurations are indistinguishable among them, to attain the correct number of possible combinations, it is necessary to divide by $M!$. Therefore the total number of possible configurations, denoted by Y , is given as,

$$Y = \frac{\prod_{i=1}^M n_i!}{M!}. \quad (2.7.1)$$

Due to physical principles, it is expected that the parameter Y , given by equation 2.7.1, should take a maximum value, as suggested in reference [2.21]. Therefore, considering that each number n_i is large, this requirement is equivalent to maximize, instead, $\ln(Y)$, given as follows,

$$\ln(Y) = \ln(n_1! + n_2! + \cdots + n_M!) - \ln(M!). \quad (2.7.2)$$

Equation 2.7.2 will be maximized, subjected to the following constraints,

$$N_T = \sum_{i=1}^M n_i \quad \text{and} \quad E_T = \sum_{i=1}^M n_i E_i. \quad (2.7.3)$$

Equation 2.7.2 together with the equations given in 2.7.3 can be solved by using Lagrange multipliers, which will lead to the equation

$$\frac{n_i}{N_T} = \frac{e^{\lambda_2 E_i}}{\sum_{i=1}^M e^{\lambda_2 E_i}}. \quad (2.7.4)$$

Equation 2.7.4 represents the probability of an equilibrium system being in the state i . We also note in this equation that the constant parameter λ_2 must be negative for physical reasons. Therefore, it will be represented as $-\beta$. In what follows we will provide a heuristic approach to estimate the value of β .

In the following figure we depict a particle in a system travelling in an arbitrary direction towards the surface denoted as A.

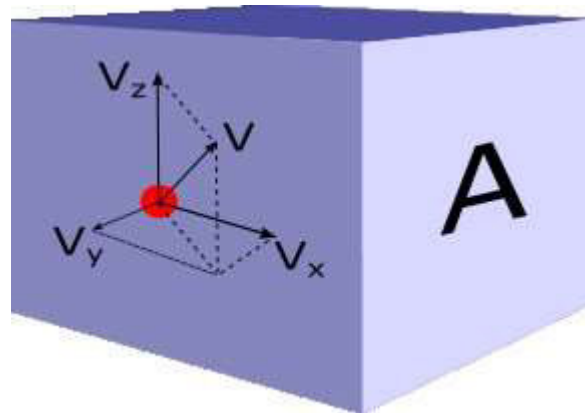


Figure 2.7.1. Diagram of a particle in a system travelling in an arbitrary direction towards the surface denoted as A).

In figure 2.7.1, the particle has velocities (v_x, v_y, v_z) and mass m . We will focus on the direction v_x of the particle. The particle will travel a distance Δx towards the surface depicted as A in a time Δt and will be reflected back a distance Δx in an additional time Δt . Under these conditions, the

particle will bear an initial momentum equal to $p = mv_x$ and after reflection, its momentum will be $p = -mv_x$. Therefore, the total momentum change will be $\Delta p = 2mv_x$ and it will take place in a time $t = 2\Delta t$. The corresponding force exerted on the surface will be $F = \Delta p / 2\Delta t$.

With the above conditions, and using $\Delta t = \Delta x / V_x$, the pressure on the surface A , $P = F / \Delta y \Delta z$, can be written as,

$$P = \frac{mV_x}{\Delta x \Delta y \Delta z}. \quad (2.7.5)$$

Noticing that in equation 2.7.5, $\Delta y \Delta y \Delta z$ represents the volume of the infinitesimal box, such that $pV = mV_x$.

To proceed with our heuristic approach, we will consider that the particle resembles an ideal gas following approximately the relation $pV = kT$, where k is the Boltzmann constant. Using this equation one obtains,

$$T = \frac{m}{k} \langle V_x \rangle. \quad (2.7.6)$$

In equation 2.7.6 the symbol $\langle * \rangle$ represents an average.

Using the results from equation 2.7.6, the expression of the number of particles n_i bearing energy E_i takes the form $n_i = e^{\lambda_1} e^{-\frac{\beta m}{2}(v_x^2 + v_y^2 + v_z^2)}$. This result leads to the equation of the temperature, represented by,

$$T = \frac{\frac{2m}{k} \iiint V_x^2 e^{-\frac{\beta m}{2}(v_x^2 + v_y^2 + v_z^2)} dV_x dV_y dV_z}{k \iiint e^{-\frac{\beta m}{2}(v_x^2 + v_y^2 + v_z^2)} dV_x dV_y dV_z}. \quad (2.7.7)$$

Solving the integrals involved in equation 2.7.12 we find that $\beta = \frac{1}{kT}$, such that the expression of the probability density function can be expressed as,

$$\frac{n_i}{N_T} = \frac{e^{-\frac{E_i}{kT}}}{\sum_{i=1}^M e^{-\frac{E_i}{kT}}}. \quad (2.7.8)$$

In equation 2.7.8 the denominator is referred to as the *Partition Function* [2.22], from the German word ‘Zustandsumme’, and it is typically represented by the letter Z as follows,

$$Z = \sum_{\text{all states}} e^{-\frac{E_i}{kT}} \quad (2.7.9)$$

We will see that the partition function, given by equation 2.7.9, will allow us to characterize our thermodynamic system.

Despite the approximations assumed in our previous derivations, it results that the equations obtained are in good agreement with experimental results reported in the literature.

From the partition function derived above, it is possible to obtain different thermodynamic properties. One such property is the free energy [2.21], and it is related to the partition function by means of the logarithm of the partition function as follows.

From equation 2.7.8, the expectation value of the energy is given by

$$\langle E \rangle = \sum_i^M E_i P_i. \quad (2.7.10)$$

In equation 2.7.10, P_i has been defined as n_i/N_T . Substituting equation 2.7.8 in equation 2.7.10 one obtains,

$$\langle E \rangle = \frac{\sum_i^M E_i e^{-\frac{E(\mu)}{kT}}}{\sum_i^M e^{-\frac{E(\mu)}{kT}}}. \quad (2.7.11)$$

Taking the natural logarithm of the expression of the partition function, equation 2.7.9, and taking its partial derivative with respect to $1/kT$ gives,

$$\frac{\partial \ln(Z)}{\partial \left(\frac{1}{kT}\right)} = \frac{1}{\sum_i^M e^{-\frac{E(\mu)}{kT}}} \sum_i^M (-E) e^{-\frac{E(\mu)}{kT}}. \quad (2.7.12)$$

In equation 2.7.12 the expectation value of the energy (average energy) has been related to the partial derivative of the natural logarithm of the partition function, with respect to the inverse of temperature. Therefore, the expectation value of the energy can be expressed as,

$$\langle E \rangle = - \frac{\partial \ln(Z)}{\partial \left(\frac{1}{kT}\right)}. \quad (2.7.13)$$

The partition function can also be related to thermodynamic variables. Usually, these variables are related through the entropy S . However, S is not as easily measured as P, V or T . For this reason, we define the Helmholtz free energy A , which provides a more convenient way to describe the properties of the system,

$$A = U - TS. \quad (2.7.14)$$

In equation 2.7.14, U represents the total internal energy of the system [2.23]. By dividing eq (2.7.14) by T , leads to $U = \partial A/T/\partial(1/T)$. Comparing this result with equation 2.7.14 one obtains,

$$A = -kT \ln Z. \quad (2.7.15)$$

The equation 2.7.15, relates the Helmholtz free energy with the partition function. From the free energy equation, given by 2.7.15, it is possible to determine the amount of work that the system performs in a thermodynamic process where the temperature is held constant.

Other important thermodynamic quantities, such as entropy, can be derived from the eq (2.7.14). The entropy can be calculated as

$$S = - \left(\frac{\partial(A)}{\partial T} \right)_{N,V} \quad (2.7.16)$$

Equation 2.7.16 relates the entropy of the system with the Helmholtz free energy, where the N and V are held constants.

In the following section we will use the statistical concepts represented by the above equations to introduce the concept of canonical ensemble.

2.10 Canonical ensemble

Let us consider a system characterized by temperature (T) and pressure (P), as the one shown in Figure 2.8.1, in which the system undergoes a process from state I to state II in two possible paths. In state I the system has free energy A_I and in state II A_{II} . The energy difference between two states can be written as [2.21]

$$A_{II} - A_I = \int_I dA = \int_{II} dA \quad (2.8.1)$$

Equation 2.8.1 shows explicitly that the difference of free energy is independent of the path followed by the system.

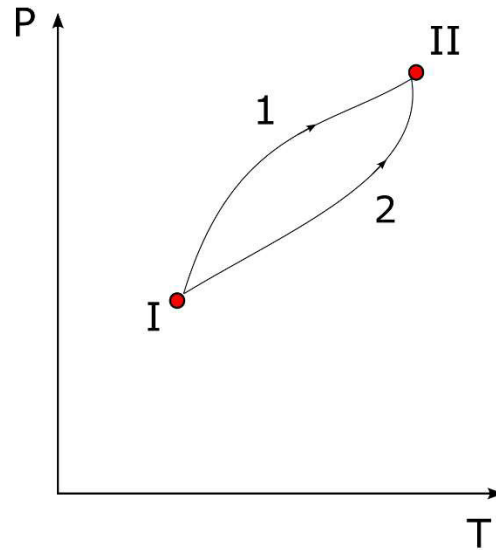


Figure 2.8.1 Two different paths between two points in the P-T space

To perform the calculations, in equation 2.7.1 it is necessary to explicitly write the dependence of the energy with respect to the variables of the system. For instance, if the variables are position and momentum, written as r^N and p^N , for the N-particle, the corresponding partition function can be written as

$$Z = \int e^{-\frac{E(r,p)}{kT}} dr dp. \quad (2.8.2)$$

Equation 2.8.2 is the continuous expression of the discrete expression given by equation 2.7.16. The space in which these states are represented is referred to as the phase-space, and it characterizes all possible states of a physical system. The energy E represents the total energy given by $E = K + U$ where K is the kinetic energy and U the potential energy.

Statistical mechanics utilizes ensembles, chosen based on specified macroscopic variables. Here, we will focus on the canonical ensemble, as it serves as the crucial link between statistical mechanics and thermodynamics, established through the partition function.

It is possible to calculate different averages over the phase-space, depending on the variables that are fixed. This leads to the concept of ensemble. The possible microstates a system could be in are known as the ensemble of states for a system [2.22]. An ensemble consists of a large collection of identical systems. The feature that distinguishes one type of ensemble from another is the communication allowed between the systems.

There are different types of ensembles. For instance, the microcanonical ensemble consists of identical systems, each system with the same energy E volume V and number of molecules N , and with the property that communication between systems is not allowed, i.e. there is no interchange of energy, so that the energy will remain constant as well as its volume and its number of molecules

[2.24]. Nothing is exchanged with the other systems in the microcanonical ensemble. The canonical ensemble is the same as the microcanonical with one exception: its systems are allowed to exchange energy in the form of heat. This exchange constitutes the communication among the systems of this ensemble, so that the temperature T , the number of molecules and the (average) energy become constant. As an example of a system where we fix the temperature, we suppose a system that is in contact with a reservoir, so that the latter and the system can exchange energy in the form of heat. This reservoir will allow to fix the temperature of the system while letting the energy fluctuate. A representation of this idea is depicted in the following figure

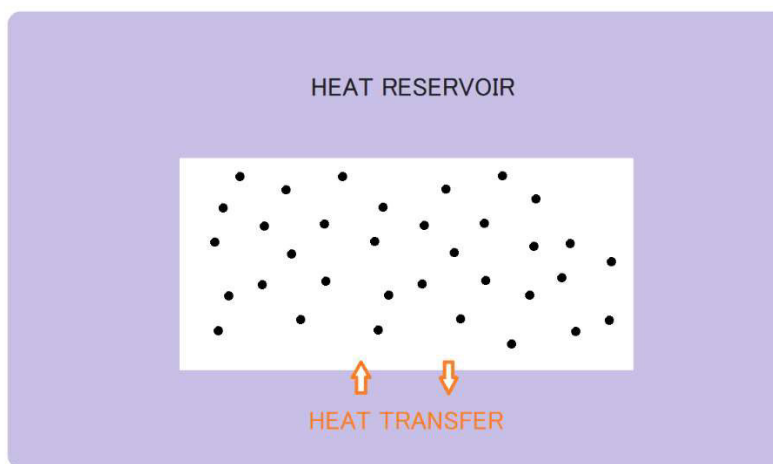


Figure 2.7.2 NVT ensemble where a heat transfer is allowed.

As we mention above, in the NVT ensemble, particles, volume, and temperature are kept constant. In this case, the system is allowed to exchange heat with outer space so that the temperature stays constant. We can imagine it as a system immersed in a giant reservoir or a thermostat. The system must remain closed, with no particle exchange and no work done over the reservoir or vice versa.

The goal of the simulation methods is to calculate macroscopic properties from microscopic properties, so the selection of the ensemble used in the simulation will depend on the properties and the type of system that will be studied. Typically, canonical ensemble is used in the study of phase diagrams, phase transition, among others [2.21].

Since we are interested in calculating structural properties, the simulations performed in this work will be carried out in the Canonical NVT ensemble as it will be described in the following chapters.

Chapter 3

3 Computational Simulation Method

As described in the last chapter, the probability density function given by equation 2.7.15, allows us to completely characterize a thermodynamical system. However, when the number of particles of a system is large, its evaluation becomes a complex task. As we will show in the following sections, a numerical method, referred to as Monte Carlo (MC), will provide an alternative approach to estimate the value of 2.7.15. In the following subsections we will focus on this method.

3.1 Monte Carlo method

To begin with, we will rewrite equation 2.7.15, substituting Z with 2.8.2, as,

$$P(E) = \frac{e^{-\frac{E(\mathbf{r}^N, \mathbf{p}^N)}{kT}}}{\int e^{-\frac{E(\mathbf{r}^N, \mathbf{p}^N)}{kT}} d\mathbf{r}^N d\mathbf{p}^N}. \quad (3.1.1)$$

In equation 3.1.1, we have moved from the discrete case to the continuous one by replacing n_i/N_T with $P(E)$, and additionally, we have expressed explicitly the energy as a function of the phase-space variables, $\mathbf{r}^N, \mathbf{p}^N$.

Equation 3.1.1 is the main equation to determine the macroscopic behavior of a thermodynamic system allowing us to compute expected values of observables; for example, in a ferromagnetic system, the average spin will measure the degree of magnetization.

To calculate the expectation value of an observable \mathcal{S} , we use the probability density function [3.1] given by equation (3.1.1), as follows,

$$\langle \mathcal{S} \rangle = \frac{\int \mathcal{S}(\mathbf{r}) e^{-\frac{E(\mathbf{r}^N, \mathbf{p}^N)}{kT}} d\mathbf{r}^N d\mathbf{p}^N}{\int e^{-\frac{E(\mathbf{r}^N, \mathbf{p}^N)}{kT}} d\mathbf{r}^N d\mathbf{p}^N}. \quad (3.1.2)$$

In equation 3.1.2, we have made explicitly the dependence of the observable $\mathcal{S}(\mathbf{r}, \mathbf{p})$ on the coordinates and momenta, however its expected value will be independent from them.

In general, equation 3.1.2 cannot be calculated analytically, therefore a numerical approach is necessary. However, when the number of particles of a system is large (>100), the calculation requires excessive processing time. Therefore, as mentioned above, the Monte Carlo method can be used as an appropriate alternative, reducing drastically the processing times. Furthermore, to

improve as possible the processing time, we will use a special scheme of the Monte Carlo method, introduced by Metropolis et al [3.2] and it will be described in the following section.

To apply the metropolis scheme, it is useful to notice that not all the points in phase-space contribute strongly to the calculation of the observable \mathcal{S} , due to low exponential values in equation 3.1.2. Therefore, it will be convenient to define a probability function $\rho(\mathbf{r})$, to sample points only when the exponential takes high values. The exponential in equation 3.1.2 will be referred to as the Boltzmann factor. The calculations will only be taken at high Boltzmann factors.

To introduce $\rho(\mathbf{r})$ in equation 3.1.2, we will proceed as follows.

First, we will rewrite equation 3.1.2 as,

$$\langle \mathcal{S} \rangle = \int \rho(\mathbf{r}) \frac{\mathcal{S}(\mathbf{r})}{\rho(\mathbf{r})} e^{-\frac{E(\mathbf{r})}{kT}} / Z d\mathbf{r}. \quad (3.1.3)$$

Now we will rewrite equation 3.1.3, as,

$$\langle \mathcal{S} \rangle = \int \rho(\mathbf{r}) \mathcal{S}^*(\mathbf{r}) e^{-\frac{E(\mathbf{r})}{kT}} / Z d\mathbf{r}. \quad (3.1.4)$$

In equation 3.1.4 we have defined $\mathcal{S}^*(\mathbf{r}) = \mathcal{S}(\mathbf{r})/\rho(\mathbf{r})$. The function $\rho(\mathbf{r})$ appears in equation 3.1.4 as a weight factor. In addition, we have dropped the dependence on \mathbf{p} since our simulations our variables will depend on the potential energy. In the following subsection we will describe how to apply this equation.

3.2 Metropolis Algorithm

We now apply the metropolis method to estimate the probability distribution $P(\mathbf{r})$ given in equation 3.1.1, where we have dropped the dependence on \mathbf{p} .

The integral in the denominator in equation (3.1.1) is complicated to calculate analytically [3.3]. Therefore, we proceed as follows.

First, to simplify our following description, we will replace the parameter \mathbf{r} by x , to consider a one-dimensional model. The generalization of this process for 3-dimensional systems is straightforward. Under these conditions, we notice that equation 3.1.1 can be written as,

$$P(x) = \frac{F(x)}{C}. \quad (3.2.1)$$

In equation 3.2.1 C represents a proportionality constant and for brevity we have defined $F(x) = \exp(-E(x)/kT)$.

The procedure consists of the following enumerated five steps.

- i) We will generate a sequence of numbers $\{x_N\} = (x_0, x_1, \dots, x_N)$ in such a way that, when N becomes large, the histogram of $\{x_N\}$ will resemble $P(\mathbf{r})$. The way this sequence of numbers is performed is referred to as a Markov chain. There are many ways of setting up a Markov chain that has this property. The Metropolis-Hastings algorithm is one of these.
- ii) We propose an initial arbitrary value for x_0 . From this value, we want to generate x_1 . The process continues this way until the final value. The values are obtained as follows.
- iii) We take a normal distribution with mean $\mu = 0$ and $\sigma^2 = 1$, denoted as $norm(0,1)$. From this distribution we calculate, $x_1 = x_0 + norm(0,1)$.
- iv) We take a uniform distribution between $(0,1)$ denoted as $unif(0,1)$. From this distribution we generate a number $q = unif(0,1)$.
- v) From the above values, we compare q with the ratio $F(x_1)/F(x_0)$. If the value of q is less than the ratio then $x_1 = x_0 + norm(0,1)$. Otherwise, $x_1 = x_0$. This process is repeated iteratively until the final element is calculated x_N .

A description of how the method works can be found in [3.4]. A summary of this description, which is based on the calculation of the probabilities of the acceptance ratios between two occurring events, follows.

We define acceptance probabilities of going from the state with value $x = a$ to a state with value $x = b$, and from $x = b$ to the state $x = a$, as $A(a \rightarrow b)$ and $A(b \rightarrow a)$, respectively.

As described above, we first assign an arbitrary value for x_0 and we try to assign a value to x_1 , taken from a random distribution. In general, this random value is taken from a normal distribution as $x_1 = x_0 + norm(0,1)$. This x_1 value is taken as a trial value to be tested. For this, we consider the following relation

$$A(a \rightarrow b) = \frac{F(b)}{F(a)} g(b|a). \quad (3.2.2)$$

Equation 3.2.2 indicates that the probability of acceptance of going from a state with value $x = a$ to a value $x = b$ is equal to the probability of the state $x = a$ multiplied by the conditional probability of getting the state $x = b$ given the state $x = a$,

Reciprocally,

$$A(b \rightarrow a) = \frac{F(a)}{F(b)} g(a|b). \quad (3.2.3)$$

Equation 3.2.3 gives the probability of acceptance of going from the state $x = a$ to the state $x = b$.

Taking the ratio between the two probability acceptances, equations 3.2.2 and 3.2.3 give,

$$\frac{A(a \rightarrow b)}{A(b \rightarrow a)} = \frac{F(b) g(a|b)}{F(a) g(b|a)}. \quad (3.2.4)$$

In equation 3.2.4, the algorithm is established for general conditions in which non-symmetrical distributions are considered. In these cases, $g(a|b) \neq g(b|a)$. These cases the algorithm is referred to as the Metropolis-Hesting method. When these distributions are symmetrical, the algorithm is simply known as Metropolis algorithm. These cases are more likely to occur in physical processes and it will be implemented in our simulations.

Under the above conditions, equation 3.2.4 can be simplified as

$$\frac{A(a \rightarrow b)}{A(b \rightarrow a)} = \frac{F(b)}{F(a)}. \quad (3.2.5)$$

In equation 3.2.5 we can consider two cases, $F(b)/F(a) < 1$ or $F(b)/F(a) \geq 1$.

For the first case, it must be accomplished that $A(a \rightarrow b) < 1$ and $A(b \rightarrow a) = 1$.

For the second case, we require that, $A(a \rightarrow b) = 1$ and $A(b \rightarrow a) < 1$.

The above cases can be written in only one equation as

$$A(a \rightarrow b) = \min\left(1, \frac{F(b)}{F(a)}\right). \quad (3.2.6)$$

To use equation 3.2.6, Metropolis et. Al [3.2], proposed to substitute the deterministic number one by a random number obtained from a uniform distribution between 0 and 1. Let us refer to this number as q . Then if q results less than the ratio $F(b)/F(a)$, the new value of the sequence is accepted. Otherwise, the new value is simply a copy of the old one.

To demonstrate that the Metropolis method works properly, we designed a Python program to generate two different probability density distributions e^{-x} and e^{-x^2} . These distributions were chosen arbitrarily for illustrative purposes. The examples show how the algorithm converges to the desired equilibrium distribution over time. A detailed explanation, along with the generated distributions and their comparisons with analytical expectations, is provided in Appendix I.

Now, we are in the position to use the Metropolis method to simulate the evolution of the movements of the particles in our system, in accordance with the probability represented by equation 3.1.1. The displacements of the particles will be carried out as follows.

First, we distribute the particles in a crystalline cell, represented by a cubic box of dimensions sides L . Next, the movement of each particle is according to the following pseudo code language.

Let N represent the total number of particles inside the box, then:

for ($n=1$, up to N , increase n in steps of 1)

{

```

num_part=random(from 1 to N); #Select one of the N particles in a random way
r_o=position of the selected particle; #Store the original value of the selected particle
E_0=exp(-U(r_0)_num_part)/(kT); #Calculate the energy corresponding to the selected particle
r_n=r_0+norm(0,1); # Select a trial position according to the description of the above section
E_n=exp(-U(r_n)_num_part)/(kT); #Calculate the energy corresponding to the selected particle
q=unif(0,1); #Generate a random value between 0 and 1 from a uniform distribution
if (q<E_n/E_0)
    accept the value of r_n
else
    r_n=r_0; #The trial value is not accepted, we keep the old value.
} # End of the for cycle

```

The pseudo code listed above can be used to displace the particles according to the probability density function that rules the system. From the position of the particles, we can follow the evolution of the system and track the different statistical parameters of interest such as the average energy, the mean square displacement, and others. In chapter 6 we present the results obtained with this scheme.

3.3 Radial Distribution Function

Now that we have devised a method to move the particles according to the probability density function that rules the system, we require a statistical measure that describes the spatial distribution between them. This parameter is usually the radial distribution function $g(r)$, which is a statistical representative that will allow to describe the structure of our liquid crystals [3.5]. This function provides the probability of finding a particle at a given distance from a reference particle, offering insights into the local structure of nematic and smectic phases. It is particularly useful for describing the presence of defects or disorders in these phases, providing the degree of deviation from perfect alignment.

Mathematically, the radial distribution function can be described as,

$$g(r) = \frac{1}{\rho N} \delta(|(\mathbf{r}_i - \mathbf{r}_j) - r|) \quad (3.3.1)$$

Where \mathbf{r}_i and \mathbf{r}_j represent the positions of particles i and j , respectively, N is the total number of particles and r is the radial distance between two particles.

A schematic representation of how $g(r)$ is computed is shown in the following figure:

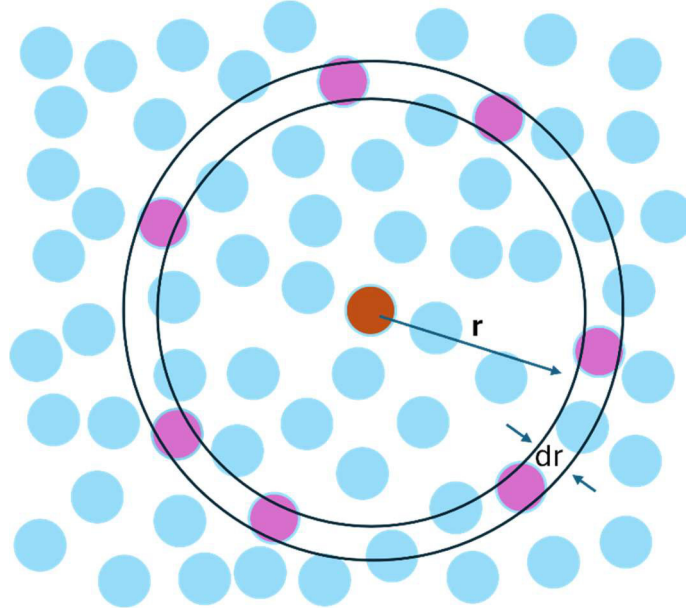


Figure 3.3.1 Schematic representation of the calculation of the radial distribution function $g(r)$. The reference particle is shown in orange, while neighboring particles within a shell of thickness dr are counted to compute $g(r)$.

Figure 3.3.1 illustrates the computation of the radial distribution function $g(r)$. To compute $g(r)$, a reference particle (orange) is selected, and concentric shells of thickness dr are constructed around it. The number of neighboring particles within each shell (purple) is then counted and normalized by the expected particle density in an ideal gas. Peaks in $g(r)$ indicate preferred distances between particles, revealing structural correlations in the system. In liquid crystals, anisotropic interactions lead to distinct features in $g(r)$, requiring separate calculations along parallel and perpendicular directions to the nematic director.

Following the same approach used to compute the radial distribution function $g(r)$, we define analogous distribution functions along the parallel and perpendicular directions relative to the director \mathbf{n} . These functions allow us to analyze positional correlations along different spatial directions, revealing structural ordering in anisotropic phases.

These functions are described as follows,

$$g_{\parallel}(z) = \frac{1}{N_r^2} \langle \sum \sum \delta(|(\mathbf{r}_i - \mathbf{r}_j) \cdot \mathbf{n}| - z) \rangle, \quad (3.3.1)$$

$$g_{\perp}(r) = \frac{1}{N_r^2} \langle \sum \sum \delta(|(\mathbf{r}_i - \mathbf{r}_j) \times \mathbf{n}| - r) \rangle. \quad (3.3.2)$$

In equations 3.3.1 and 3.3.2, \mathbf{r}_i and \mathbf{r}_j represent the positions of particles i and j , respectively. The unit vector \mathbf{n} denotes the nematic director. The delta function $\delta(\mathbf{r})$ ensures that only pairs separated by a distance z (parallel case) or r (perpendicular case) contribute to the summation.

These equations allow us to distinguish between positional correlations along the director (parallel case) and those in the perpendicular plane [3.6]. In practice, these functions provide a useful tool for detecting structural ordering and provide information of the formation of layers along the director vector, since it calculates the probability of finding particles at a certain distance from a reference point, confirming the formation of a smectic phase.

The following figure shows an example of $g_{\parallel}(z)$ for a LC system in the smectic phase:

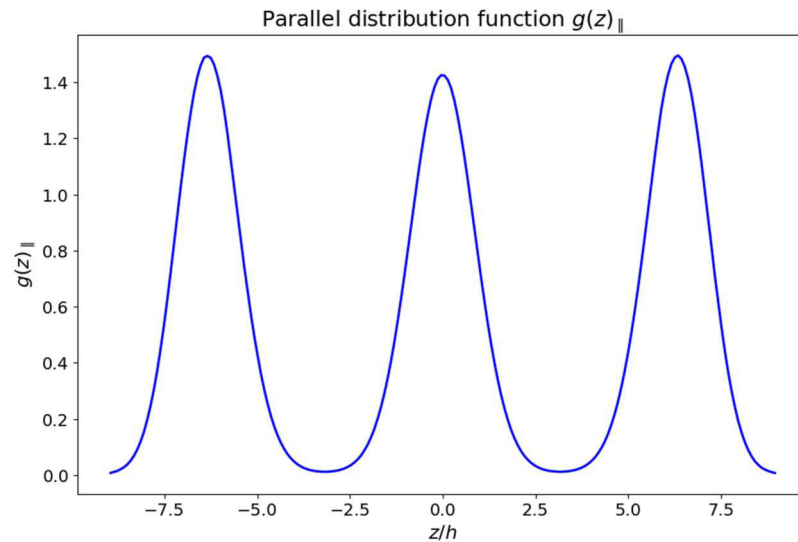


Figure 3.3.1 Parallel distribution function $g_{\parallel}(z)$ in a smectic phase, showing characteristic peaks associated with layer formation.

Figure 3.3.2 illustrates the parallel distribution function $g_{\parallel}(z)$ for a smectic phase. The presence of multiple peaks indicates the formation of well-defined layers along the director, with each peak corresponding to a preferred interlayer distance. The periodicity in $g_{\parallel}(z)$ confirms the existence of long-range positional order along the nematic director.

Although equations 3.3.1 and 3.3.2 are analytically correct for calculating $g_{\parallel}(z)$ and $g_{\perp}(r)$, they are not appropriate for programming purposes and their direct implementation in simulations requires a discrete approach using histograms. Therefore, we will use the approach proposed in [3.7], illustrated in the listing and pseudocode presented in Appendix 3.

This section provides the theoretical background necessary to analyze the structural properties of our simulated liquid crystal phases. The computed $g(r)$ will later be used to compare nematic and smectic structures, providing additional insight into their ordering.

Now, we will describe the periodic boundary conditions. For this we will refer to the following subsection

3.3.1 Additional details Periodic boundary conditions

In order to simulate bulk phases, it is important to choose correct boundary conditions to mimic the surroundings of our N -particle system [3.7]. The box volume that contains the particles will be treated as the primitive cell of an infinite lattice of identical cells. In figure 3.3.1, we depict a two-dimensional 3×3 -lattice, containing only two particles, denoted as A and B, for illustrative purposes. In this illustration, the primitive cell is the bottom left cell, and the other cells are replicas of the primitive one. We will use figure 3.3.1 to establish the pseudocode used in our simulations.

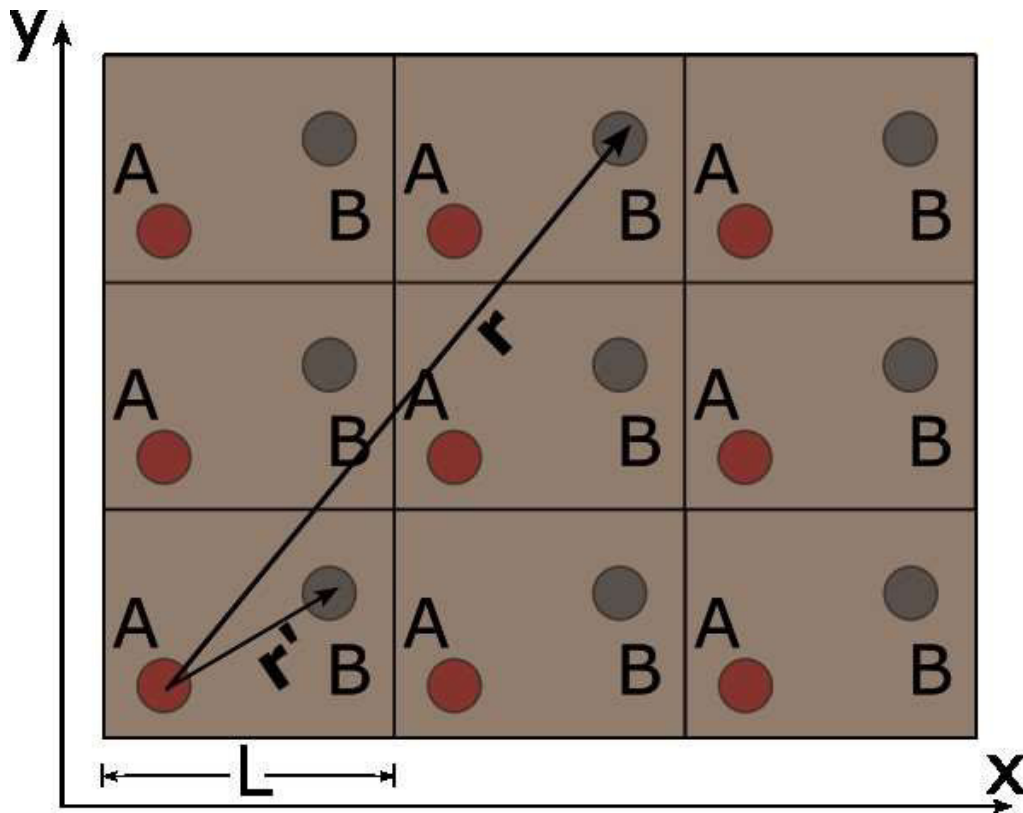


Figure 3.3.1. Boundary conditions considered to establish the pseudocode used in our simulations.

In figure 3.3.1 \mathbf{r} represents the vector joining particles A and B. However, as it can be appreciated, particle B is not in the primitive cell. However, due to periodicity, B must be in the primitive cell. Therefore, we have to consider, instead, vector \mathbf{r}' .

Let us denote $\mathbf{r}' = [x', y']$ and $\mathbf{r} = [x, y]$. The relationship between the coordinates of \mathbf{r}' and \mathbf{r} , is as follows: $x' = x - L \cdot \text{int}(x'/L)$ and $y' = y - L \cdot \text{int}(y'/L)$. These equations are used above, in the pseudocode of section 3.3.

To use the pseudocode, we have to introduce the interactive potential between the particles and their shape. In the following section we give details of our model.

3.4 Model and MC simulation details

The system studied in this work comprises $N_r = 1000$ rod-like particles with aspect ratio $L/\sigma=5$, where L and σ are the length and diameter of the rods, respectively as depicted in the following figure.

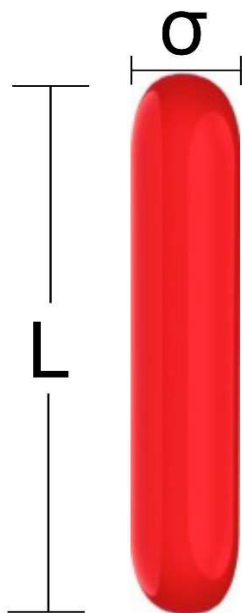


Figure 3.3.1 Model of a spherocylinder with aspect ratio $L/\sigma = 5$ and diameter σ .

For our long-range interaction simulations, the dipolar model system is also a soft spherocylinder with a point dipole oriented along the molecular axis.

We use kT , σ and $\tau = \sigma^2/D_0$ as our energy, length and time units, with k Boltzmann's constant, T the absolute temperature, $D_0 = kT/\eta_0\sigma$ a diffusion constant related to the solvent viscosity and η_0 the viscosity coefficient of the solvent [3.8].

The particles that we simulate in this work interact via a shifted and truncated Kihara potential. The interactions will take place only in the repulsive region of this potential. Its mathematical representation is as follows [3.9].

$$U_{ij}(\mathbf{r}_{ij}, \hat{\mathbf{u}}_i, \hat{\mathbf{u}}_j) = \begin{cases} 4\epsilon \left[\left(\frac{\sigma}{d_m} \right)^{12} - \left(\frac{\sigma}{d_m} \right)^6 + \frac{1}{4} \right] & d_m \leq \sqrt[6]{2}\sigma \\ 0 & d_m > \sqrt[6]{2}\sigma, \end{cases} \quad (3.3.1)$$

In equation 3.3.1 the subscripts i and j denote a pair of interacting particles where \mathbf{r}_{ij} represents the vector between their centers. The parameters $\hat{\mathbf{u}}_i$ and $\hat{\mathbf{u}}_j$ give their respective orientations. The strength of the interaction is set by a proportional term ϵ . This term represents the value of the depth of the potential, as depicted in figure 3.3.2. The value $\sqrt[6]{2}\sigma$ is the critical point between the attractive and repulsive regions. Therefore, if d_m is greater than this value, the potential vanishes, as indicated in equation 3.3.1, to neglect the attractive effect. For illustrative purposes this region is plotted in dashed line in figure 3.3.2. The dependence of U_{ij} on the parameters indicated in equation 3.3.1 comes from the parameter d_m which is by itself a function as follows, $d_m = d_m(\mathbf{r}_{ij}, \hat{\mathbf{u}}_i, \hat{\mathbf{u}}_j)$. Furthermore, Ref. [3.10] provides an algorithm to calculate the minimum distance between two spherocylinders.

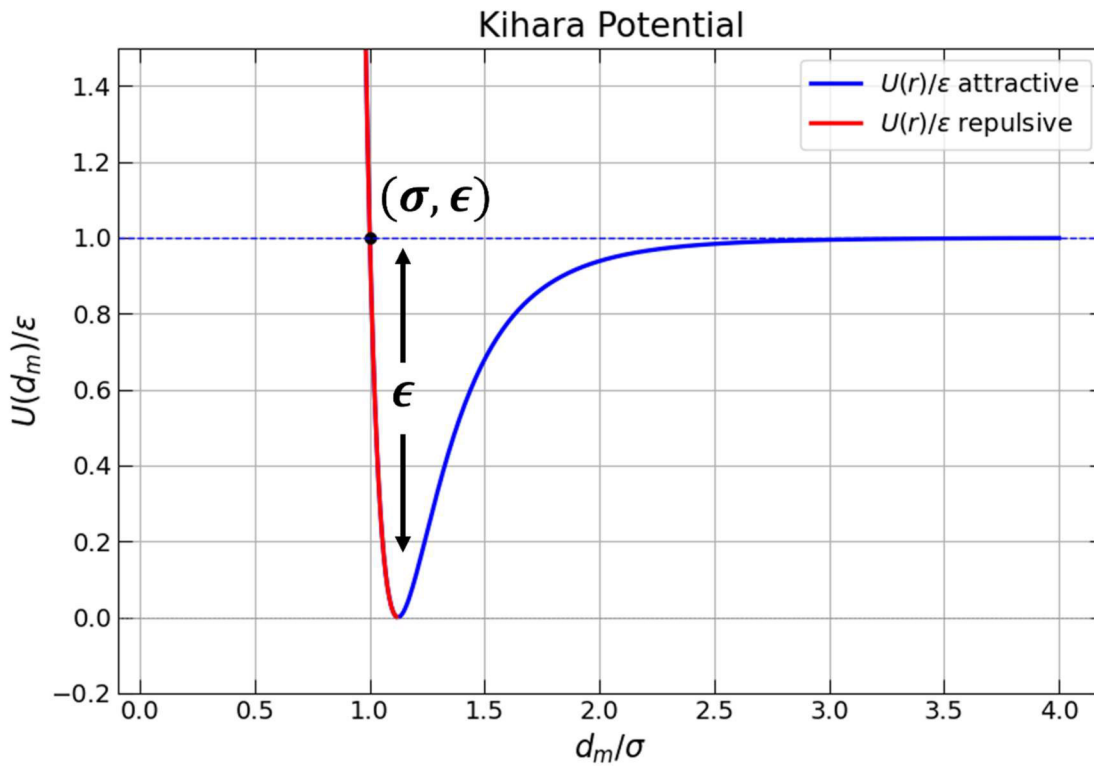


Figure. 3.3.2 Shifted and truncated Kihara potential as represented by equation 3.3.1, with parameters $\epsilon = 2$ and $\sigma = 0.6$. In our study, the attractive region will be considered equal to zero.

In figure 3.3.2 we have chosen arbitrarily parameters ϵ and σ , 2 and 0.6 respectively.

In this work we will apply the MC method to study two particular mesophases, nematic and smectic, in liquid crystals, interacting via the Kihara potential. For this study, we will choose five reduced temperatures $T^* = 5, 7, 10, 15$ and 20. The parameter T^* is defined as $T^* = kT/\epsilon$ (where T is the absolute temperature).

For the above task, we will make use of the packing fraction, defined as $\phi = N_r V_r/V$, where V_r is the volume of the rod, N_r the total number of rods and V is the volume of the box. The values

were chosen according to the phase diagram for soft-spherocylinders published by Cuetos & Martinez Haya in Ref. [3.11]. For illustrative purposes, in figure 3.3.3 we show the plot published in reference [3.11]. The packing fraction values for Nm and Sm phase are $\phi = 0.49$ and $\phi = 0.55$, were set, respectively, which correspond to densities of $\rho^* = 0.12$ and $\rho^* = 0.14$. With the previous initial conditions, NVT MC simulations were carried out to stabilize nematic and smectic phases at the three different temperatures.

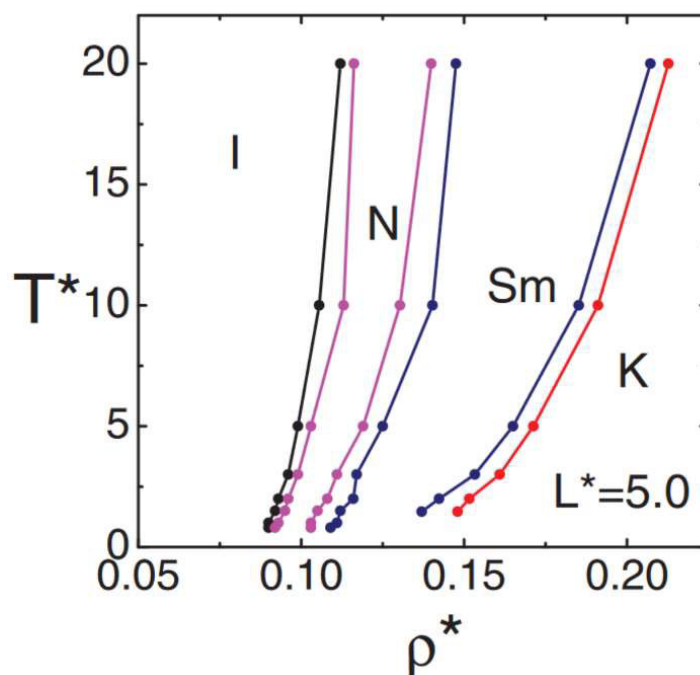


Figure 3.3.3. Phase diagram of spherocylinders for an aspect ratio $L/D = 5$. Taken from reference [3.11].

The above reference will allow us to set the initial conditions for our simulations. Once these values, the packing fractions and the reduced temperatures, have been set for our systems, we proceed to run several Monte Carlo simulations and we will calculate different functions such as the order parameter and distribution functions, in order to characterize the structural properties of the mesophases. We will report these results in chapter 6.

As mentioned above, another important quantity that appears in the study of the phase transition and will be reported in the structural results of liquid crystal phases, is the order parameter S_2 . It is the distinguishing feature of most phase transitions when the value of the parameter is nonzero. This parameter will be described in more detail in the following section.

3.5 Order parameter

The order parameter is a crucial concept in the study of liquid crystals. In liquid crystals, the order parameter is a measure of the degree of alignment or orientational order of the molecules in the material. This order parameter is an important characteristic that distinguishes liquid crystals from regular liquids. The value of the parameter is non-zero in the ordered phase but identically zero in the disordered phase.

The order parameter can be measured using various experimental techniques, such as X-ray scattering, polarized optical microscopy, and differential scanning calorimetry. The order parameter is a key factor in determining the behavior of liquid crystals, including their phase transitions and response to external stimuli.

The order parameter is often used to describe the behavior of liquid crystals in terms of their phase transitions. For example, when a liquid crystal undergoes a transition from a nematic phase to an isotropic phase, the order parameter drops to zero. Similarly, when a liquid crystal undergoes a transition from a smectic phase to a nematic phase, the order parameter increases.

The order parameter is also used to describe the behavior of liquid crystals in response to external stimuli. For example, when an electric field is applied to a liquid crystal, the order parameter can be modified, resulting in a change in the molecular alignment and other physical properties of the material.

The order parameter is defined differently in different kinds of physical systems. In a ferromagnet it is simply spontaneous magnetization. In a liquid–gas system it will be the difference in the density between the liquid and gas phases at the transition; for liquid crystals the degree of orientational order is telling. An order parameter may be a scalar quantity or may be a multicomponent (or even complex) quantity.

In our analysis we will use the scalar order parameter, and this parameter is defined as

$$S_2 = l_2(\cos\theta)$$

Where the l_2 the second Legendre polynomial [3.12].

The order parameter ranges from 0 (completely isotropic) to 1 (perfectly aligned). Typical values of order parameters for nematic and smectic liquid crystal phases can vary significantly depending on the specific material and conditions, for example, temperature, concentration, or external fields. However, general ranges for these order parameters are often used as references:

As we described in previous chapters, in the nematic phase, the liquid crystals exhibit long-range orientational order but no positional order. The order parameter quantifies the degree of alignment of the liquid crystal molecules relative to a preferred direction and typically, for well-ordered nematic phases, S_2 ranges from 0.5 to 0.8. For example, in many nematic liquid crystals, S_2 might be around 0.7 to 0.8 in the bulk phase.

In the smectic phase, as we described, the liquid crystals exhibit both long-range orientational order and partial positional order, organized into layers. There are several subphases of smectic liquid crystals, such as smectic A, smectic C and smectic B, each with different characteristics.

Values of the order parameter in the Sm phase typically are in the range of 0.8 to 1.0, reflecting the extent of layer formation [3.13].

3.6 *Dynamic Monte Carlo method*

The DMC method is based in the generation of random numbers to make the particles move based on a transition probability function in order to calculate dynamic properties such as the mean square displacements and the diffusion coefficients. In the DMC method, the time step and the maximum displacement of the particles are related through the short-time diffusion coefficients. This is accomplished in the limit of small displacements and using the Einstein equation for Brownian motion, that relates the mean square displacement of a particle with its diffusion coefficient, deduced in chapter 2. By rescaling the MC time step via its acceptance rate, a unique MC time scale is obtained making it possible to calculate dynamic properties at different time scales. [3.9]. A description of the DMC method applied in this work is available in references [3.14-3.16]

As mentioned, in DMC method a time scale for the displacements of the particles is defined and it can be related with the time scale for Brownian motion. This relation depends on the acceptance rate of the trial movements and the number of Monte Carlo cycles.

The acceptance rate is influenced by the displacement step size, for shorter displacements, the probability of accepting a move is higher, and the associated energy allowed between the movement in two states. If the change in energy corresponds to a permitted value, then the movement will be accepted with a probability according to its Boltzmann factor $e^{-\beta\Delta U}$.

Let's assume a particle j is situated at $x = 0$. The particle can be displaced to a new position within the interval $[-\delta x, \delta x]$. The probability of finding a particle in its initial position after a trial movement is $P_{rejected} = A'$. The probability of accepting the movement is $P_{accepted} = 1 - P_{rejected} = A$

A can be assumed to be constant within the interval $[-\delta x, \delta x]$, simplifying the mathematical treatment of the method.

This assumption is valid in the limit of infinite dilution or when displacements are infinitesimally small, as in these conditions the acceptance probability is expected to be independent of the step size. However, at high concentrations or when interactions between particles are strong, the acceptance probability may become highly dependent on the displacement step size. In these cases, deviations from the assumed constant A could affect the time scale calibration of the DMC method.

Making this simplified assumption, then the probability of moving the particle is $P_{move} = \frac{A}{2\delta x}$.

Thus, calculating the mean square displacement, we obtain the expression

$$\langle x^2 \rangle = \int_{-\delta x}^{\delta x} x^2 P_{move} dx = \frac{A(\delta x)^2}{3} \quad (3.6.1)$$

One can obtain a similar result for N particles performing C_{MC} cycles.

In this case the mean square displacement reads

$$\langle x^2 \rangle = C_{MC} \frac{A(\delta x)^2}{3} \quad (3.6.2)$$

In the case of rod-like particles with axial symmetry, there are 3 translational degrees of freedom corresponding to the displacement of the center of mass, and 2 rotational degrees of freedom associated with their orientation. The rotation around the particle's long axis does not affect its state and is therefore not considered a degree of freedom. In the general case of f degrees of freedom, a particle can be moved to a point $\xi = \xi_1, \xi_2, \dots, \xi_f$ belonging to an f -dimensional hyperprism of size $[-\delta\xi_k \delta\xi_k]$ with $k = 1, 2, \dots, f$. It is supposed that this move is accepted with uniform probability A . Similarly, for the case $f = 1$, the normalized probability of a displacement to any point reads

$$P_{move}(\xi) = \frac{A}{V_{\Xi}} \quad (3.6.3)$$

Where $V_{\Xi} = \prod_i^f (2\delta\xi_k)$ is the volume of the hyperprism. For this case the mean square displacement is given by

$$\langle \xi_k^2 \rangle = \int_{V_{\Xi}} \xi_k^2 P_{move} d\xi_k = \frac{A(\delta\xi_k)^2}{3} \quad (3.6.4)$$

Extending this result for the case of N identical particles we obtain,

$$\langle \xi_k^2 \rangle = C_{MC} \frac{A(\delta\xi_k)^2}{3} \quad (3.6.5)$$

Using the above result, it is possible to define a time unit for a DMC simulation defined as t_{MC} which can be related to the time unit of a Brownian dynamic simulation t_{BD} . During an MC step, the goal is to modify all the degrees of freedom of a randomly chosen particle at once. After this modification, the move is then accepted with probability A . Linking the displacements and rotations of a particle to a consistent temporal scale is effectively done through the Einstein relation for the diffusion coefficient, deduced in chapter 2. Using this equation and if the MC moves are statically independent, time and space are related as follows:

$$(\delta\xi_k)^2 = 2D_k \delta t_{MC} \quad (3.6.6)$$

Where D_k is the self-diffusion coefficient associated to the k th degree of freedom and δt_{MC} is the time needed to perform an MC cycle in the MC timescale. Using the above result allows us to obtain an expression of the mean square displacement, given by

$$\langle \xi_k^2 \rangle = \frac{2}{3} A D_k C_{MC} \delta t_{MC} \quad (3.6.7)$$

For a BD simulation its corresponding Einstein equation is given by

$$\langle \xi_k^2 \rangle = 2 D_k \delta t_{BD} \quad (3.6.8)$$

Combining equations (3.6.7) and (3.6.8) a relation between both timescales is obtained as follows:

$$t_{BD} = \frac{A}{3} C_{MC} \delta t_{MC} \quad (3.6.9)$$

The equation connects the timescales in BD and DMC simulations. However, it's crucial to note that Eqs. (6)-(8) hold true only under infinite dilution conditions, where the acceptance rate remains seemingly unaffected by the displacement size. Conversely, in cases of finite dilution, when particle collisions occur, these equations lose their exactness, yielding approximate outcomes.

It is important to notice that the maximum displacements must be small enough in order to have accurate equivalence between DMC and BD simulations but not extremely small so that it collects significant statistics in a realistic period of simulation time.

Equation (3.6.9) is the fundamental equation that will be used to rescale the simulation results, reported in chapter 6, to a unique time scale and will allow us to calculate dynamic properties, such as the self-diffusion coefficients of the system.

As mentioned in the previous section, to satisfy the requirement for the correct application of DMC, small displacements of the particles are required. These maximum displacements can be defined via the short-time diffusion coefficients of the particles.

In the DMC method, random displacements of the center of mass and rotations of the long axis of the particles will be performed. These maximum displacements and rotations can be related with the respective short-time self-diffusion coefficients via the time step δt_{MC} as it is shown in the following equations

$$\delta r_{\perp} = \sqrt{2 D_{\perp} \delta t_{MC}} \quad (3.6.10)$$

$$\delta r_{\parallel} = \sqrt{2 D_{\parallel} \delta t_{MC}} \quad (3.6.11)$$

$$d\theta = \sqrt{2 D_{\perp} \delta t_{MC}} \quad (3.6.12)$$

In equations (3.6.10-3.6.12) δr and $d\theta$ represent the displacements and the rotations respectively, while δt is the time over which the displacement occurs, and D is the corresponding self-diffusion coefficient.

It is important to distinguish between short-time and long-time diffusion coefficients. The diffusion coefficients derived here correspond to the short-time self-diffusion coefficients, which describe the initial motion of particles before significant interactions dominate and are obtained from the inverse of the friction coefficients in the infinite dilution limit as will be shown in the following paragraphs. In contrast, the long-time diffusion coefficients incorporate the effects of particle collisions and collective behavior, which modify the transport properties at longer timescales. The short-time diffusion coefficients derived in this section will be used to define the time step in the DMC method and to rescale the simulation results.

Since the short-time diffusion coefficients in equations [3.6.10-3.6.12] depend on the friction coefficients, it is necessary to introduce them first. Particles moving through a medium experience frictional drag, a force proportional to their velocity but in the opposite direction. This frictional force is determined by a friction coefficient, which depends on both the size and shape of the particles. These friction coefficients are inversely proportional to the diffusion coefficients, establishing a direct link between friction and particle mobility.

To compute the previously derived expressions for the maximum displacements and rotations, it is necessary to determine the diffusion coefficients in the limit of infinite dilution. These coefficients can be obtained using the expressions for the friction coefficients of particles with spherocylindrical geometry. In reference [3.17], the authors derive analytical expressions for the friction coefficients of particles with different shapes using the induced forces method. In their approach, the shape of the particles is described through the function,

$$h(x) = (1 - x^{2n})^{\frac{1}{2n}} \quad (3.6.13)$$

where the parameter n controls the particle geometry. When $n = 1$, the function describes spheroids, while for $n \rightarrow \infty$, it corresponds to straight cylinders. For intermediate values, such as $n = 8$, which will be used for our calculations, the particles resemble cylinders with rounded edges, making them more suitable for modeling rod-like particles.

The equations (3.6.14-3.6.16) express the friction coefficients perpendicular, parallel and rotational, in terms of $h(x)$, providing the necessary framework for calculating diffusion properties in rod-like systems.

$$\zeta_{\perp} = \frac{4\pi\eta_s L}{\ln \frac{2}{\epsilon} - \frac{1}{2} - \frac{1}{2} \int_{-1}^1 dx \ln h(x)} \quad (3.6.14)$$

$$\zeta_{\parallel} = \frac{2\pi\eta_s L}{\ln \frac{2}{\epsilon} - \frac{3}{2} - \frac{1}{2} \int_{-1}^1 dx \ln h(x)} \quad (3.6.15)$$

$$\zeta_r = \frac{\pi\eta_s L^2}{\ln \frac{2}{\epsilon} - \frac{1}{2} - \frac{1}{2} \int_{-1}^1 dx \ln h(x)} \left(\frac{\int_{-1}^1 dx \ln h(x)}{\ln \frac{2}{\epsilon} - \frac{11}{6} - \frac{3}{2} \int_{-1}^1 dx x^2 \ln h(x)} - 2\chi \right) \quad (3.6.16)$$

In equations (3.6.14-3.6.16), the parameter ϵ is defined as $\epsilon \equiv \frac{\sigma}{L}$ and $h(x)$ is a positive function and defined for $-1 \leq x \leq 1$ with n being a positive integer.

In the particular case of rod like particles $n = 8$. The integral that needs to be numerically solved for this case is expressed as

$$I \equiv \frac{1}{2} \int_{-1}^1 \ln h(x) dx \quad (3.6.16)$$

The result for I for $n = 8$ is $I = -0.0061$. This result allows us to calculate the value for each friction coefficient given in equations (3.6.14-3.6.16).

The corresponding short-time diffusion coefficient is given by the inverse of each corresponding friction coefficient, as follows

$$D_{\perp, \parallel, r} = \frac{1}{\zeta_{\perp, \parallel, r}} \quad (3.6.17)$$

By substituting the corresponding value of $D_{\perp, \parallel, r}$ in the Einstein's equations (3.6.10-3.6.12) the expression for the displacements and rotations are obtained.

Once we have calculated the mean square displacement through the DMC method our goal will be to carry out a rheological study of the systems, where we are interested in calculating the viscoelastic behavior of each phase to characterize the shear moduli and its dependence on the long-range interactions. This will be discussed in more depth in the rheology chapter.

3.7 Van Hove and intermediate scattering functions

The Van Hove function (VHF) and the intermediate scattering function (iSF) are two key functions for characterizing and understanding the dynamics of LCs. These functions provide insights into how particles move and interact over time and will be calculated in our simulations.

The VHF and iSF are the reciprocal time dependent functions for the radial distribution function and the structure factor, respectively.

The Van Hove function describes the probability density of finding a particle i at a position r at time t , given that a reference particle was at the origin at $t = 0$. This function is crucial for studying transport properties and microscopic motion, as it allows us to distinguish between localized and diffusive behaviors in complex fluids. By analyzing the VHF, we can determine whether particles remain close to their original positions, undergo typical diffusive motion, or exhibit anomalous transport mechanisms.

The VHF can be decomposed into two contributions. The self-VHF part $G_s(r, t)$ represents the probability distribution of displacements of the same particle over time, while the distinct-VHF $G_d(r, t)$ represents the probability of finding a particle i in the vicinity of r at a time t , knowing that a particle j is in the vicinity of the origin at a time $t=0$.

In this work, we focus exclusively on the self-part of the Van Hove function, given by

$$G_s(r, t) = \frac{1}{N} \delta\langle(r + r_i(0) - r_i(t))\rangle \quad (3.7.1)$$

Particularly for our study, instead of analyzing its time evolution, we evaluate it at a fixed time, as it will be reported in chapter 6. This approach allows us to examine the probability distribution of particle displacements over a specific timescale, revealing structural and dynamical characteristics of the system at that time.

Instead of considering correlations in space, one can perform a study in reciprocal space in Fourier components. The intermediate scattering function is defined as the Fourier transform of the Van Hove function

$$F(\mathbf{k}, t) = \int dk G(\mathbf{r}, t) e^{-i\mathbf{k}\cdot\mathbf{r}t} \quad (3.7.2)$$

Reciprocally to the case of VHF, iSF can be defined as a self and a distinct part. Where the self-part is given by

$$F_s(\mathbf{k}, t) = \int dk G_s(\mathbf{r}, t) e^{-i\mathbf{k}\cdot\mathbf{r}t} \quad (3.7.3)$$

Instead of Fourier transform, during the simulation the self-iSF function can be also directly computed from the trajectories of the particles by using following expression,

$$F_s(\mathbf{k}, t) = \frac{1}{N} \langle \sum_{j=1}^N \exp [i\mathbf{k}\cdot(r_j(t) - r_j(0))] \rangle \quad (3.7.4)$$

4 Microrheology in Liquid Crystals

4.1 Introduction to Microrheology

Microrheology refers to a set of techniques used to determine the viscoelastic properties of complex fluids at a microscopic scale. Unlike conventional bulk rheology, which measures the macroscopic response of a material to externally applied deformation [4.1], microrheology infers local viscoelastic moduli by analyzing the motion of tracer particles embedded in the medium. These methods overcome some limitations of bulk rheology, such as the need for large sample volumes and restricted frequency ranges, making them particularly useful for heterogeneous or small-scale systems [4.2].

Due to its versatility, microrheology has been applied in various fields, including biological and soft matter systems [4.1]. It has been used to study the viscoelastic properties of DNA solutions, where the mechanical response varies depending on molecular alignment under shear flow. In cell mechanics, microrheology has provided insights into the stiffness of the cytoskeleton and the local heterogeneity of intracellular environments. Additionally, it has been employed to monitor gelation processes in colloidal suspensions and to characterize flow behavior in microfluidic devices, where conventional rheometers are impractical.

Microrheology approaches can be broadly categorized into passive and active methods. Passive microrheology tracks the spontaneous thermal motion of probe particles to extract viscoelastic properties, whereas active microrheology applies controlled external forces to probe the mechanical response of the system [4.2][4.3]. Both approaches provide insights into key viscoelastic parameters, such as the complex shear modulus and the stress relaxation modulus, which are interconnected through well-established mathematical transformations.

These techniques are particularly relevant for colloidal liquid crystals, where anisotropic interactions lead to spatial variations in viscosity and elasticity. These materials exhibit viscoelastic behavior, meaning they combine properties of both solids and liquids. Their mechanical response is characterized by the complex shear modulus $G^*(\omega)$ [4.4], which depends on the frequency ω and is given by

$$G^*(\omega) = G'(\omega) + iG''(\omega) \quad (4.1.1)$$

where $G'(\omega)$, also called the storage modulus, represents the elastic component, which describes how the material stores energy when deformed and $G''(\omega)$, known as the loss modulus, represents the viscous component, which describes energy dissipation due to internal friction [4.5].

While microrheology is often applied in experiments, tracking the motion of probe particles in biological and colloidal systems, it can also be implemented in simulations. In this work, we implement microrheology within DMC simulations, introducing a tracer particle into the liquid crystal systems. By tracking its displacements over time, we infer local viscoelastic properties of the system, providing insight into its mechanical behavior at a microscopic scale.

4.1.1 Active vs Passive Microrheology

As mentioned, microrheology techniques can be classified into active and passive methods: Active microrheology involves applying external forces (e.g., electric or magnetic fields) to control particle motion and directly measure the material's response [4.2], while passive microrheology analyzes the thermal Brownian motion of tracer particles to infer material properties without applying external forces [4.3].

In passive microrheology, no external force is applied to deform the material. Instead, the characteristic frequency ω is determined by the time scales of Brownian motion of the probe particle:

At high ω we probe short-time dynamics, where the material may behave more elastically, while at low ω we probe long-time dynamics, where viscous effects dominate. Thus, the viscoelastic response is inferred without an imposed deformation frequency, making microrheology ideal for studying soft and biological materials.

In this work, we use passive microrheology, as it allows us to extract the local viscoelastic response of liquid crystal phases by tracking the motion of an embedded spherical probe particle in dynamic Monte Carlo simulations. Such method can be modified to include calculations of viscoelastic properties by adding a spherical tracer to the phases and analyzing its mean square displacement, giving results of the viscous and elastic moduli of the system. There are different approaches to analyzing the mean square displacement to obtain information of the viscoelastic coefficients. We have chosen an analytical approach that will be described in the next section.

4.2 Generalized Stoke-Einstein Relation (GSE)

The Generalized Stokes-Einstein Relation provides a theoretical framework to extract the viscoelastic modulus $G^*(\omega)$ from the MSD of a probe particle. The viscoelastic modulus can be obtained using the Fourier transform of the MSD

In classical diffusion theory, the diffusion coefficient D is related to viscosity η through the Stokes-Einstein relation:

$$D = \frac{kT}{6\pi\eta a} \quad (4.2.1)$$

Where k is the Boltzmann constant, T is the temperature and a is the particle radius.

However, in viscoelastic fluids, viscosity is not constant but depends on frequency. The generalized version of the equation connects the mobility of the probe particle with the complex shear modulus $G^*(\omega)$.

In the following paragraphs we will describe the expression that relates the viscoelastic moduli with the mean square displacement of the probe particle, which will be implemented in our simulations.

A full derivation of the generalized Stokes-Einstein equation in the Fourier frequency domain can be found in Mason et al. (2000). Here, we summarize the main steps.

First, the Langevin equation describes the motion of a spherical particle in a viscoelastic fluid and is given by

$$mv\dot{(t)} = f_R(t) - \int \zeta(t-t')v(t')dt' \quad (4.2.2)$$

where m is the mass of the probe particle, $v(t)$ its velocity, $\zeta(t)$ is a memory function describing the local viscoelastic response and $f_R(t)$ a Gaussian random force due to the Brownian motion.

Fourier transforming equation 4.2.2 allows us to obtain $v^*(\omega)$ in terms of the frequency in the Fourier space as,

$$v^*(\omega) = \frac{f(\omega) + mv(0)}{\zeta(\omega) + i\omega m} \quad (4.2.3)$$

Multiplying equation 4.2.3 by the factor $v(0)$ we obtain

$$\langle v^*(\omega)v(0) \rangle = \frac{f(\omega)v(0) + mv(0)^2}{\zeta(\omega) + i\omega m} \quad (4.2.4)$$

The causality of the function $f(\omega)$ guarantees that the following condition is satisfied

$$f(\omega)v(0) = 0$$

The equipartition theorem states that

$$m \langle v(t)v(t) \rangle = kT \quad (4.2.5)$$

Putting together equations 4.2.4 and 4.2.5 leads to the relation

$$\langle v^*(\omega)v(0) \rangle = \frac{kT}{\zeta(\omega) + i\omega m} \quad (4.2.6)$$

Therefore, we obtain the following form for the function $\zeta(\omega)$

$$\zeta(\omega) = \frac{kT}{\langle v^*(\omega)v(0) \rangle} \quad (4.2.7)$$

The Fourier transform of the mean square displacement is given by

$$\mathcal{F}\{\langle \Delta r^2 \rangle\} = \frac{6}{(i\omega)^2} \mathcal{F}\{\langle v^*(\omega)v(0) \rangle\} \quad (4.2.8)$$

Equation 4.2.8 leads to the relation

$$\zeta(\omega) = \frac{6}{(i\omega)^2} \frac{kT}{\mathcal{F}\{\langle \Delta r^2 \rangle\}} \quad (4.2.9)$$

The known stoke relation for the drag of a pure viscous fluid [4.2] is given by

$$\eta = \frac{\zeta(\omega)}{6\pi a} \quad (4.2.10)$$

Substituting equation 4.2.9 in 4.2.10 we obtain

$$\eta = \frac{kT}{(i\omega)^2 \pi a \mathcal{F}\{\langle \Delta r^2 \rangle\}} \quad (4.2.11)$$

The complex viscoelastic coefficient is given by

$$G^*(\omega) = i\omega\eta \quad (4.2.12)$$

This leads to the equation of the G^* modulus given by

$$G^*(\omega) = \frac{kT}{i\omega \pi a \mathcal{F}\{\langle \Delta r^2 \rangle\}} \quad (4.2.13)$$

Equation 4.2.13 is known as the generalized Stoke-Einstein equation and it relates the viscoelasticity of a fluid with the mean square displacement of the particles immersed in it. This equation will be used and implemented to the DMC simulation results of the MSD of the spherical probe particle, to calculate the viscoelastic modulus $G^*(\omega)$ of the LC systems, as reported in the results section.

4.3 *Mason Approach*

In this section, we are interested in describing the approach for measuring the viscoelasticity of a liquid crystal medium. There are many ways of representing linear viscoelasticity [4.6]. One of these ways is the so-called generalized Stokes-Einstein equations (GSE), mentioned in the last section, which can also be written as [4.7]

$$\tilde{G}(s) = \frac{kT}{\pi a s \mathcal{L}\{\langle \Delta r^2(t) \rangle\}}. \quad (4.3.1)$$

In equation 4.3.1, t represents time and s represents its corresponding Laplace coordinate. The operator \mathcal{L} represents the Laplace transform of the mean square displacement $\langle \Delta r^2(t) \rangle$. The parameter a represents the radius of the particles.

Equation 4.3.1 gives an analytical way to calculate the linear viscoelastic response of a fluid, by knowing the mean square displacement, of the particles of the fluid, $\langle \Delta r^2(t) \rangle$. This approach, however, cannot be made in a direct manner, since the data obtained from experiments and simulations are sampled over limited discrete times, due to the complexity of the acquisition

processing, leading to severe errors. An alternative approach proposed in [4.7] will be used in this work and described in this section.

The method consists in expanding the function $\langle \Delta r^2(t) \rangle$ in a Taylor series around a given time t_0 , as follows,

$$\langle \Delta r^2(t) \rangle = t^{\alpha(s)} [a_0 + a_1(t - t_0) + a_2(t - t_0)^2 + \dots]. \quad (4.3.2)$$

In equation 4.3.2, when $t = t_0$, gives,

$$\langle \Delta r^2(t_0) \rangle = a_0 t_0^{\alpha(s)}. \quad (4.3.3)$$

Taking only the first term in the series given by 4.3.2 and using equation 4.3.3 leads to,

$$\langle \Delta r^2(t) \rangle \simeq \frac{\langle \Delta r^2(t_0) \rangle}{t_0^{\alpha(s)}} t^{\alpha(s)}. \quad (4.3.4)$$

Now, we will substitute $t_0 = 1/\omega_0$ in equation 4.3.4. We obtain,

$$\langle \Delta r^2(t) \rangle \simeq \frac{\langle \Delta r^2\left(\frac{1}{\omega_0}\right) \rangle}{\left(\frac{1}{\omega_0}\right)^{\alpha(s)}} t^{\alpha(s)}. \quad (4.3.5)$$

Here, ω_0 represents a chosen characteristic frequency around which the Taylor expansion is performed. This choice facilitates the calculation, and the final expressions can be generalized to any frequency ω . Now we will take the natural logarithm at both sides of equation 4.3.5. We obtain,

$$\ln \langle \Delta r^2(t) \rangle \simeq \ln \langle \Delta r^2\left(\frac{1}{\omega_0}\right) \rangle + \alpha(s) \ln(\omega_0) + \alpha(s) \ln(t) \quad (4.3.6)$$

Taking the derivative respect with time on both sides of equation 4.3.6, gives

$$\alpha(s) \simeq \left. \frac{d \ln \langle \Delta r^2(t) \rangle}{d \ln t} \right|_{t=t_0}. \quad (4.3.7)$$

Equation 4.3.7 gives explicitly the value of $\alpha(s)$. We will leave this value pending to be used later in our calculations. Meanwhile, we rewrite the equation 4.3.5 as,

$$\langle \Delta r^2(t) \rangle \simeq \omega_0^{\alpha(s)} \langle \Delta r^2\left(\frac{1}{\omega_0}\right) \rangle t^{\alpha(s)}, \quad (4.3.8)$$

and focus in obtaining the Laplace transform of equation 4.3.8. For this we will use the following equation,

$$\mathcal{L}\{t^{\alpha(s)}\} = \frac{\Gamma(\alpha(s) + 1)}{s^{\alpha(s)+1}}. \quad (4.3.9)$$

Substituting equation 4.3.9 in equation 4.3.8 gives

$$\mathcal{L}\{\langle \Delta r^2(t) \rangle\} \simeq \omega_0^{\alpha(s)} \langle \Delta r^2 \left(\frac{1}{\omega_0} \right) \rangle \frac{\Gamma(\alpha(s) + 1)}{s^{\alpha(s)+1}}. \quad (4.3.10)$$

Substituting s by $i\omega_0$ in equation 4.3.10, gives

$$\mathcal{L}\{\langle \Delta r^2(t) \rangle\} \simeq \langle \Delta r^2 \left(\frac{1}{\omega_0} \right) \rangle \frac{\Gamma(\alpha(\omega_0) + 1)}{i\omega_0} i^{-\alpha(\omega_0)}. \quad (4.3.11)$$

Equation 4.3.11, will allow to rewrite equation 4.3.1 as,

$$\tilde{G}(\omega_0) = \frac{kT}{\pi a \langle \Delta r^2 \left(\frac{1}{\omega_0} \right) \rangle \Gamma(\alpha(\omega_0) + 1)} i^{\alpha(\omega_0)} \quad (4.3.12)$$

Writing $i^{\alpha(\omega_0)} = \cos \frac{\pi}{2} \alpha(\omega_0) + i \sin \frac{\pi}{2} \alpha(\omega_0)$, allows to write the real and imaginary parts, as well as the magnitude, of equation 4.3.12 as,

$$G'(\omega) = \text{Re}[\tilde{G}(\omega)] = \frac{kT}{\pi a \langle \Delta r^2 \left(\frac{1}{\omega} \right) \rangle \Gamma(\alpha(\omega) + 1)} \cos \frac{\pi}{2} \alpha(\omega) \quad (4.3.13)$$

$$G''(\omega) = \text{Im}[\tilde{G}(\omega)] = \frac{kT}{\pi a \langle \Delta r^2 \left(\frac{1}{\omega} \right) \rangle \Gamma(\alpha(\omega) + 1)} \sin \frac{\pi}{2} \alpha(\omega) \quad (4.3.14)$$

$$|\tilde{G}(\omega)| \approx \frac{k_B T}{\pi a \langle \Delta r^2 \left(\frac{1}{\omega} \right) \rangle \Gamma[1 + (\alpha(\omega))]} \quad (4.3.15)$$

Equations 4.3.13-4.3.15, characterize completely $\tilde{G}(s)$. As we have not imposed any restrictions on ω_0 , in these equations, we have replaced ω_0 by a general value ω .

The above equations will allow us to analytically calculate the viscoelastic response of our systems, where a tracer particle will be inserted in the fluid medium, assuming that the local viscoelastic modulus around the sphere is the same as the macroscopic viscoelastic modulus, as we will see in the results section.

4.4 Implementation of Microrheology in DMC Simulations

As previously stated, microrheology is a technique used to determine the viscoelastic properties of soft materials by tracking the thermal motion of embedded tracer particles. Unlike conventional rheology, which applies external forces to measure a material's bulk response, passive microrheology relies on the intrinsic Brownian motion of tracers to extract local viscoelastic

moduli. In this study, we implement a passive microrheology technique using dynamic Monte Carlo simulations to analyze the local viscoelastic response of the medium surrounding a spherical tracer within the liquid crystalline phases.

Our approach involves simulating a tracer embedded in a colloidal rod suspension to understand the influence of local structural arrangements on the system's linear viscoelastic properties. By focusing on both the elastic modulus $G'(\omega)$, and the viscous modulus $G''(\omega)$, obtained from $|\tilde{G}(\omega)|$, as the real and imaginary parts, respectively, we aim to study the relation between phase ordering and the viscoelastic behavior of the surrounding medium. In addition, we will explore the effects of long-range interactions by introducing dipoles into our simulations, allowing us to assess their impact on the viscoelasticity of the liquid crystalline phases.

To accomplish this, we first define the translational diffusion coefficient of the tracer at infinite dilution, D_t , which is estimated from the Stokes-Einstein equation. It is expressed as

$$D_t = \frac{D_0 \sigma}{3\pi d_t} \quad (4.4.1)$$

The diameter of the tracer used in the simulations is $d_t = 1\sigma$. A correlation between the tracer size and the viscoelastic response has been reported in previous works [4.8]. Based on this, we selected the appropriate tracer size to obtain accurate results.

We performed simulations containing $N_r = 999$ rods and $N_t = 1$ embedded spherical tracer. The packing fraction is given by $\phi = (N_r V_r + V_t/V)$ where $\sigma V_r = \pi\sigma^3/6 + \pi\sigma^2 L/4$ and $V_t = \pi d_t^3/6$.

For a system containing rods and a spherical particle, the Brownian dynamics time can be derived from the rescaling of the MC time of the individual components as follows

$$\delta t_{BD} = \frac{A_t}{3} \delta t_{MC,t} = \frac{A_r}{3} \delta t_{MC,r} \quad (4.4.2)$$

In equation 4.3.2, A_t and A_r represent the acceptance rates for the tracer and the rods, respectively. These rates are determined at fixed MC times $\delta t_{MC,t}$ and $\delta t_{MC,r}$. Although the two species in the simulations have different MC timescales, these must be rescaled to the same BD timescale. To achieve this, we establish a fixed MC time step for the rods and then calculate the MC time for the tracer as well as A_t and A_r until eq converges, with the following expression

$$\delta t_{MC,t} = \frac{A_r}{A_t} \delta t_{MC,r} \quad (4.4.3)$$

We set the values for the MC time of the rods as 10^{-3} and recalculated the MC time step for the tracer in each simulation with the eq anterior

We performed simulations where we calculated 5000 trajectories with 10^{-5} MC cycles to calculate the mean square displacements in each phase.

The MSD is used to calculate the viscoelastic response of the system, which can be derived from the shear moduli given by the equation deduce in the previous section and given in Ref. [4.5]

$$|\tilde{G}(\omega)| \approx \frac{k_B T}{\pi a \langle \Delta r^2 \rangle \left(\frac{1}{\omega}\right) \Gamma[1+(\alpha(\omega))]} \quad (4.4.4)$$

Similar as in our MC simulations described in previous chapters, we performed NVT simulations in a cubic box with periodic boundaries. Using equilibrium configurations, we investigated the dynamics of the tracer to calculate the coefficients $G'(\omega)$ and $G''(\omega)$.

The microrheology simulations provide insights into the complex interactions that influence the rheological characteristics of these phases. By examining these interactions, we enhance our

comprehension of the behavior of liquid crystalline phases. The results of this analysis will be detailed in the rheology results section.

5 Long- range interactions

There are two main approaches to studying long range interactions. The first one, is the so-called Ewald summation, in which the particles are constrained in a squared cavity. In this technique the total electrostatic energy of the system is divided into two parts: a short-range contribution that is computed directly in real space, and a long-range contribution that is calculated in reciprocal space [5.1]. By doing so, it efficiently accounts for the interactions between all charged particles in the system, regardless of their separation distance.

The second approach is the reaction field method, in which the particles are surrounded by a spherical cavity and a reaction field is produced due to the polarization of the dielectric medium [5.2]. In this work we are going to focus on the last method, and it will be implemented in the Monte Carlo simulations to study the long-range interactions within the liquid crystal particles.

Long-range interactions in physics and chemistry refer to forces that act between objects or particles over significant distances, typically extending beyond the immediate vicinity of the interacting entities. These interactions are characterized by their influence not being limited to short distances and often follow an inverse square law, meaning they decrease with distance but can affect objects far apart.

In the context of liquid crystals and computational simulations, long-range interactions are important in understanding the behavior of liquid crystals. Liquid crystal molecules exhibit long-range orientational order, where their orientations are correlated over relatively large distances. This behavior is influenced by intermolecular forces like dipole-dipole interactions, van der Waals forces, and Coulombic forces, which have a long-range nature. These interactions play a crucial role in maintaining the ordered structure and alignment of liquid crystal molecules.

In computational simulations, such as molecular dynamics or Monte Carlo simulations, accurately representing long-range interactions is essential for modeling the behavior of liquid crystals. Specialized techniques, like the methods previously stated. These methods account for the long-range nature of forces like electrostatic interactions, ensuring that simulations provide realistic insights into the behavior of liquid crystals.

Long-range interactions are fundamental in understanding the behavior of liquid crystals. In computational simulations of liquid crystals, accurately modeling these long-range interactions is critical for capturing their characteristic ordered structures and alignment, allowing researchers to predict and study the properties and behavior of these materials.

5.1 Dipolar potential

In this study we will use the reaction field method to calculate the long-range dipolar-dipolar interaction between the particles in the liquid crystal mesophases. The results obtained, considering these interactions, will allow us to characterize more precisely the viscosity of the liquid crystal mesophases, as it will allow to include in our simulations the formulas for the viscoelastic coefficients deduced in the previous sections. For these calculations we will require the analytical expression of the dipolar potential, which we will review briefly in the following paragraphs.

The analytical expression of an electric field due to two punctual charged particles forming a dipole is given in [5.3]. For convenience, a brief description follows.

Referring to figure 5.1.1, the electric field at point P can be written as,

$$\mathbf{E} = \frac{q}{4\pi\epsilon_0} \left\{ \frac{\mathbf{r} - \mathbf{r}_a - \mathbf{l}}{|\mathbf{r} - \mathbf{r}_a - \mathbf{l}|^3} - \frac{\mathbf{r} - \mathbf{r}_a}{|\mathbf{r} - \mathbf{r}_a|^3} \right\}. \quad (5.1.1)$$

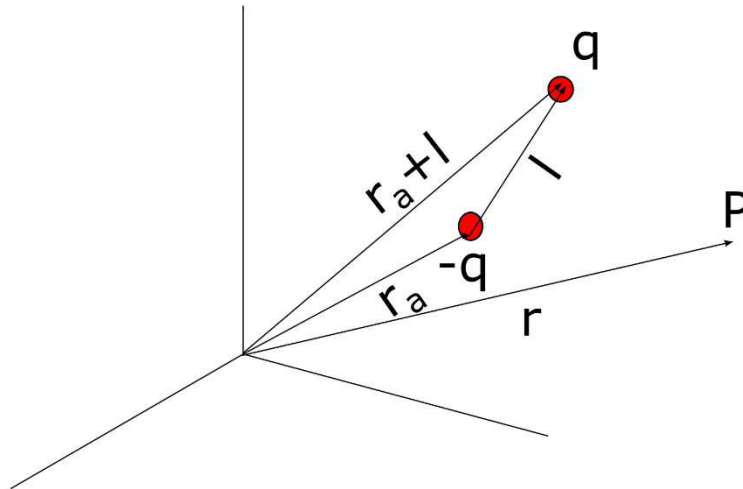


Figure 5.1.1 Two point particles with charge $+q$ and $-q$. The electric field due to these particles is calculated at P .

In figure 5.1.1, q and $-q$ are the charges of the positive and negative particles, respectively, positioned as depicted.

The denominator in equation 5.1.1 can be written as,

$$|\mathbf{r} - \mathbf{r}_a - \mathbf{l}|^{-3} = \{(\mathbf{r} - \mathbf{r}_a - \mathbf{l}) \cdot (\mathbf{r} - \mathbf{r}_a - \mathbf{l})\}^{-\frac{3}{2}}. \quad (5.1.2)$$

The dot product in equation 5.1.2 can be expanded in terms of $\mathbf{r} - \mathbf{r}_a$ as,

$$|\mathbf{r} - \mathbf{r}_a - \mathbf{l}|^{-3} = \{(\mathbf{r} - \mathbf{r}_a)^2 + l^2 - 2\mathbf{l} \cdot (\mathbf{r} - \mathbf{r}_a)\}^{-\frac{3}{2}}. \quad (5.1.3)$$

In equation 5.1.3, l^2 is very small, therefore 5.1.3 can be approximated to,

$$|\mathbf{r} - \mathbf{r}_a - \mathbf{l}|^{-3} = \{(\mathbf{r} - \mathbf{r}_a)^2 - 2\mathbf{l} \cdot (\mathbf{r} - \mathbf{r}_a)\}^{-\frac{3}{2}}. \quad (5.1.4)$$

Factorizing the term $(\mathbf{r} - \mathbf{r}_a)^{-3}$ in equation 5.1.4 gives,

$$|\mathbf{r} - \mathbf{r}_a - \mathbf{l}|^{-3} = (\mathbf{r} - \mathbf{r}_a)^{-3} \left\{ 1 - \frac{2\mathbf{l} \cdot (\mathbf{r} - \mathbf{r}_a)}{(\mathbf{r} - \mathbf{r}_a)^2} \right\}^{-\frac{3}{2}}. \quad (5.1.5)$$

Expanding into a Taylor series the right term of equation 5.1.5, leads to,

$$|\mathbf{r} - \mathbf{r}_a - \mathbf{l}|^{-3} = |\mathbf{r} - \mathbf{r}_a|^{-3} \left\{ 1 + \frac{3\mathbf{l} \cdot (\mathbf{r} - \mathbf{r}_a)}{|\mathbf{r} - \mathbf{r}_a|^2} \right\}. \quad (5.1.6)$$

Substituting equation 5.1.6 in equation 5.1.1, the electric field takes the form,

$$\mathbf{E} = \frac{q}{4\pi\epsilon_0} \left\{ |\mathbf{r} - \mathbf{r}_a|^{-3} \left\{ 1 + \frac{3\mathbf{l} \cdot (\mathbf{r} - \mathbf{r}_a)}{|\mathbf{r} - \mathbf{r}_a|^2} \right\} (\mathbf{r} - \mathbf{r}_a - \mathbf{l}) - \frac{\mathbf{r} - \mathbf{r}_a}{|\mathbf{r} - \mathbf{r}_a|^3} \right\}. \quad (5.1.7)$$

Equation 5.1.7 can further be rewritten as,

$$\mathbf{E} = \frac{q}{4\pi\epsilon_0} \left\{ \frac{\mathbf{r} - \mathbf{r}_a - \mathbf{l}}{(\mathbf{r} - \mathbf{r}_a)^3} + \frac{3\mathbf{l} \cdot (\mathbf{r} - \mathbf{r}_a)(\mathbf{r} - \mathbf{r}_a - \mathbf{l})}{|\mathbf{r} - \mathbf{r}_a|^5} \right\} - \frac{\mathbf{r} - \mathbf{r}_a}{|\mathbf{r} - \mathbf{r}_a|^3}. \quad (5.1.8)$$

Equation 5.1.8 can be written as,

$$\mathbf{E} = \frac{q}{4\pi\epsilon_0} \left\{ \frac{\mathbf{r} - \mathbf{r}_a - \mathbf{l}}{(\mathbf{r} - \mathbf{r}_a)^3} + \frac{-3\mathbf{l} \cdot (\mathbf{r} - \mathbf{r}_a)\mathbf{l} + 3\mathbf{l} \cdot (\mathbf{r} - \mathbf{r}_a)(\mathbf{r} - \mathbf{r}_a)}{|\mathbf{r} - \mathbf{r}_a|^5} \right\} - \frac{\mathbf{r} - \mathbf{r}_a}{|\mathbf{r} - \mathbf{r}_a|^3} \quad (5.1.9)$$

In equation 5.1.9 we can neglect terms of order of \mathbf{l}^2 , leading to,

$$\mathbf{E} = \frac{q}{4\pi\epsilon_0} \left\{ \frac{3\mathbf{l} \cdot (\mathbf{r} - \mathbf{r}_a)(\mathbf{r} - \mathbf{r}_a)}{|\mathbf{r} - \mathbf{r}_a|^5} - \frac{\mathbf{l}}{(\mathbf{r} - \mathbf{r}_a)^3} \right\}. \quad (5.1.10)$$

Finally equation 5.1.10 can be written as,

$$\mathbf{E} = \frac{q}{4\pi\epsilon_0} \left\{ \frac{3\mathbf{p} \cdot (\mathbf{r} - \mathbf{r}_a)(\mathbf{r} - \mathbf{r}_a)}{|\mathbf{r} - \mathbf{r}_a|^5} - \frac{\mathbf{p}}{(\mathbf{r} - \mathbf{r}_a)^3} \right\}. \quad (5.1.11)$$

In writing equation 5.1.11 we have defined $\mathbf{p} = q\mathbf{l}$, which represents the dipolar moment.

Finally, we will define a normalized vector $\mathbf{n} = \mathbf{r} - \mathbf{r}_a/|\mathbf{r} - \mathbf{r}_a|$. Therefore 5.1.11 can be written as,

$$\mathbf{E} = \frac{1}{4\pi\epsilon_0} \left\{ \left[\frac{3\mathbf{n} \cdot \mathbf{p}}{|\mathbf{r} - \mathbf{r}_a|^3} \right] \mathbf{n} - \frac{\mathbf{p}}{|\mathbf{r} - \mathbf{r}_a|^3} \right\} \quad (5.1.8)$$

Equation 5.1.8 gives explicitly the analytical expression for the electric field as a function of the \mathbf{p} , \mathbf{n} and \mathbf{r}_a . We will require this equation for the calculations of the reaction field that will be described in the following chapters.

5.2 Onsager reaction field

In the previous section we calculated the electric field \mathbf{E} at a point \mathbf{r}_0 due to a dipolar particle. This expression is given by

$$\mathbf{E} = \frac{3\mathbf{n}(\mathbf{p} \cdot \mathbf{n}) - \mathbf{p}}{|\mathbf{r} - \mathbf{r}_0|^3} \quad (5.2.1)$$

Where \mathbf{p} is the dipole moment of the particle and \mathbf{n} is the unit vector along the direction from \mathbf{r} to \mathbf{r}_0 .

The corresponding electric potential at \mathbf{r}_0 is given by

$$\phi(\mathbf{r}_0) = \frac{\mathbf{p}_1 \cdot \mathbf{n}}{|\mathbf{r} - \mathbf{r}_0|^2} = -(\mathbf{p}_1 \cdot \nabla)\psi_u \quad (5.2.2)$$

In equation 5.2.2, ψ_u is defined as

$$\psi_u(\mathbf{r}_0) = \frac{1}{|\mathbf{r} - \mathbf{r}_0|} \quad (5.2.3)$$

And the dipole operator is defined as

$$\mathcal{O}_p = -\mathbf{p} \cdot \nabla \quad (5.2.4)$$

For a second particle located at \mathbf{r}_2 interacting with the potential in equation 5.2.1, the interaction potential will be given by

$$\psi_0(\mathbf{r}) = -\mathbf{p}_2 \cdot \nabla \phi = -(\mathbf{p}_2 \cdot \nabla)(\mathbf{p}_1 \cdot \nabla)\psi_u \quad (5.2.5)$$

This expression indicates that the pair interaction between point dipoles is obtained by applying the dipole operator \mathcal{O}_p twice to equation 5.2.3

The potential ϕ must be a solution to the Poisson equation.

$$\nabla^2 \phi = -\frac{\rho}{\epsilon_0} \quad (5.2.6)$$

Where ρ is the charge density. This requirement is relevant when simulating systems interacting with the potential ψ_0 . Since this is a potential of a long-range nature, simulating systems interacting under the influence of this potential needs to include the surrounding mediums effects. The system that we will simulate will consist of the dipolar particles within the cell surrounded by a medium which interacts with the particles. To model these interactions, we will use the reaction field method.

To model the interaction with the surrounding medium, we transform the potential ψ_0 into an effective potential ψ_{eff} . This effective potential must be consistent with the Maxwell equations, and it also must approach ψ_0 as the number of particles N approaches infinity.

The effective potential ψ_{eff} can be described using the Green function $G(\mathbf{r}_1, \mathbf{r}_2)$. The general solution to the Poisson equation for a unit point charge inside a volume V is given by

$$G(\mathbf{r}_1, \mathbf{r}_2) = \psi_{eff} + F(\mathbf{r}_1, \mathbf{r}_2) \quad (5.2.7)$$

Where $F(\mathbf{r}_1, \mathbf{r}_2)$ satisfies

$$\nabla^2 F(\mathbf{r}_1, \mathbf{r}_2) = 0$$

The function $F(\mathbf{r}_1, \mathbf{r}_2)$ represents the potential of a system due to localized charges outside the volume V . For a dipolar system we can obtain similar results by applying the dipole operator twice to obtain

$$\psi_0 = \psi_{eff} + \psi_s \quad (5.2.8)$$

Where

$$\psi_{eff} = -(\mathbf{p}_1 \cdot \nabla)(\mathbf{p}_2 \cdot \nabla)G(\mathbf{r}_1, \mathbf{r}_2) \quad (5.2.8a)$$

And

$$\psi_s = -(\mathbf{p}_1 \cdot \nabla)(\mathbf{p}_2 \cdot \nabla)F(\mathbf{r}_1, \mathbf{r}_2) \quad (5.2.8b)$$

In the reaction field (RF) method, each dipole is surrounded by a spherical cavity filled with a continuum medium characterized by a dielectric constant ϵ_s . This medium is polarized by all dipoles within the cavity, creating a reaction field inside it. The interaction between a central dipole and another dipole within the cavity is described by the standard free-space interaction plus the additional energy from the reaction field. The interaction with dipoles outside the cavity is considered negligible, simplifying the simulation.

Since the particles inside the cavity will polarize the medium, in turn will create a reaction field that will interact with the particles. This field is called the reaction field.

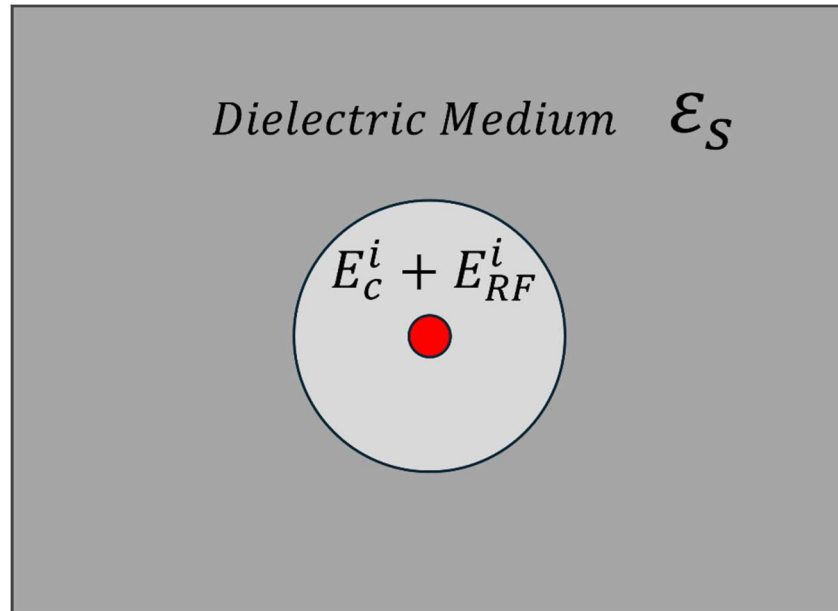


Figure 5.2.1 Dipolar particle surrounded by a dielectric medium with dielectric constant ϵ_s . The dipolar field and the reaction field are acting within the sphere.

In figure 5.2.1 ϵ_s is the dielectric constant of the surrounding medium, E_C is the electric field and E_{RF} is the reaction field.

The field E_{RF} interacting within the particles inside the cavity is given by

$$E_{RF}(0) = \left(\frac{\epsilon_s - 1}{2\epsilon_s + 1} \right) \frac{1}{R_c^3} \sum_j p_j \quad (5.2.9)$$

The energy of interaction between the central dipole and the reaction field is given by

$$\psi_i = -p_i \cdot E_{RF} \quad (5.2.10)$$

Where the contribution to the total energy due to the reaction field is given by

$$U_{RF} = \frac{1}{2} \sum_j \psi_j \quad (5.2.11)$$

The other contribution to U comes from the free space interaction ψ_0 between the central dipole and all the other dipoles inside the cavity, assuming that for dipoles outside the sphere the contribution is null.

The effective pair interaction associated with this model is

$$\psi_{eff} = \psi_0 - (\mathbf{p}_i \cdot \nabla)(\mathbf{p}_j \cdot \nabla) \left(\frac{\epsilon_s - 1}{2\epsilon_s + 1} \right) \frac{r_{ij}^2}{R_c^3} \#(5.2.12)$$

Which can be written as

$$\psi_{eff} = \psi_0 - \left(\frac{\epsilon_s - 1}{2\epsilon_s + 1} \right) \frac{\mathbf{p}_i \cdot \mathbf{p}_j}{R_c^3} \quad (5.2.13)$$

For $|r_{ij}| < R_c$ and $\psi_{eff} = 0$ for $|r_{ij}| > R_c$.

The potential is of the form of equations (5.2.8 (a-b)) so that we can identify a Green function that is obtained as the free space term plus a term that satisfies the Laplace equation inside the volume under consideration.

The simulation of dipolar systems interacting by the potential given by equation last can be carried out using aspherical truncation. This truncation must be done for $R_c < L/2$. The dielectric constant is another parameter that must be adjusted. A self-consistent method is a convenient way of making the method more efficient.

To carry out the self-consistent method we start by giving an arbitrary value to the dielectric constant and it is updated at regular intervals. For the calculation of ϵ_s , we will use the Clausius-Mossotti expression that is derived in the following paragraphs.

Let's start with the polarization vector in a medium that is defined as the dipolar moment per unit volume as,

$$P = \langle \frac{M}{V} \rangle = P_0 + (\nabla P) \cdot e_0 \quad (5.2.14)$$

Where P_0 denoted the initial polarization and e_0 is the external field vector.

The polarization can be calculated using the following expression

$$P = \frac{M}{V} \frac{\int e^{-\beta(T+U_{VDW}+U_E+e_0M)} d\mathbf{r}^N}{\int e^{-\beta(T+U_{VDW}+U_E+e_0M)} d\mathbf{r}^N} \quad (5.2.15)$$

Where we have defined the Hamiltonian \mathcal{H} as,

$$\mathcal{H} = T + U_{VDW} + U_E + e_0M \quad (5.2.16)$$

Where U_{VDW} is the energy related to the short-range interactions, U_E denotes the energy due to the dipole-dipole interactions and e_0M accounts for the reaction field energy. M represents the total dipole moment, and it is calculated by the sum of the individual dipoles as

$$M = \sum_{\alpha=1}^N \mu_{\alpha} \quad (5.2.17)$$

The partition function Z of the system is expressed as

$$Z = Z_{ideal} Q \quad (5.2.18)$$

Where Q is given by

$$Q = \frac{1}{V^N} \int e^{-\beta Z} dr^N \quad (5.2.19)$$

To simplify notation, we define the numerator of equation 5.2.15 as

$$G = \frac{M}{V} \int e^{-\beta \mathcal{H}} dr^N \quad (5.2.20)$$

To calculate the total polarization of the system given by equation 5.2.15, we first calculate ∇P

$$\nabla P = \nabla \left(\frac{G}{Q} \right) = \frac{\nabla G}{Q} - \frac{G}{Q^2} \nabla Q \quad (5.2.21)$$

Evaluating the necessary terms, we find

$$\nabla G = \beta \int \frac{M^2}{V} e^{-\beta \mathcal{H}} dr^N \quad (5.2.22)$$

And

$$\nabla Q = M\beta \int e^{-\beta \mathcal{H}} dr^N \quad (5.2.23)$$

Putting together results 5.2.22 and 5.2.23 into equation 5.2.21 we obtain ∇P is given by

$$\nabla P = \frac{\beta \int \frac{M^2}{V} e^{-\beta \mathcal{H}} dr^N}{\int e^{-\beta \mathcal{H}} dr^N} - \left\langle \frac{M}{V} \right\rangle \frac{\beta \int M e^{-\beta \mathcal{H}} dr^N}{\int e^{-\beta \mathcal{H}} dr^N} \quad (5.2.24)$$

This can be simplified to the form

$$\nabla P = \frac{\beta}{V} \{ \langle M^2 \rangle - \langle M \rangle^2 \} \quad (5.2.25)$$

Substituting this result into equation 5.2.14, we obtain

$$P = \langle \frac{M}{V} \rangle = P_0 + \frac{\beta}{V} \{ \langle M^2 \rangle - \langle M \rangle^2 \} \cdot e_0 \quad (5.2.26)$$

The polarization vector is related to the electric field E through the susceptibility X as

$$P = XE \quad (5.2.27)$$

For an isotropic medium, according to electromagnetism, the displacement D is given by

$$D = E + 4\pi P \quad (5.2.28)$$

Using together equations 5.2.27 and 5.2.28 we obtain

$$\epsilon E = E + 4\pi XE \quad (5.2.29)$$

The systems response to an electric field can be expressed as

$$P = P_0 + E \int \chi(r) dr \quad (5.2.30)$$

By comparing equations 5.2.30 and 5.2.26 and making an expansion around the external field e_0 , we find the following expression

$$\int \chi(r) dr = \frac{\beta}{V} \{ \langle M^2 \rangle - \langle M \rangle^2 \} \cdot e_0 \quad (5.2.31)$$

According to [5.4], for an isotropic dielectric medium, the susceptibility χ is expressed as

$$\chi(r) = I \frac{3}{4\pi} \left(\frac{\epsilon - 1}{\epsilon + 2} \right) \quad (5.2.32)$$

Inserting equation 5.2.32 into equation 5.2.31 we obtain

$$\left(\frac{\epsilon - 1}{\epsilon + 2} \right) = yg \quad (5.2.33)$$

Where y is usually defined as $4\pi\rho\mu^2/9kT$ and g is defined as $g = \frac{\beta}{V} \{ \langle M^2 \rangle - \langle M \rangle^2 \} \cdot e_0$

Equation 5.2.33 is the Clausius-Mossotti equation [5.4][5.5] where ϵ is the macroscopic dielectric constant of the material, ϵ_s is the static dielectric constant, which reflects the response of the material to an external electric field at low frequencies and yg represents a term related to the reaction field in the material. This equation will be implemented in the code to calculate the long-range interactions of the liquid crystal systems as we will see in the results section.

The Clausius-Mossotti equation describes how the material's ability to polarize in response to an applied electric field influences its overall dielectric behavior. This relationship is crucial for understanding the dielectric properties of materials and their response to external fields [5.6][5.7].

This equation along with the reaction field method, used in physics and chemistry, is a theoretical approach used to describe the influence of surrounding molecules or charges on a specific molecule or ion within a medium. It represents the collective effect of the environment on the properties of a solute, such as its electrostatic interactions or energetics. The reaction field accounts for the polarizability and charge distribution of the medium and is often used in the study of solvation, molecular interactions, and related phenomena, especially in the field of statistical mechanics and molecular simulations. This method will be implemented in the Monte Carlo simulations to add the long-range interactions acting between the colloidal particles.

In the following section we describe our simulation procedures and the results.

6 Results for the non-dipolar case

6.1 *Structural properties*

The first part of the study presented here consisted of performing MC simulations to stabilize the two different mesophases of the liquid crystals, nematic and smectic, referred to in the above chapters, to characterize their structure. To this end, MC simulations were carried out for five different temperatures $T^* = 5, 10, 15$ and 20 for both phases. The number of MC cycles was 10000 in each simulation. The equilibrium state was considered achieved when energy was stable within statistical fluctuations

We calculated structural properties, the radial distribution function along the parallel and perpendicular directions to the director vector to distinguish between the positional and orientational order of the particles and the order parameter the measure the degree of positional order [6.1].

The results for the distribution functions in parallel and perpendicular directions to the director are shown in Figures 6.1.1 and 6.1.2, respectively.

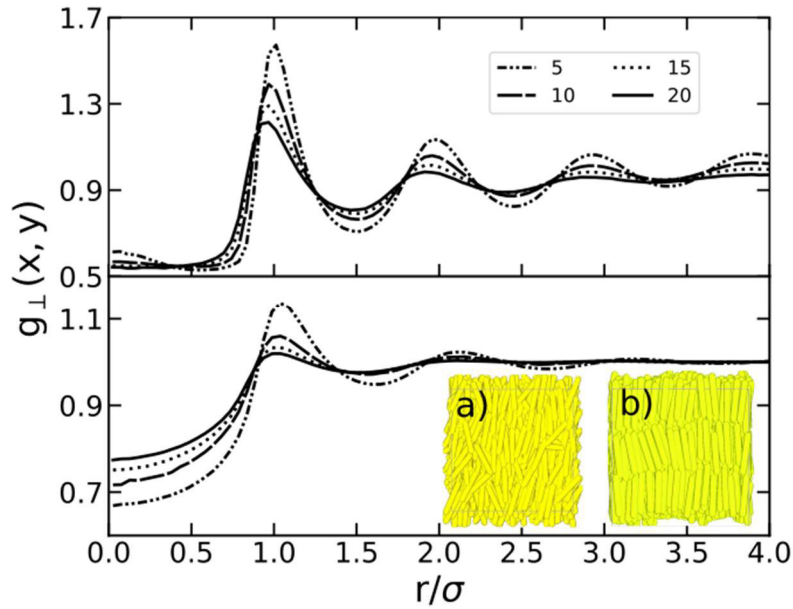


Figure 6.1.1 Pair correlation functions perpendicular to the nematic director. Nematic phase(top) and smectic phase(bottom) at $T^* = 5, 10, 15$ and 20 . Insets a) and b) in the bottom frame correspond to two representative states of the plots, taken at $T^* = 10$ for the nematic and smectic phases at densities $\rho^* = 0.12$ and 0.15 , respectively. The highest peak corresponds to the lowest temperature ($T^* = 5$), and the peak heights decrease progressively as temperature increases in both phases.

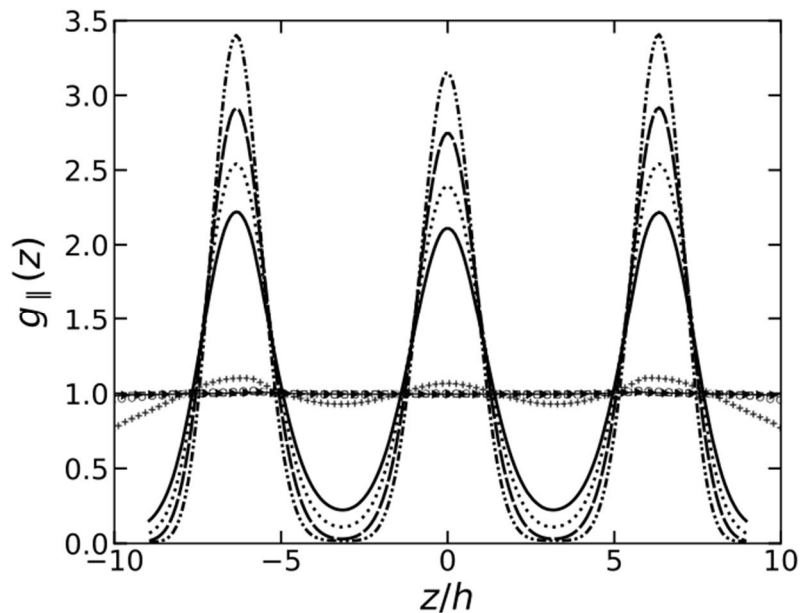


Figure 6.1.2 Distribution function in parallel direction to the nematic director at $T^* = 5, 10, 15$ and 20 . Dashed lines and symbols correspond to smectic and nematic phases, respectively. The highest peak corresponds to the lowest temperature and the peak heights

decrease progressively as temperature increases. Smectic phases exhibit more pronounced periodic peaks, while nematic phases show a smoother decay. Equilibrium densities are $\rho^* = 0.12$ and $\rho^* = 0.15$ for the nematic and smectic phases, respectively.

Densities are expressed in reduced units and defined as $\rho^* = \sigma^3 N/V$, where N is the total number of particles, V the volume of the system and σ the diameter of the rod.

Figure 6.1.1 reveals that both nematic and smectic phases resemble a typical fluid-like behavior in the perpendicular direction, with the first peak appearing at around one diameter length ($r/\sigma = 1$). After this point, the amplitude of the fluctuations decays exponentially, such that $g_{\perp}(x, y)$ stabilizes to a value of one approximately after three diameters length ($r/\sigma = 3$). As the temperature increases from $T^* = 5$ to 20, the peaks flatten, and the fluctuations decay at progressively shorter distances. This result is expected since higher temperatures lead to less ordered phases causing a smaller peak near the central particle. This behavior is similar for both phases.

Figure 6.1.2 shows periodic correlations that indicate the layered structure typically seen in smectic phases. It is observed the presence of three peaks for the smectic phases ($T^* = 5, 10, 15$ and 20) indicating the clear formation of layers, whereas in the nematic phases the function is almost a constant since in these phases the particles are not ordered in a layered structure.

In the smectic phase, each peak corresponds to a layer where particle density is at its maximum. In contrast, the spaces between layers are almost entirely empty, with a very low probability of finding particles in these regions.

Increasing the temperature significantly affects the density distribution in the smectic phase but has a negligible impact on the nematic phase, which shows no evidence of positional order at any of the studied temperatures.

We also calculated the order parameter for the different temperatures. These results are shown in the following table

T^*	S_2 Nematic	S_2 Smectic
5	0.87	0.96
10	0.86	0.96
15	0.84	0.94
20	0.82	0.93

Table 6.1.1. Order parameter (S_2) obtained for different reduced temperatures (T^*).

The results in table 6.1.1 show that the order parameter for nematic phases is lower than the corresponding one of the smectic phases, as expected. The order parameter also decreases with the temperature for both phases.

6.2 Dynamic properties

Now that we have established the structural differences between the nematic and smectic phases, we now examine how these distinctive morphological features affect their dynamic behavior.

As previously described, the system comprises $N=1000$ rods. The units used in our simulations for the time will be rescaled by a factor τ defined as $\tau = \sigma^2/D_0$, where $D_0 = k_B T/\mu\sigma$ is a diffusion constant and μ is the viscoelastic coefficient of the solvent.

To calculate the dynamic behavior of our systems, we first calculated the MSD in the direction parallel and perpendicular to the nematic director and after this, we calculated the long-time diffusion coefficients. To this end, we ran DMC simulations at different values of the MC time step, between $\delta t_{MC} = 10^{-5}$ and 10^{-2} , and then, we applied Equation (3.6.9) to rescale the results and recover the unique BD time scale [3.9]. The rescaled MSDs collapse into a single master curve as shown in Figure 6.2.1, where we report the parallel MSD in the smectic phase at $T^* = 10$.

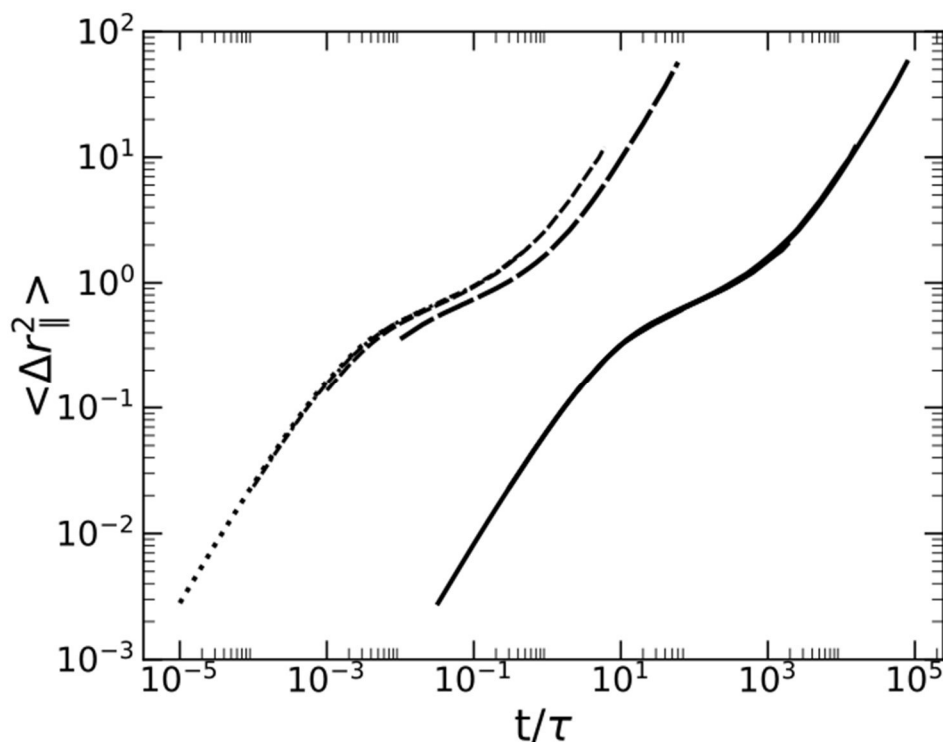


Figure 6.2.1 Mean square displacement in the smectic phase at $T^* = 10$ in the direction parallel to the nematic vector. Dotted, dashed and long-dashed lines refer to independent DMC simulations at $T^* = 5$, and $\delta t_{MC} = 10^{-5}$, 10^{-3} , and 10^{-2} , respectively. Solid lines have been obtained by rescaling the corresponding dashed lines according to Equation (3.6.9)

The re-scaling procedure to obtain the MSD across the whole spectrum of relevant time scales is the same for all the remaining systems.

The resulting master curve is obtained by superimposing four separate rescaled MSDs (dashed lines) calculated from DMC simulations at times $\delta t_{MC} = 10^{-5}, 10^{-4}, 10^{-3}$, and 10^{-2} . The calculated MSD shows an initial diffusive regime, primarily influenced by the particle geometry. This is followed by an intermediate time regime where the neighboring layers form a cage around the particles, slowing down diffusion. Finally, a long-time diffusive regime develops fully at $t/\tau > 1$, where the MSD exhibits linear behavior. Similar behavior has also been detected at the remaining temperatures $T^* = 5, 8, 12, 15$ and 20 with some differences observed in the extension of the cage effect and the onset of the long-time diffusive regime.

In particular, the effect of temperature on the MSD is clarified in figure 6.2.2, where we report parallel and perpendicular MSDs in nematic (top frame) and smectic (bottom frame) LCs at $T^* = 5$ and 20 , that are the lowest and highest temperatures studied.

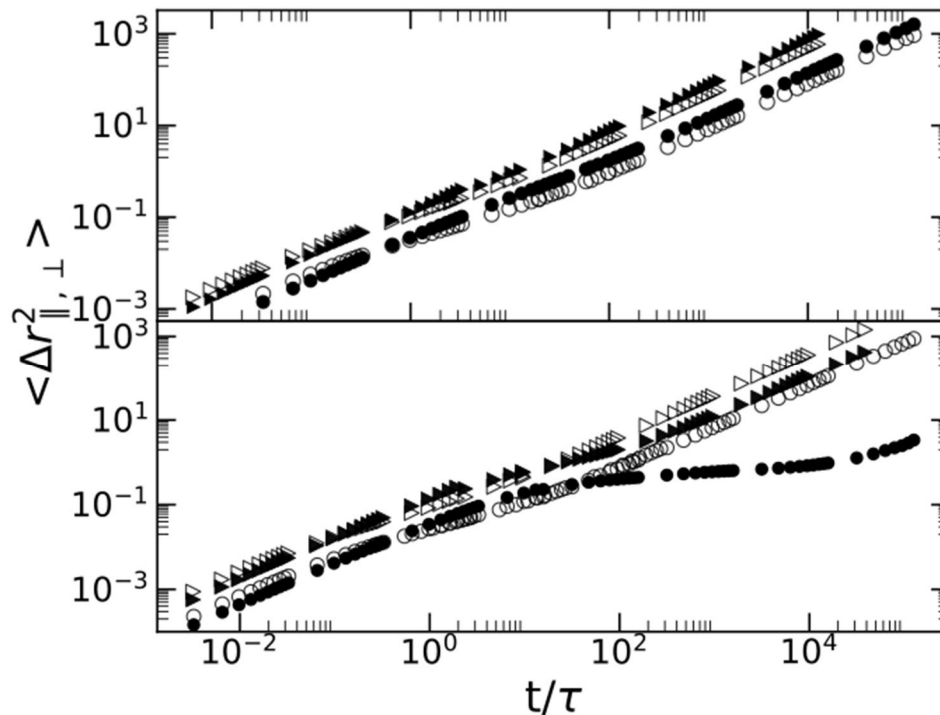


Figure 6.2.2. Mean square displacements in nematic (top frame) and smectic (bottom frame) LCs at $T^* = 5$ (circles) and $T^* = 20$ (triangles). Open and solid symbols refer to perpendicular and parallel direction, respectively.

To appreciate better the behavior of the plots, we do not show the parallel and perpendicular MSDs at intermediate temperatures, which exhibit a profile in between those reported in figure 6.2.2 for nematic and smectic phases.

We also notice that, in the nematic phase, at short time scales the relationship between parallel and perpendicular MSDs is such that $\xi \equiv \Delta r_{\perp}^2 / \Delta r_{\parallel}^2 > 1$, while it inverts at intermediate time scales, when the parallel MSD becomes larger and stays so up to the long-time diffusive regime. This behavior has also been reported in Brownian dynamics simulations of soft repulsive rods at $T^* = 1.465$ [6.2], a temperature at which the phase behavior of soft spherocylinders can be mapped on that of hard spherocylinders [6.3]. The dominant character of the long-time parallel diffusion has also been observed experimentally in N phases of rod-like viruses [6.4], but less clear is whether this tendency already exists at short time scales as observed in simulations. To gain an insight into the effect of temperature on the ratio between perpendicular and parallel diffusivities, we have calculated the time when the crossover from $\xi > 1$ to $\xi < 1$ is observed. Such an inversion time, referred to as t_i , does indeed change with temperature and the results are shown in figure 7.2.3.

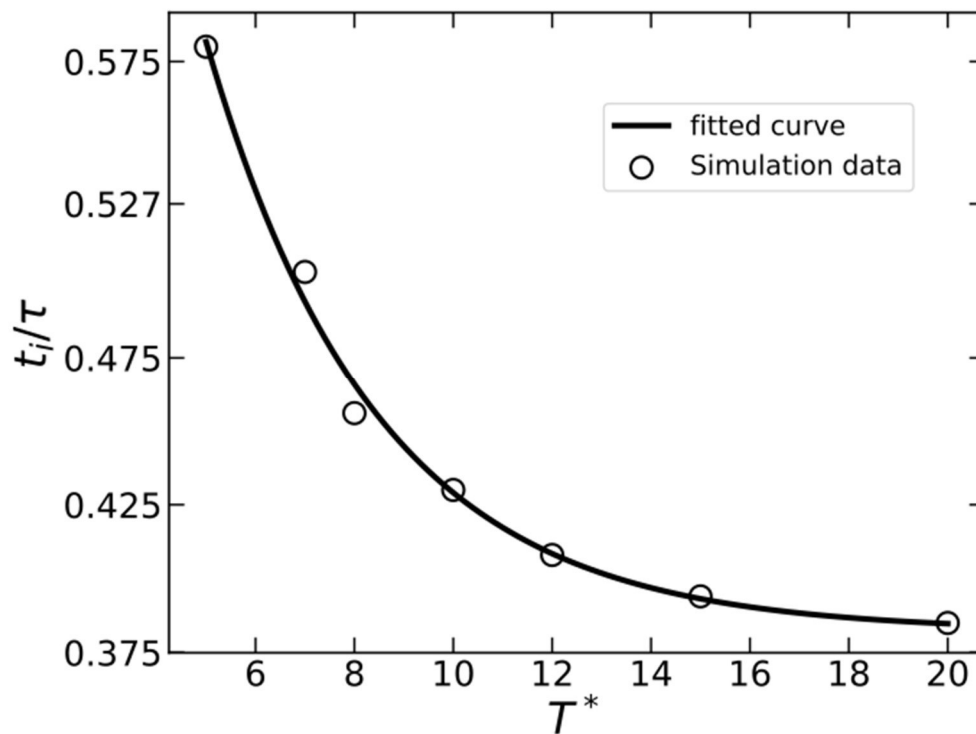


Figure 6.2.3 Inversion time between parallel and perpendicular MSD of the nematic phase. Symbols correspond to simulation results and the solid line is a fitting exponential function.

We observe that t_i is relatively large at low temperatures and then gradually decreases following an exponential law of the type $t_i/\tau = A + B \exp(-CT)$, where $A = 0.40$, $B = 1.51$ and $C = 0.37$ are fitting parameters. It is evident that at large enough temperatures, t_i tends to a constant value, approximately equal to 0.40τ , that will not change significantly up to the isotropic-nematic transition temperature.

6.3 Self-diffusion

The MSDs are used to calculate the long-time self-diffusion coefficients and their dependence on temperature. More specifically, parallel and perpendicular self-diffusion coefficients in N and Sm phases were obtained from the slope of the corresponding MSDs in the long-time diffusive regime:

$$D_{\parallel,\perp} = \lim_{t \rightarrow \infty} \frac{1}{2d} \frac{d \langle \sum [r_i(t) - r_i(0)]^2 \rangle}{dt} \quad (7.3.1)$$

where $d = 1$ or 2 denotes the dimensionality of particle dynamics associated to the parallel or perpendicular MSD, respectively. By contrast, the total self-diffusion coefficient has been calculated as $D_T = (D_{\parallel} + 2D_{\perp})/3$. The dependence of the self-diffusion coefficients on temperature in N and Sm phases is presented in the two frames of Figure 6.3.1.

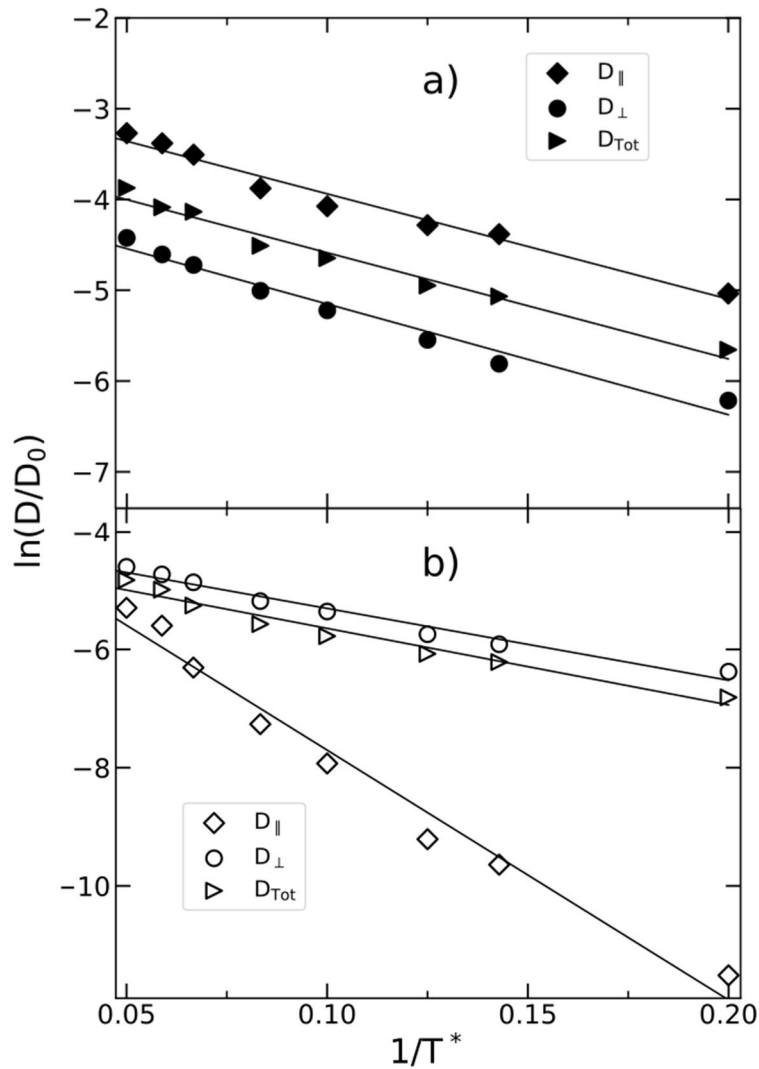


Figure 6.3.1 Total (D_T), parallel ($D_{||}$) and perpendicular (D_{\perp}) self-diffusivities, represented with triangles, squares and circles, respectively, as a function of the reduced temperature in the N (a) and Sm (b) phases. Solid lines are exponential fits of the type $D/D_0 \approx D^* \exp(E^*/T^*)$, with $D^* = \{0.0621, 0.0196, 0.0328\}$ and $E^* = \{11.5901, 12.1927, 11.6009\}$ for parallel, perpendicular and total self-diffusivities, respectively, for the nematic states, and $D^* = \{0.0308, 0.0167, 0.0129\}$ and $E^* = \{42.243, 12.1584, 12.948\}$ for parallel, perpendicular and total self-diffusivities, respectively, for the smectic states.

In agreement with previous molecular dynamics simulation of liquid crystals [6.5], we find that the three sets of long-time self-diffusion coefficients exhibit a dependence on T^* that is well-described by an Arrhenius-like exponential law, that reads $D/D_0 \approx D^* \exp(E^*/T^*)$, with the preexponential factor D^* and activation energy E^* fitting parameters. We also observe that the dependence of D_{\perp} on temperature is very similar in both N and Sm phases. At a given temperature, most likely due to the packing difference between the two LC phases, the numerical value of D_{\perp} is slightly larger in the N phase than in the Sm phase, but otherwise $D_{\perp} = D_{\perp}(T)$ exhibits the same exponential trend, with very similar fitting parameters, in both frames of Figure 6.3.1.

On the other hand, the diffusion along the director is significantly slower in the Sm phase ($E^* \approx 42$) than in the N phase ($E^* \approx 11$) by almost one order of magnitude, most likely due to the layered structure that hampers the penetration of the rods and thus delays their diffusion along the nematic director. These findings are in qualitative agreement with former theoretical, simulation and experimental works that clarified the existence of free-energy barriers hampering the diffusion of rod-like particles through Sm layers [6.6–6.11].

Therefore, while SRS particles in the N phase preferentially diffuse in the direction of the nematic director, in the Sm phase they are essentially constrained in a two-dimensional space, especially at $T^* < 10$, where D is almost negligible.

6.4 The Van Hove function

We now turn our attention to the probability of observing particles that displace significantly shorter or longer distances than the average particles over the same period of time. The existence of such particles, here referred to as fast or slow, is corroborated by the computation of the s-VHFs along the nematic director and perpendicularly to it, as given, respectively, in the following equations

$$G_s(r, t) = \frac{1}{N_r} \left\langle \sum_{j=1}^N \delta(z - [z_j(t + t_0) - z_j(t_0)]) \right\rangle \quad (7.4.1)$$

$$G_s(r, t) = \frac{1}{N_r} \left\langle \sum_{j=1}^N \delta(r - [r_j(t + t_0) - r_j(t_0)]) \right\rangle \quad (7.4.2)$$

Where z and $r \equiv \sqrt{x^2 + y^2}$ are the particle center-to-center distances in the direction of n and perpendicularly to it, respectively, and δ is the Dirac delta function.

To illustrate these calculations, we show the s-VHFs at $t/\tau = 10^4$, a time that is sufficiently long to observe the relevant dynamical features of both N and Sm phases across the whole spectrum of temperatures studied. These results for the s-VHF for N and Sm phases in parallel and perpendicular direction, respectively, are shown in Figures 6.4.1 and 6.4.1

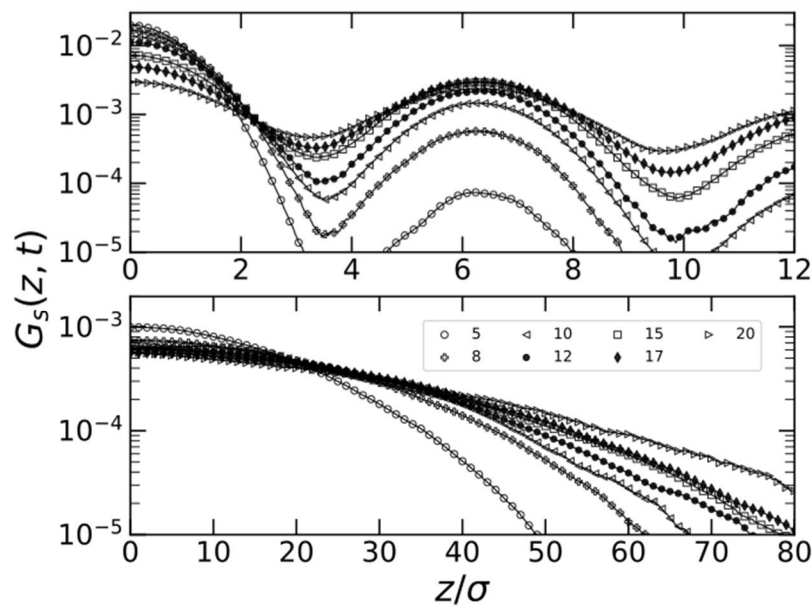


Figure 6.4.1 Self-part of the van Hove function at a time $t/\tau = 10^{-4}$ in N (bottom) and Sm (top) phases along the nematic director at scaled temperatures $T^* = 5, 8, 10, 12, 15, 17$ and 20 .

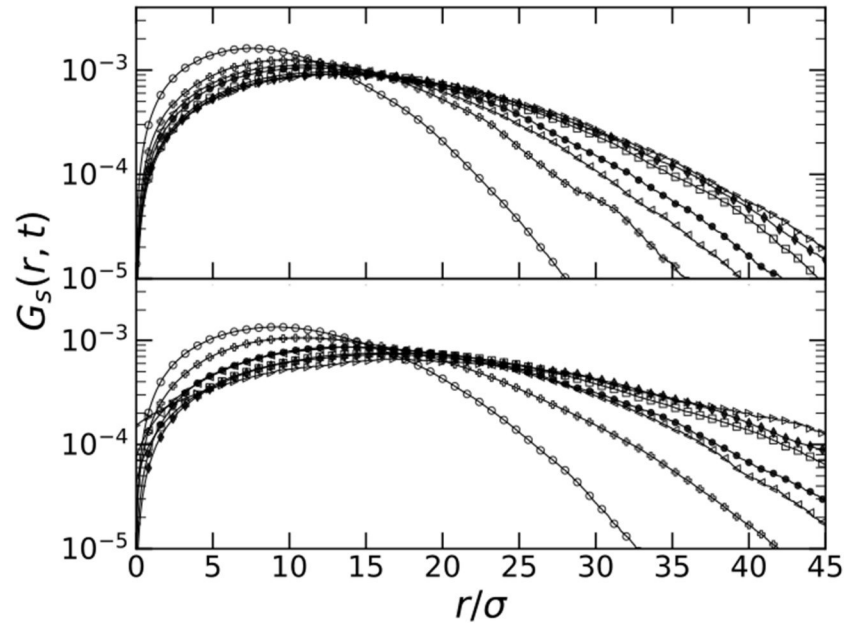


Figure 6.4.2 Self-part of the van Hove function at a time $t/\tau = 10^{-4}$ in N (bottom) and Sm (top) phases in planes perpendicular to the nematic director for scaled temperatures $T^* = 5, 8, 10, 12, 15, 17$ and 20 . Symbols as in figure 6.4.1.

In particular, the parallel s-VHF of Sm LCs, shown in the top frame of Figure 6.4.1, displays periodically peaked profiles that follow the typical layered structure of this phase. At increasing temperatures, from $T^* = 5$ to 20 , these peaks become less and less pronounced, suggesting a more uniform probability of finding particles at any distance along the nematic director. Nevertheless, at relatively low temperature, with the smectic layers well defined and less prone to density fluctuations, the profiles unambiguously suggest that particles preferentially jump from layer to layer and almost no particles are observed in between. For instance, at $T^* = 5$, while most particles are still in their original layer (primary peak), there exist especially fast particles that succeeded in diffusing, over the same period of time, to a contiguous layer (secondary peak). This is also observed at larger temperatures, but the difference between the height of primary and secondary peaks gradually softens and eventually disappears at $T^* = 20$.

The bottom frame of Figure 6.4.1 reports similar s-VHFs for the N phase. In this case, profiles with a maximum at $z = 0$ and monotonic decay at relatively long distances are observed. Most particles are therefore at or very close to their original position, with few of them fast enough to be displaced substantially larger distances over the same time window. With increasing temperature, more and more particles are able to move longer distances and correspondingly, less and less are found at their original location.

Finally, the perpendicular s-VHFs shown in Figure 6.4.2 for N (bottom frame) and Sm (top frame) phases reveal the presence of an interesting variety of particles. At $t/\tau = 10^{-4}$, most of them have left their initial position, as indicated by the peak of the distribution. These particles coexist with others that either remained very close to their original location or displaced significantly larger distances. Upon increasing temperature, the probability of observing such slow and fast particles becomes more and more uniform and would eventually become space-independent at very large temperatures, at which the system would transform into an isotropic phase.

6.5 Intermediate scattering function

Temperature also plays a key role in determining the time scale of the structural relaxation of the system. This has been estimated by computing the s-ISF in the direction parallel and perpendicular to \mathbf{n} . The s-ISFs of N and Sm phases are respectively shown in Figures 6.5.1 and 6.5.2.

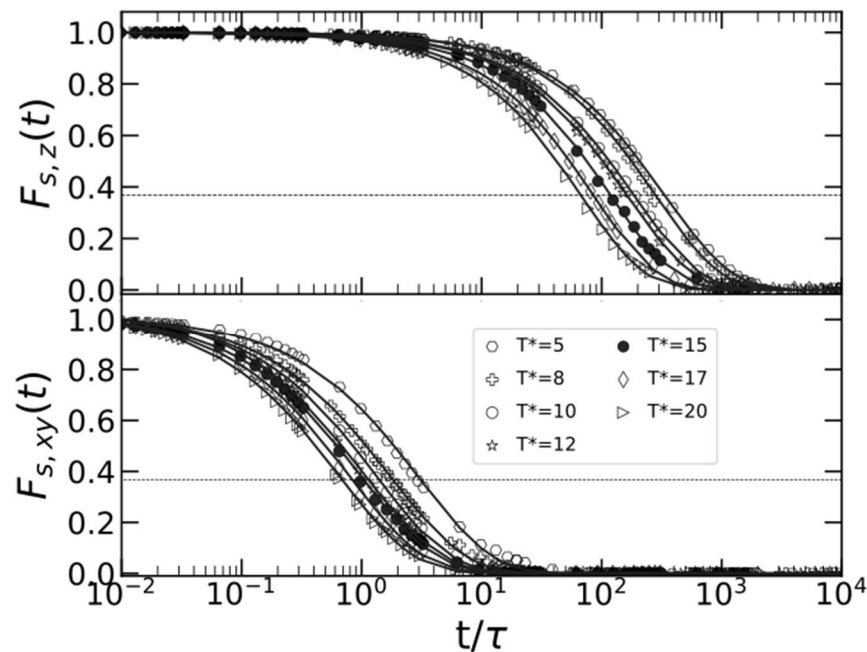


Figure 6.5.1. Temperature dependence of the self-part of the intermediate scattering function in the N phase along the nematic director (top frame) and perpendicular to it (bottom frame). Symbols indicate simulation results, while solid lines are stretched-exponential fits. All s-ISFs have been calculated at wave vectors $q_z\sigma \approx 1$ and $\sqrt{(q_x^2 + q_y^2)}\sigma \approx 6$. Dashed line corresponds to the $1/e$ value where relaxation of iSF is commonly measured.

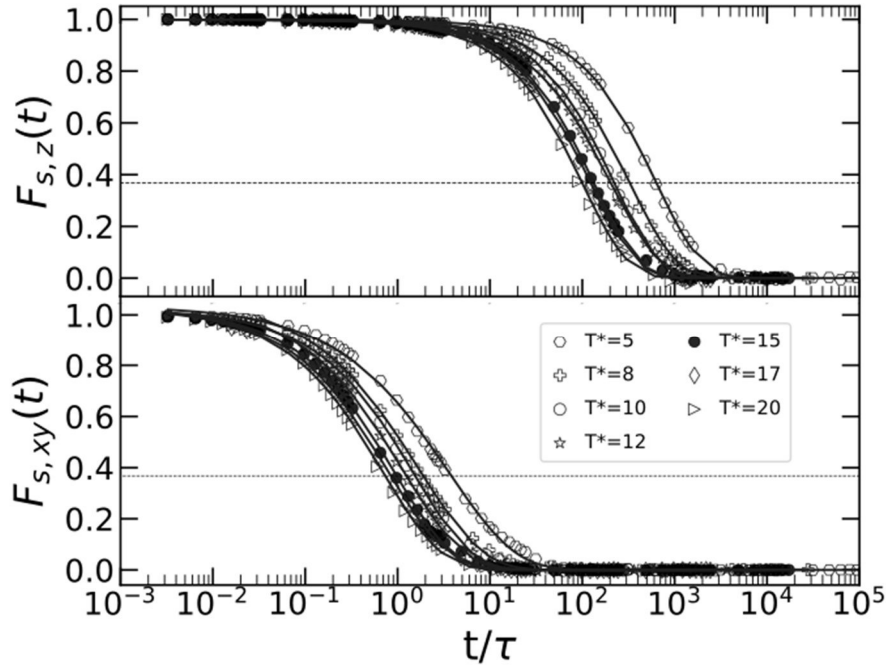


Figure 6.5.2. Temperature dependence of the self-part of the intermediate scattering function in the Sm phase along the nematic director (top frame) and perpendicular to it (bottom frame). Symbols indicate simulation results, while solid lines are stretched-exponential fits. All s-ISFs have been calculated at wave vectors $q_z\sigma \approx 1$ and $\sqrt{(q_x^2 + q_y^2)}\sigma \approx 6$. Dashed line corresponds to the $1/e$ value where relaxation of iSF is commonly measured.

In figures 6.5.1 and 6.5.2, both have been calculated at the wave vectors corresponding to the peak of the static structure factor, which are $\mathbf{q} = (0, 0, q_z)$ with $q_z\sigma \approx 1$ for the parallel s-ISFs and $\mathbf{q} = (q_x, q_y, 0)$ with $\sqrt{(q_x^2 + q_y^2)}\sigma \approx 6$ for the perpendicular s-ISFs.

Both LC phases exhibit a relevant difference between parallel and perpendicular relaxation, with the former taking up to 2 to 3 extra time decades. In all the cases studied, the decay of the s-ISFs closely follows a stretched-exponential function of the form $\exp[-(t/t_r)^\beta]$, typically observed in dense fluids [6.12], with t_r and β fitting parameters. In particular, the exponent β is approximately between 0.6 and 0.7 for $F_{s,xy}$, and between 0.8 and 0.9 for $F_{s,z}$, suggesting a more stretched decay in planes perpendicular to the nematic director than in the direction parallel to it. These values agree well with those reported in previous simulation of hard spherocylinders [6.4][6.5].

While the dependence of β on temperature is relatively mild, the relaxation time t_r , arbitrarily defined as the time at which $F_s = 1/e$, changes significantly with the temperature as can be inferred from Figure 6.5.3, where $\ln(t_r/\tau)$, is plotted as a function of $\ln(T^*)$. The so-calculated relaxation time exhibits a power-law dependence on T^* that holds in both Sm and N phases.

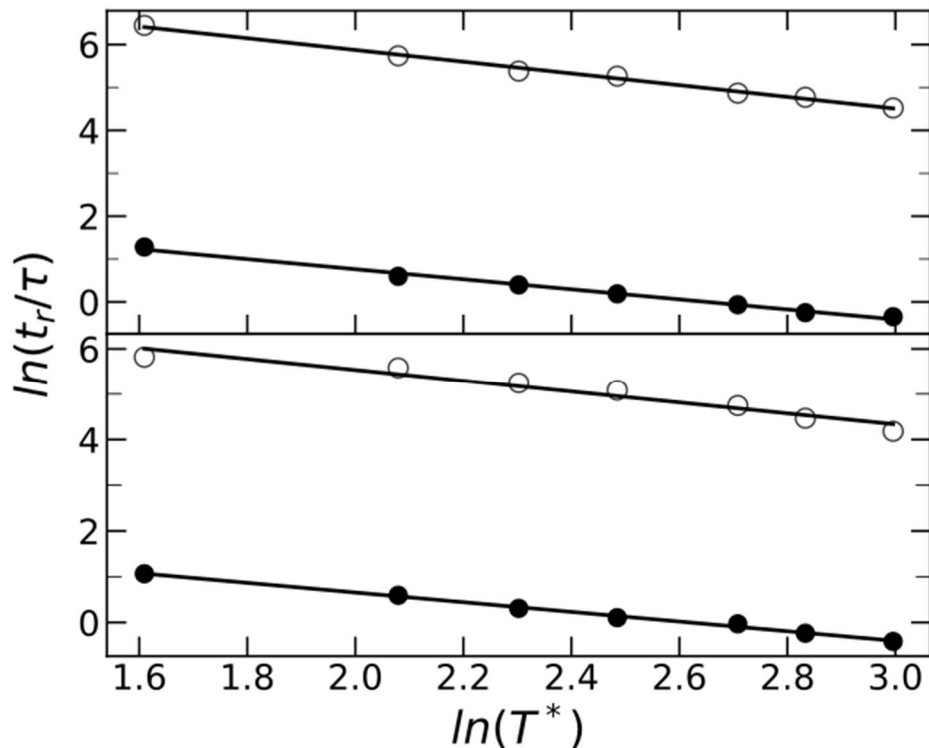


Figure 6.5.3. Relaxation times for Sm (top frame) and N (bottom frame) phases. Open and solid symbols refer respectively to structural relaxation perpendicular to the nematic director and parallel to it. Solid lines are fitted functions of the form $t_r/\tau = b \cdot T^{*a}$ where $a = -1.36$ and $b = 2980$.

6.6 Effect of modifying the Kihara potential on phase behavior

The particles simulated in this work interact via a shifted and truncated Kihara potential, as mentioned before. This potential is commonly used to model soft repulsive rod-like particles, capturing essential features of their phase behavior. In standard implementations, the repulsive interactions follow an exponent of 12-6, analogous to the Lennard-Jones potential. However, in this section, we explore the impact of modifying these exponents to 10-4 in order to examine the sensitivity of the phase diagram to the range and strength of the repulsive interactions.

The effect of modifying the interparticle interactions in liquid crystal systems has been extensively studied in the literature. It is well known that the introduction of soft repulsive interactions can significantly alter the stability of the different mesophases. For instance, in Ref [3.11] studied soft repulsive rods and demonstrated that temperature plays a crucial role in determining the stability regions of isotropic, nematic, and smectic phases, in contrast to hard-rod systems where the phase behavior is primarily controlled by density alone. This motivates the exploration of how changing the Kihara potential exponents affects the phase transitions in our system.

We performed constant-temperature Monte Carlo (MC) simulations in the NPT ensemble at $T^* = 5$, where we systematically varied the pressure of the system. As the pressure was adjusted in the input parameters, the simulation box volume fluctuated accordingly, allowing us to explore the resulting phase behavior. This approach enables the identification of phase transitions by analyzing the equilibrium density at different pressure values.

In this study, we investigate the effect of modifying the exponents of the Kihara potential from (12,6) to (10,4) to assess how changes in the range and softness of the repulsive interactions influence the phase diagram. The modified potential retains the same functional form as the one described in Section 3.4, but with different exponents. Specifically, its mathematical representation is given by:

$$U_{ij}(\mathbf{r}_{ij}, \hat{\mathbf{u}}_i, \hat{\mathbf{u}}_j) = \begin{cases} 4\epsilon \left[\left(\frac{\sigma}{d_m} \right)^{10} - \left(\frac{\sigma}{d_m} \right)^4 + \frac{1}{4} \right] & d_m \leq \sqrt[6]{2}\sigma \\ 0 & d_m > \sqrt[6]{2}\sigma, \end{cases} \quad (6.6.1)$$

where d_m represents the shortest center-to-center distance between two spherocylinders, considering their orientations.

We find that modifying the exponents from (12,6) to (10,4) leads to slight shifts in the phase diagram. The figure below presents the resulting phase diagram at $T^* = 5$ where different liquid crystal phases (isotropic, nematic, and smectic) are identified along with representative snapshots of particle configurations in each phase. The modifications to the potential result in changes in the pressure-density relationships, affecting slightly the locations of the isotropic-nematic (I-N) and nematic-smectic (N-Sm) transitions. Specifically, the nematic phase appears to be more stable across a broader range of densities compared to the standard Kihara potential, while the smectic phase remains well-defined but with slight shifts in its stability region.

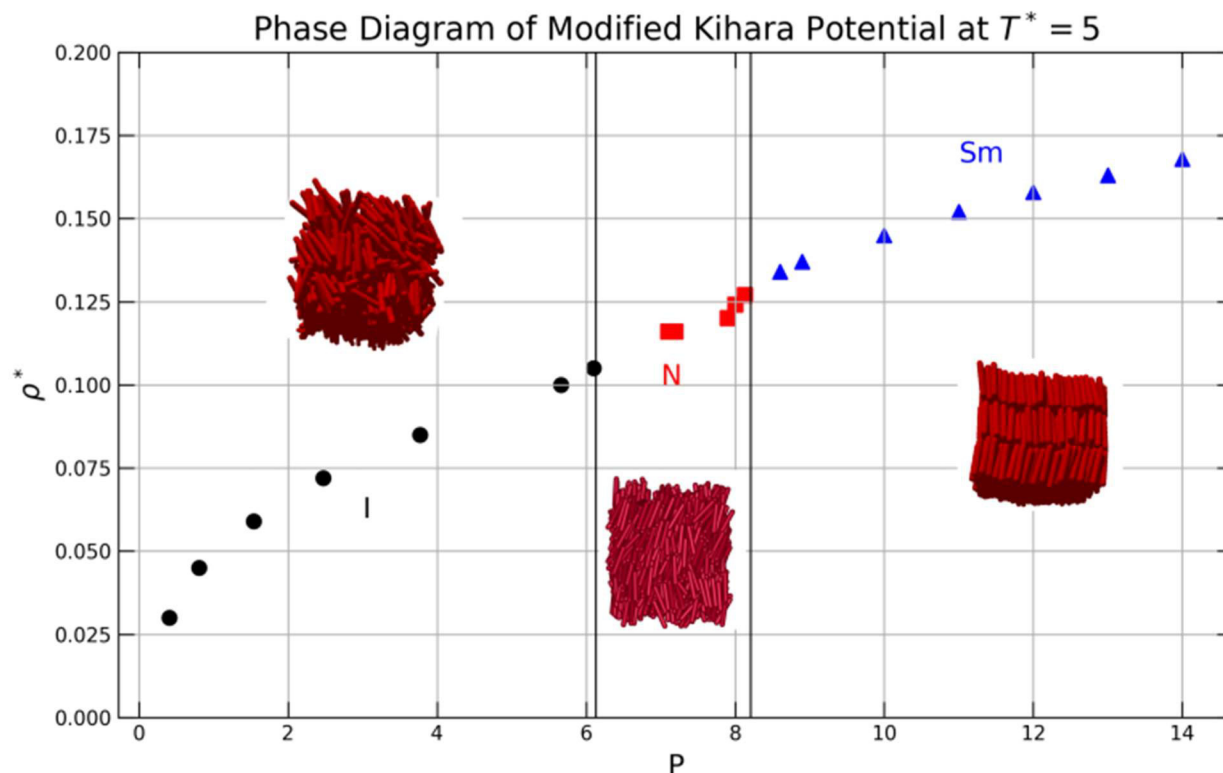


Figure 6.6.1 Phase diagram obtained from NPT Monte Carlo simulations at $T^* = 5$ for a system of spherocylinders interacting via a modified Kihara potential with exponents (10,4). The different symbols represent the identified phases: black circles correspond to the isotropic phase (I), red squares to the nematic phase (N), and blue triangles to the smectic phase (Sm). The vertical lines indicate the approximate locations of the isotropic-nematic (I-N) and nematic-smectic (N-Sm) transitions. The snapshots show representative configurations of the system at different pressures, illustrating the structural differences among the phases

These observations help as a reference for understanding how the introduction of additional interactions, such as dipolar interactions, might further modify the phase diagram. Dipole-dipole interactions are known to promote the formation of smectic and ferroelectric phases in rod-like systems, as evidenced in previous studies [5.5]. By first examining how variations in repulsive interactions alone influence phase stability, we can better anticipate the effects of long-range attractive and anisotropic interactions, which are explored in later sections of this work.

7 Results for the dipolar case

In this chapter, we present the results obtained from DMC simulations for rod-like particles with a permanent dipole moment, investigating the influence of long-range dipolar interactions on the structural and rheological properties of the system. This analysis builds upon previous studies of

non-dipolar systems, where particles interacted exclusively via the Kihara potential. By incorporating dipolar interactions using the reaction field (RF) method, we aim to determine how these long-range forces modify both the static and dynamic behavior of the system. This approach allows us to simulate the effect of the surrounding medium on the dipolar interactions within a finite simulation cell, as previously discussed in chapter 5.

Simulation Setup and Parameters Selection

MC and DMC simulations were performed on systems of N rod, each possessing a central, permanent dipole moment aligned along the main axis of the rod. To account for dipolar interactions within a finite simulation box, we employed the reaction field method, which approximates the effect of an infinite medium by surrounding each particle with a dielectric continuum. This approach ensures a more realistic treatment of long-range dipolar interactions, mitigating the limitations imposed by periodic boundary conditions.

The reaction field method requires optimizing two key parameters: the cutoff radius R_c and the dielectric constant of the surrounding medium ϵ_s . The choice of R_c is constrained by the dimensions of the simulation box, ensuring that the spherical cavity enclosing each dipole remains fully contained within the parallelepiped simulation cell. Following previous studies, we set $R_c = L_{min}/2$ where $L_{min} = \min \{L_x, L_y, L_z\}$ represents the smallest edge length of the simulation box. This choice maximizes the volume of the cavity while preserving the consistency of the RF potential within periodic boundary conditions.

For the dielectric constant ϵ_s , we employed a self-consistent iterative approach [5.5], where ϵ_s is periodically updated based on the simulated dielectric properties of the system. This method ensures a more accurate representation of the surrounding continuum, as the dielectric response of the system evolves throughout the simulation. Specifically, we initialized the simulation with an estimated value of ϵ_s and recalculated it every 10^3 Monte Carlo cycles using the Clausius-Mossotti fluctuation formula (5.2.33).

This iterative process converges to a stable ϵ_s , ensuring that the reaction field method accurately captures the dielectric screening effects.

Each simulation was equilibrated over 10^6 Monte Carlo cycles. One Monte Carlo cycle consisted of N trial moves, including translational and rotational displacements of the rods.

The strength of the dipole is represented by the dipole moment value $\mu = 1$. The dipole moment is given in reduced units, expressed as $\mu = \frac{\mu_{real}}{\sqrt{\epsilon_0 kT \sigma^3}}$, where ϵ_0 is the permittivity of free space, k is the Boltzmann constant, T the temperature of the system and σ the particle diameter.

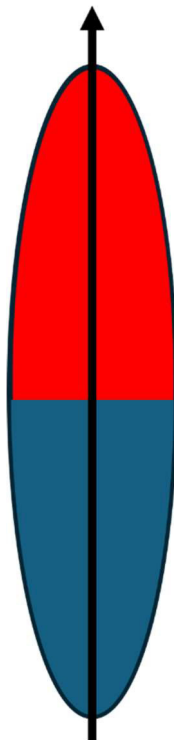


Figure. 7.1 Representation of a dipolar particle with a central permanent dipole moment. The dipole is aligned with the major axis of the rod, as indicated by the arrow.

Previous studies have shown that dipolar interactions become more significant at lower temperatures [5.5], especially in liquid crystal systems. By comparing the results from both temperatures, we aim to better understand how dipole-dipole interactions affect the mechanical and dynamic properties of the system

To evaluate the impact of dipolar interactions, we analyzed key structural and rheological properties in both dipolar and non-dipolar systems, including order parameter, MSD, self-diffusion coefficients and viscoelastic moduli.

By introducing dipolar interactions, we observe a significant modification of the system's response. Notably, the presence of dipole moments leads to increased structural ordering, as evidenced by higher values of S_2 . Similarly, the mean squared displacement and self-diffusion coefficients exhibit anisotropic behavior, reflecting the directional influence of dipolar interactions.

By employing the DMC method in combination with the reaction field approach, and applying the passive microrheology technique, it is possible to detect changes in the viscoelastic properties of liquid crystals upon the introduction of dipolar interactions. The tracer particle effectively captures these variations, confirming that the method is sensitive to the influence of long-range interactions. The observed effects are discussed in detail in the following subsections.

Microrheology

In order to probe the viscoelastic properties of the systems, we introduced a spherical tracer particle with a diameter $\sigma_s = 1$, in the liquid crystals. The tracer behaves as a hard sphere, allowing us to track its motion over time. By measuring its displacement, we can determine the system's viscoelastic modulus.

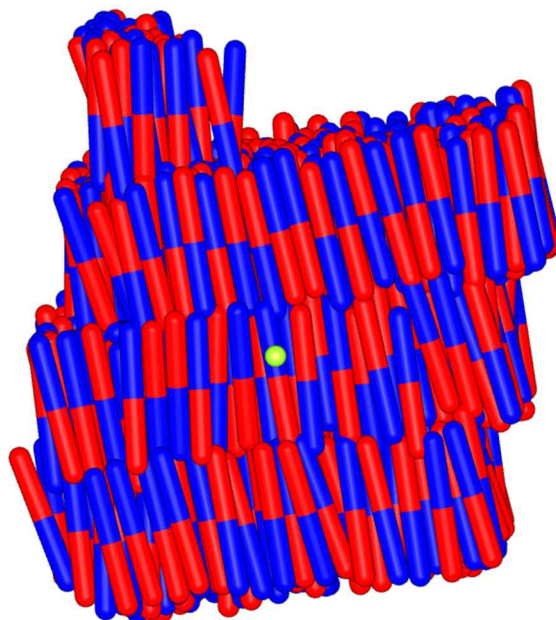


Figure 7.2 Snapshot of a spherical tracer particle embedded in a bath of spherocylinders in the smectic phase. Dipole positive and negative signs are indicated by colors red and blue, respectively.

As depicted in Figure 7.2, the tracer moves through the liquid crystal, and its displacements are analyzed in the parallel and perpendicular directions relative to the nematic director. These displacements are essential for calculating the viscoelastic response, allowing us to extract both the elastic modulus $G'(\omega)$ and the viscous modulus $G''(\omega)$, as previously mentioned in chapter 4.

We performed DMC simulations to investigate the microrheological behavior of both nematic and smectic phases. These simulations were carried out at different temperatures, $T^* = 1, 1.46$, and 10, in order to explore how dipolar interactions influence the viscoelastic properties at varying thermal conditions.

7.1 Effect of Dipolar Interactions at High Temperatures

We begin by presenting simulations of the Sm phase at a higher temperature: $T^* = 10$. At this temperature, the influence of dipolar interactions is relatively weak, as thermal motion dominates and disrupts the ordering effect that dipoles can have. This supports our observation that at high temperatures, the impact of dipole interactions on the system's overall behavior is minimal, as also reported in previous studies on dipolar fluids under comparable conditions [7.1].

In contrast, as temperature decreases, the effects of dipolar interactions become more pronounced, leading to stronger alignment and order within the system. This will be further discussed in the following sections. The snapshots below illustrate the behavior at $T^* = 10$, showing the limited role of dipoles at this temperature.

In the following snapshots, we present the configurations for both dipolar and non-dipolar systems at $T^* = 10$.

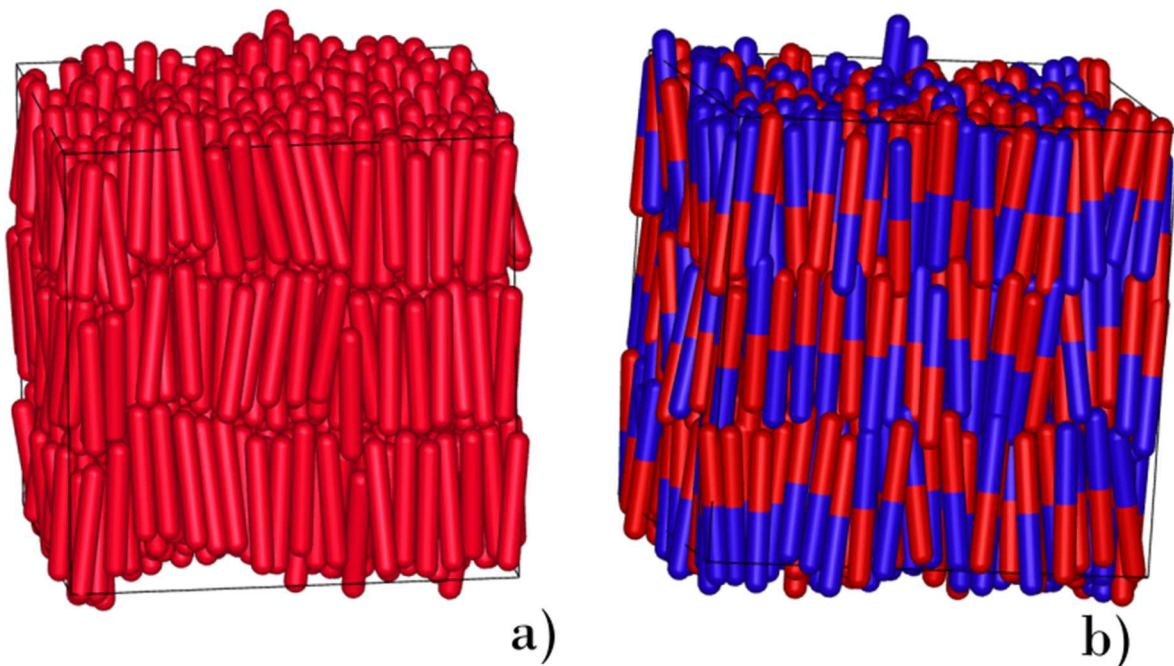


Figure 7.1.1. Snapshot of Sm phase for non-dipolar a) and dipolar b) systems at $T^* = 10$.

As expected, there are no significant differences between the two systems. To further investigate whether the presence of dipoles induces structural changes, we calculated the distribution function parallel to the nematic director. The graph of $g(z)$, shown below, reveals that there are no notable changes in the characteristic peaks of the smectic phase. Both dipolar and non-dipolar systems exhibit virtually identical $g(z)$ profiles, indicating no discernible structural differences.

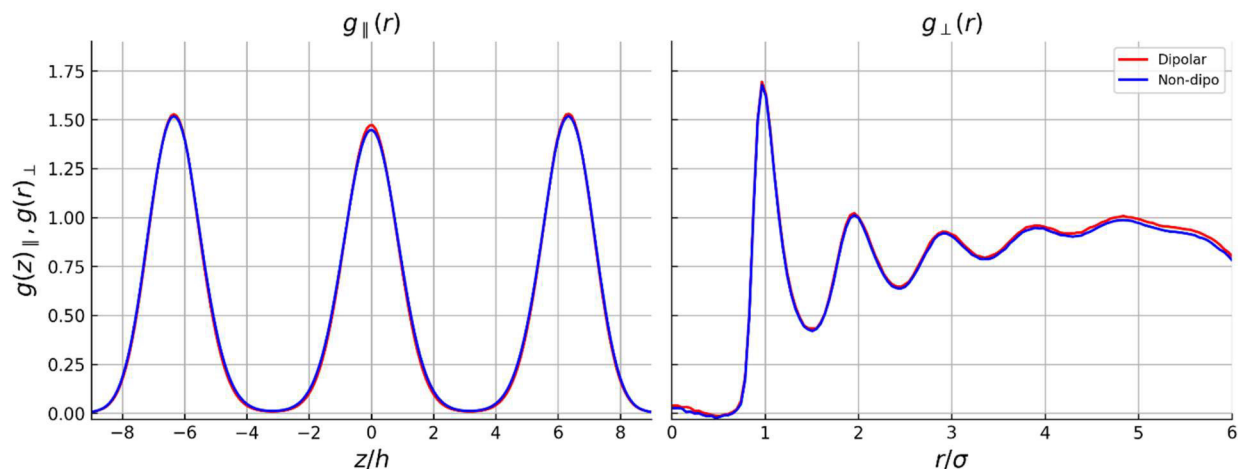


Figure 7.1.2. Parallel distribution function of Sm phase for non-dipolar and dipolar systems. Left frame corresponds to the distribution function in parallel direction to \mathbf{n} , while the right frame corresponds to the perpendicular direction.

Figure 7.1.2 shows that the structure in the parallel and perpendicular directions remains practically unchanged for both systems, indicating that the dipoles do not significantly affect the structural order at higher temperatures.

This clearly conveys that the dipoles have little impact on the system's structure at high temperatures.

We also computed the order parameters for both systems, which were also nearly identical, reinforcing the observation that dipolar interactions have minimal impact on the ordering of the rods at this temperature, as shown in the following figure.

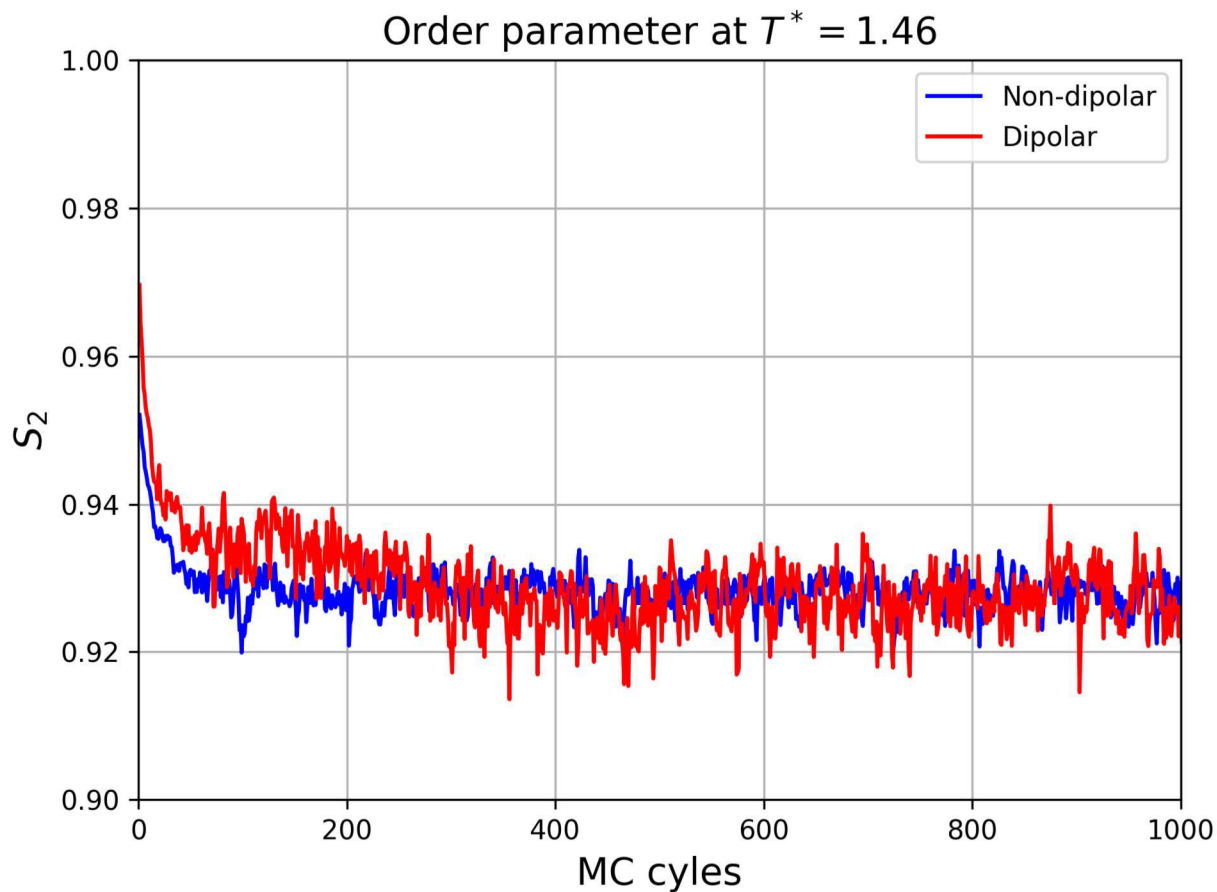


Figure 7.1.3. Order parameter for dipolar (blue) and non-dipolar (red) Sm phase at $T^* = 10$, obtained from the MC simulations.

Finally, we analyzed the mean square displacement of the tracer particle. Given the absence of significant changes in the system's structure and order, it is unsurprising that no substantial differences were observed in the MSD between the dipolar and non-dipolar systems. This is clearly illustrated in the following figure.

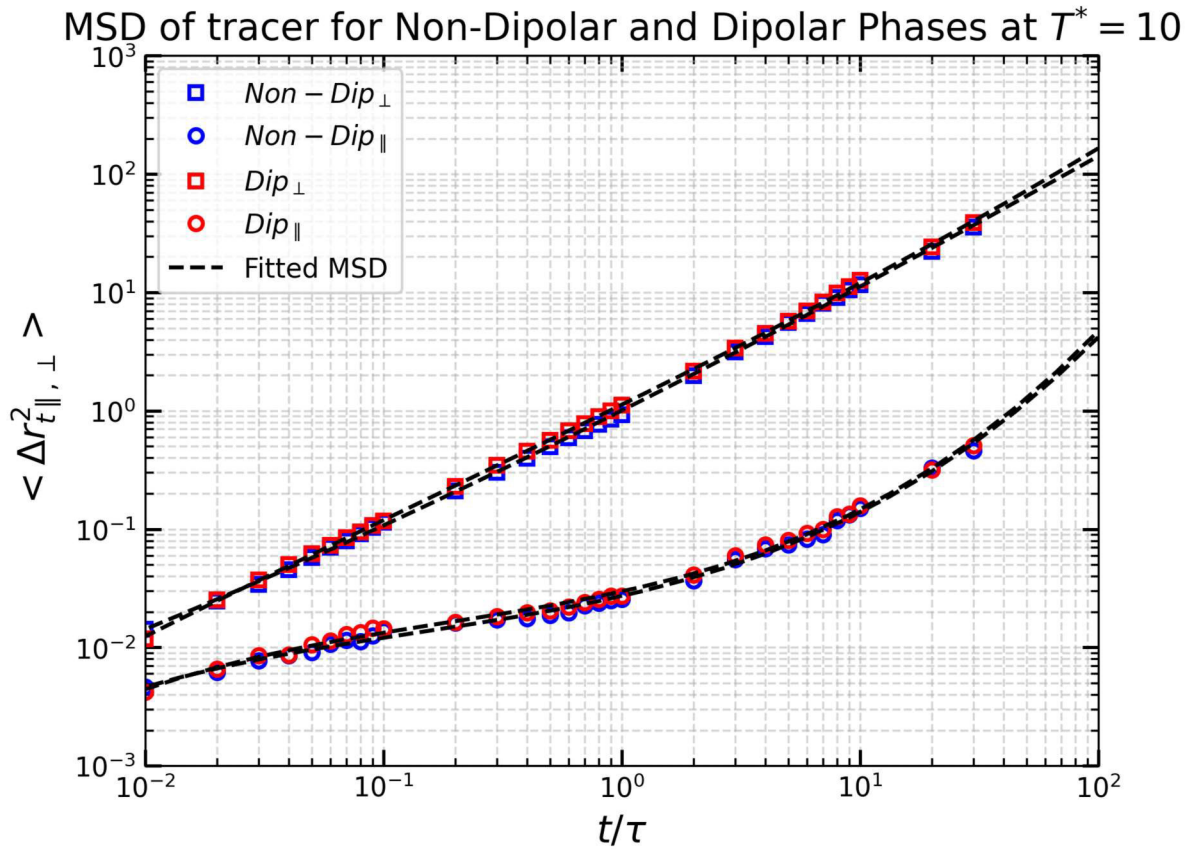


Figure 7.1.4. MSD of tracer in parallel and perpendicular directions for dipolar and non-dipolar Sm phase at temperature $T^* = 10$.

As shown in Figure 7.1.4, the MSDs for both dipolar and non-dipolar systems at $T^* = 10$ are nearly identical in both parallel and perpendicular directions, indicating that dipolar interactions do not significantly affect tracer dynamics at this high temperature. This result is consistent with previous reports suggesting that thermal energy dominates over dipolar interactions at high temperatures, leading to behavior that resembles that of non-polar systems [7.1]. Although the outcome might seem expected, confirming it through simulation supports the validity of the model and provides a reference point for comparison with lower-temperature cases. The following section explores tracer behavior at lower temperatures, where dipolar interactions play a more prominent role in restricting mobility and enhancing structural order.

7.2 Transition from Nematic to Smectic Phase

To investigate how dipolar interactions influence phase behavior and viscoelastic properties in anisotropic fluids, we performed Dynamic Monte Carlo (DMC) simulations on a system of

spherocylindrical particles, with and without embedded dipoles, at reduced temperature $T^* = 1$. The particles interact via the Kihara potential, and long-range dipolar interactions were incorporated using the Reaction Field method. At this temperature and density $\rho^* = 0.12$ the system without dipoles stabilizes in a nematic phase. When dipolar interactions are introduced, the system undergoes a transition to a more ordered smectic phase, as shown in Figure 7.2.1.

Figure 7.2.1 shows representative snapshots of the systems. The non-dipolar system exhibits a nematic phase with well-aligned rods, while the dipolar system transitions into a layered smectic phase. The inclusion of dipoles, modeled via the Reaction Field method, promotes enhanced orientational and positional ordering, consistent with a smectic structure.

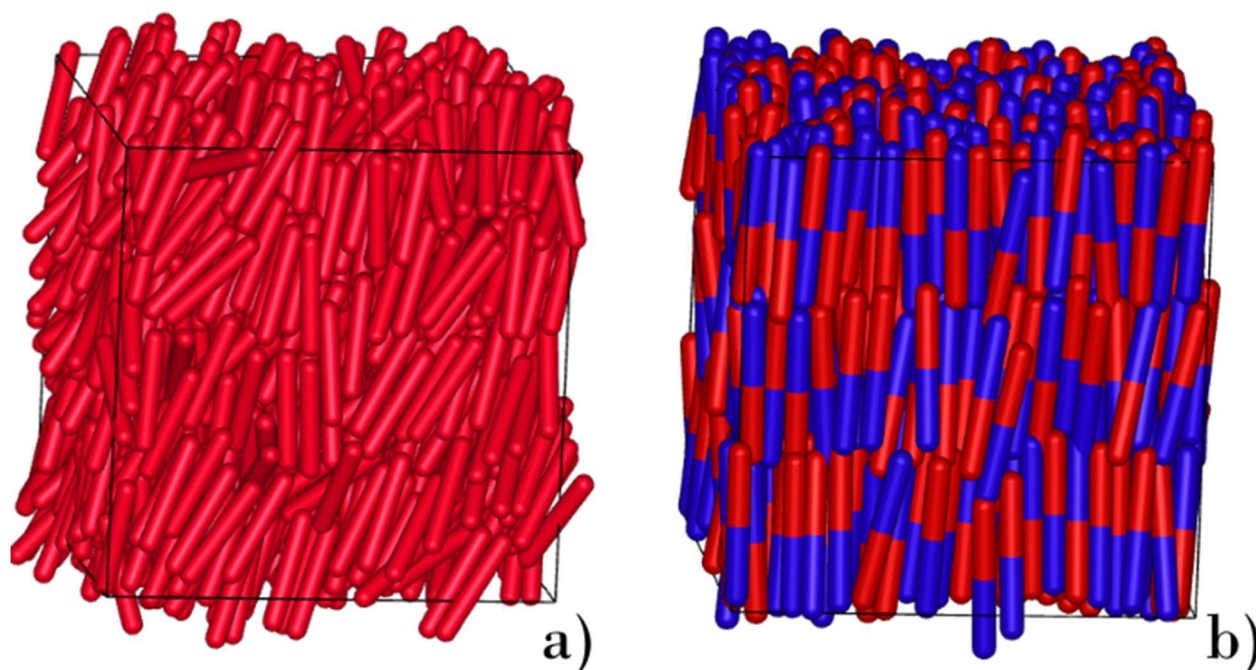


Figure 7.2.1 Snapshots of the system before and after dipolar interactions were introduced. (a) Non-dipolar system in the nematic phase. (b) Dipolar system showing transition into a smectic phase.

In Figure 7.2.1, two systems can be observed. Panel (a) shows the non-dipolar system in the nematic phase, characterized by orientational ordering without translational layering. In contrast, panel (b) illustrates the dipolar system, where clear layered structures emerge, indicative of a smectic phase. These results clearly show that dipolar interactions promote the stabilization of a smectic phase, even under conditions where the system would otherwise remain nematic. Similar behavior, where dipolar interactions favor the formation of smectic ordering, has been reported in previous studies of dipolar liquid crystal phases [7.1]. Additionally, the rods appear to alternate

their orientation along the director, suggesting the possibility of local antiferroelectric ordering. To quantitatively corroborate this visual observation, we calculated the Legendre correlation functions, as discussed below.

To analyze potential ferroelectric or antiferroelectric behavior, we calculated the Legendre correlation functions $S_1(r)$ and $S_3(r)$, which correspond to the first and third Legendre polynomials, respectively. Specifically, $S_1(r)$ detects ferroelectric order (aligned dipoles), while $S_3(r)$ is sensitive to antiferroelectric alignment (alternating dipoles). As shown in Figure 7.2.2, both functions tend to zero for the dipolar systems across all distances, indicating the absence of long-range ferroelectric or antiferroelectric phases, despite the visual alternation in dipole orientation observed in the snapshots. This finding is consistent with prior studies on dipolar rod-like systems, where no macroscopic ferroelectric order was detected under comparable conditions [7.3], [7.4].

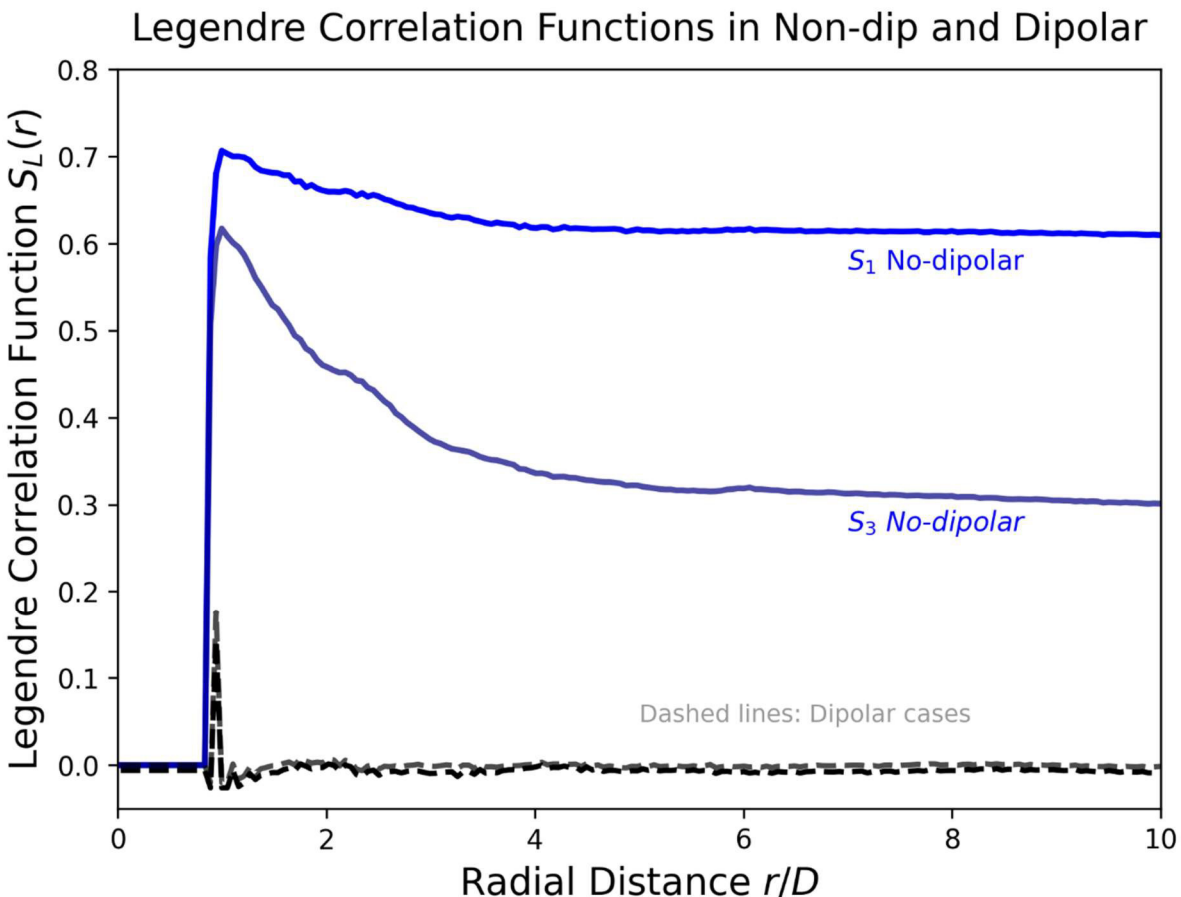


Figure. 7.2.2 Legendre correlation functions $S_1(r)$ and $S_3(r)$ for dipolar and non-dipolar systems. The functions were calculated to assess the presence of ferroelectric or antiferroelectric

order. Both $S_1(r)$ and $S_3(r)$ approach zero for the dipolar system, indicating the absence of long-range ferroelectric alignment.

The structural transition from Nm to Sm is further supported by the analysis of the nematic order parameter S_2 shown in Figure 7.2.3. The evolution of S_2 over Monte Carlo cycles reveals that the non-dipolar system stabilizes around 0.77, which is consistent with typical values for nematic phases. In contrast, the dipolar system reaches an S_2 value of approximately 0.89, indicating significantly enhanced orientational alignment driven by dipolar interactions.

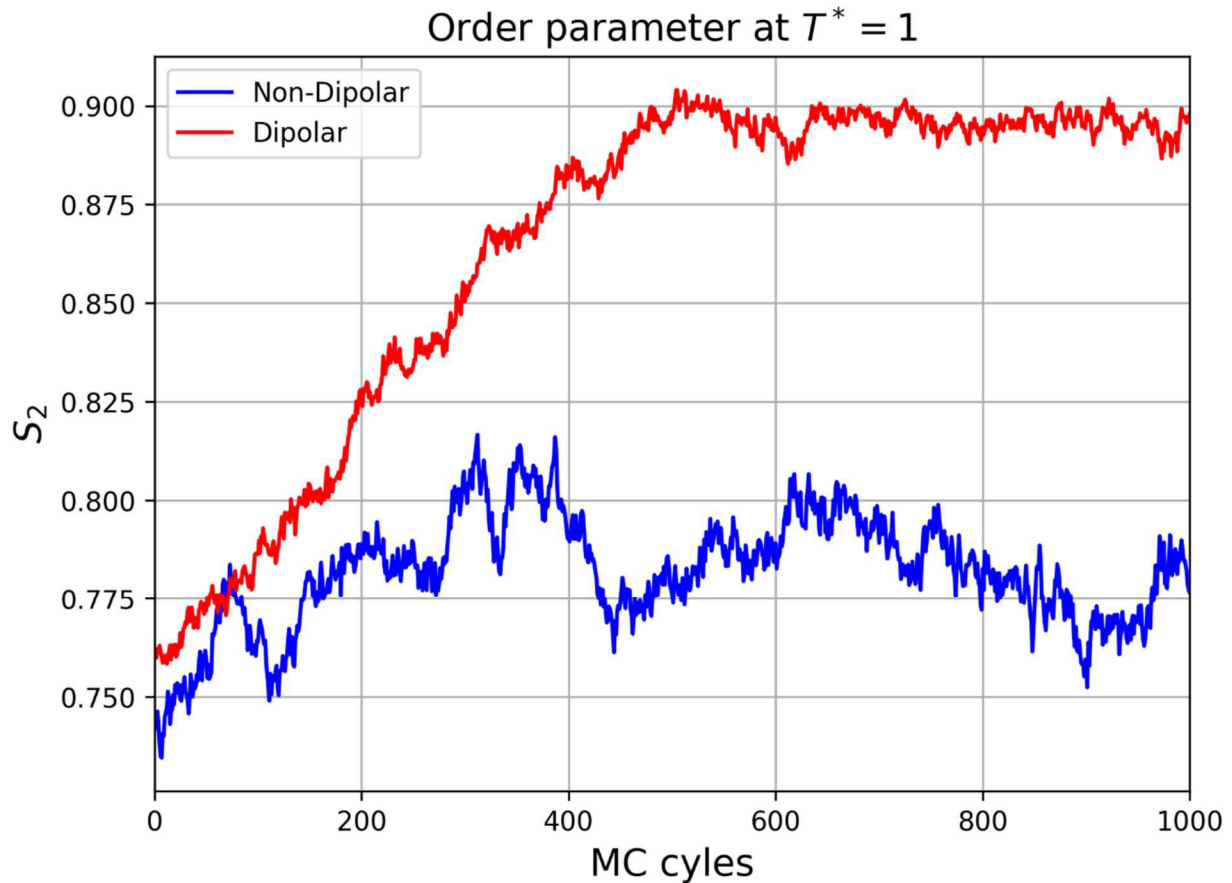


Figure 7.2.3 Evolution of the nematic order parameter S_2 over Monte Carlo cycles for dipolar and non-dipolar systems at $T^* = 1$

The observed increase in S_2 for the dipolar system is consistent with previous reports demonstrating that dipolar interactions can reinforce orientational ordering, particularly when dipoles are aligned along the rod's longitudinal axis [7.4]. Although dipolar interactions alone do not necessarily induce macroscopic polar phases, they can influence the degree of alignment, especially in systems where steric and dipolar effects act together. This enhanced orientational ordering contributes to the stabilization of smectic-like structures, as observed in the snapshots and corroborated by the higher S_2 value. The extent of this effect depends on factors such as dipole strength and dipole location on the rod, as discussed by Weis et al. [7.4].

To further quantify the structural transition, we computed pair correlation functions in the parallel and perpendicular directions, as well as the total correlation function, as shown in Figure 7.2.4. The dipolar system exhibits pronounced peaks in $g(z)_{\parallel}$ characteristic of smectic layering, whereas the non-dipolar system shows flatter profiles typical of a nematic phase. In the perpendicular direction, both systems display similar correlations, while the total distribution function $g(r)_{\perp}$ reveals enhanced short-range ordering in the dipolar case.

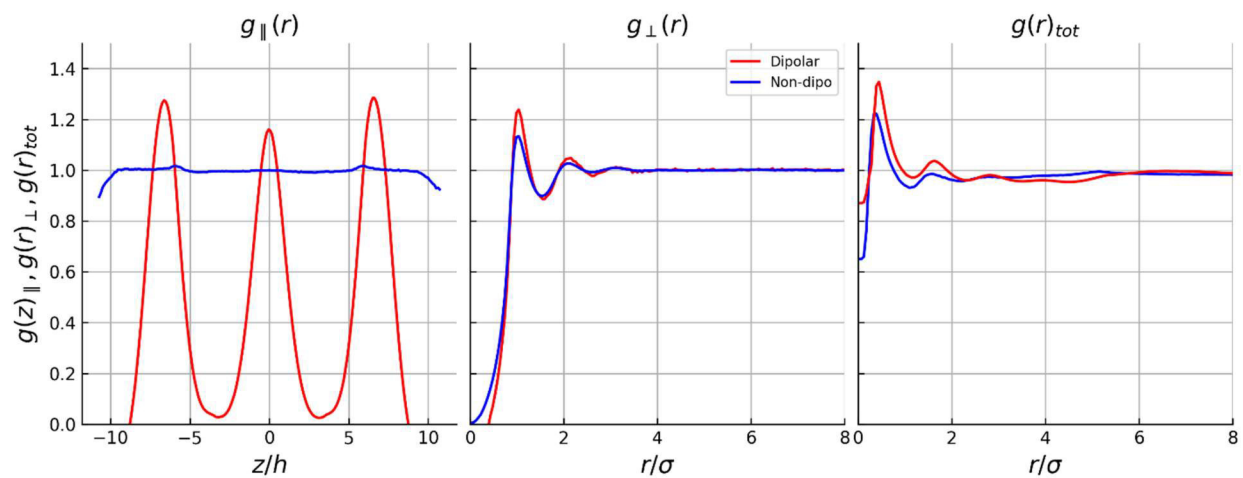


Figure. 7.2.4 Distribution functions $g(z)_{\parallel}$, $g(r)_{\perp}$ and $g(r)_{tot}$ for dipolar and non-dipolar systems at $T^* = 1$. Dipolar interactions promote stronger parallel correlations indicative of smectic layering.

As structural analyses revealed significant differences between dipolar and non-dipolar systems, particularly the formation of smectic layers in the presence of dipolar interactions, we next investigated whether these structural changes influence rod mobility. To this end, we computed the mean squared displacement of the rods in both parallel $\langle \Delta r^2 \rangle_{\parallel}$ and perpendicular $\langle \Delta r^2 \rangle_{\perp}$ directions relative to the nematic director at $T^* = 1$. Figure 7.2.5 shows the MSD curves for dipolar and non-dipolar systems in both directions.

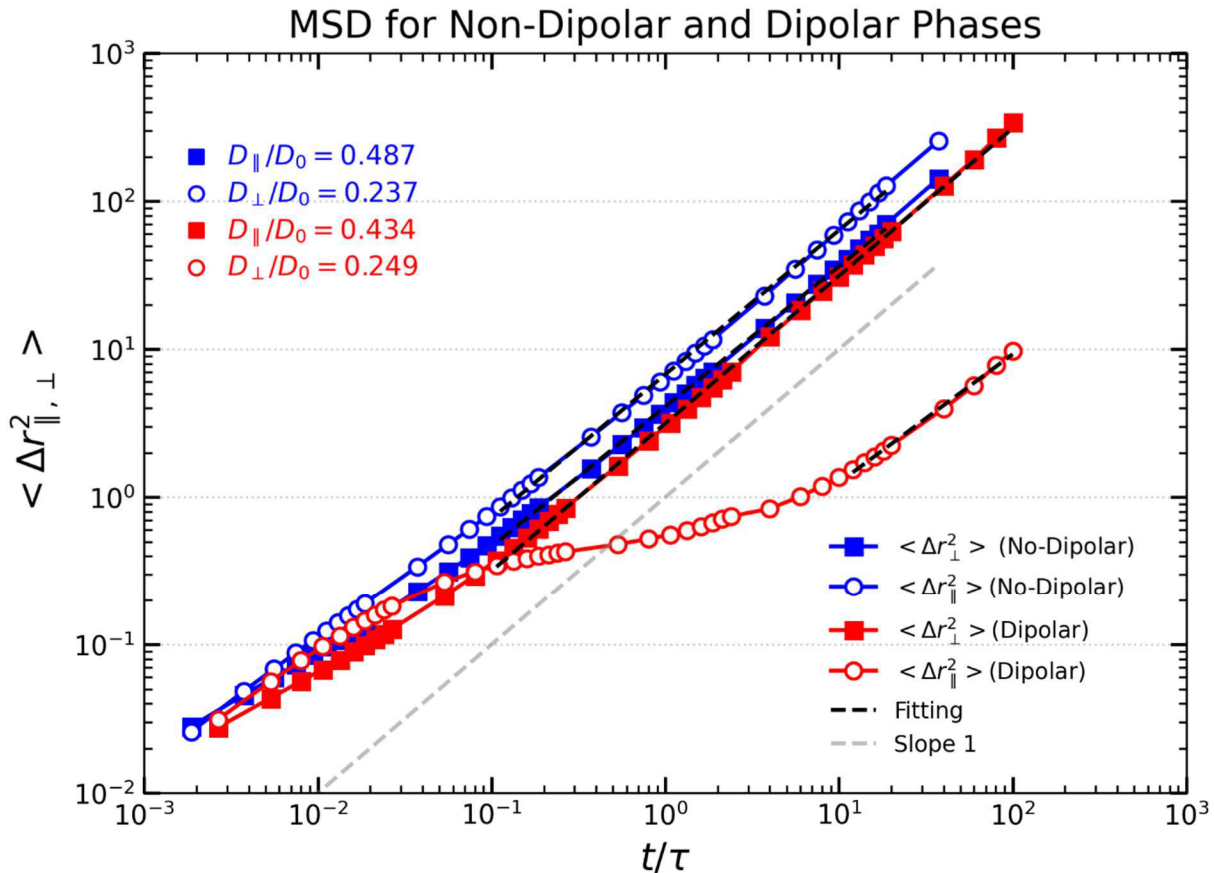


Figure 7.2.5 Mean squared displacements of rods in the \parallel and \perp directions for dipolar and non-dipolar systems at $T^* = 1$. Blue symbols correspond to the non-dipolar system while red symbols correspond to the dipolar one. Circles and squares refer to parallel and perpendicular directions, respectively. The dipolar system shows a marked reduction in parallel displacement due to smectic layering, while perpendicular displacement is slightly higher for the non-dipolar system.

In the non-dipolar system, the MSD values for both $\langle \Delta r^2 \rangle_{\parallel}$ and $\langle \Delta r^2 \rangle_{\perp}$, are relatively high in comparison to the dipolar one, indicative of free rod mobility characteristic of a nematic phase. However, in the dipolar system, the MSD in the parallel direction decreases significantly. This reduction is attributed to the formation of smectic layers, which hinders translational motion along the director, as rods must overcome the energy barrier associated with moving across layers. In contrast, the MSD in the perpendicular direction remains comparable between dipolar and non-dipolar systems, suggesting that lateral rod mobility is less affected by smectic ordering.

These observations confirm that dipolar interactions induce anisotropic constraints on rod mobility, particularly suppressing displacement along the director due to the emergence of layered structures. This effect has been reported in previous studies where smectic-like ordering imposed significant barriers to translational motion along the director while preserving x-y mobility [7.3], [7.4].

Building upon the observed differences in rod mobility, we next investigated how dipolar interactions affect the local viscoelastic response of the system. To this end, we performed microrheological analysis using tracer particles embedded in the system. Microrheology has proven particularly valuable in exploring mechanical responses at the microscale, such as in biological systems [7.2]. The mean squared displacement of these tracers was calculated in both parallel $\langle \Delta r^2 \rangle_{t_{\parallel}}$ and $\langle \Delta r^2 \rangle_{t_{\perp}}$ directions for dipolar and non-dipolar systems at $T^* = 1$, as shown in Figure 7.2.6.

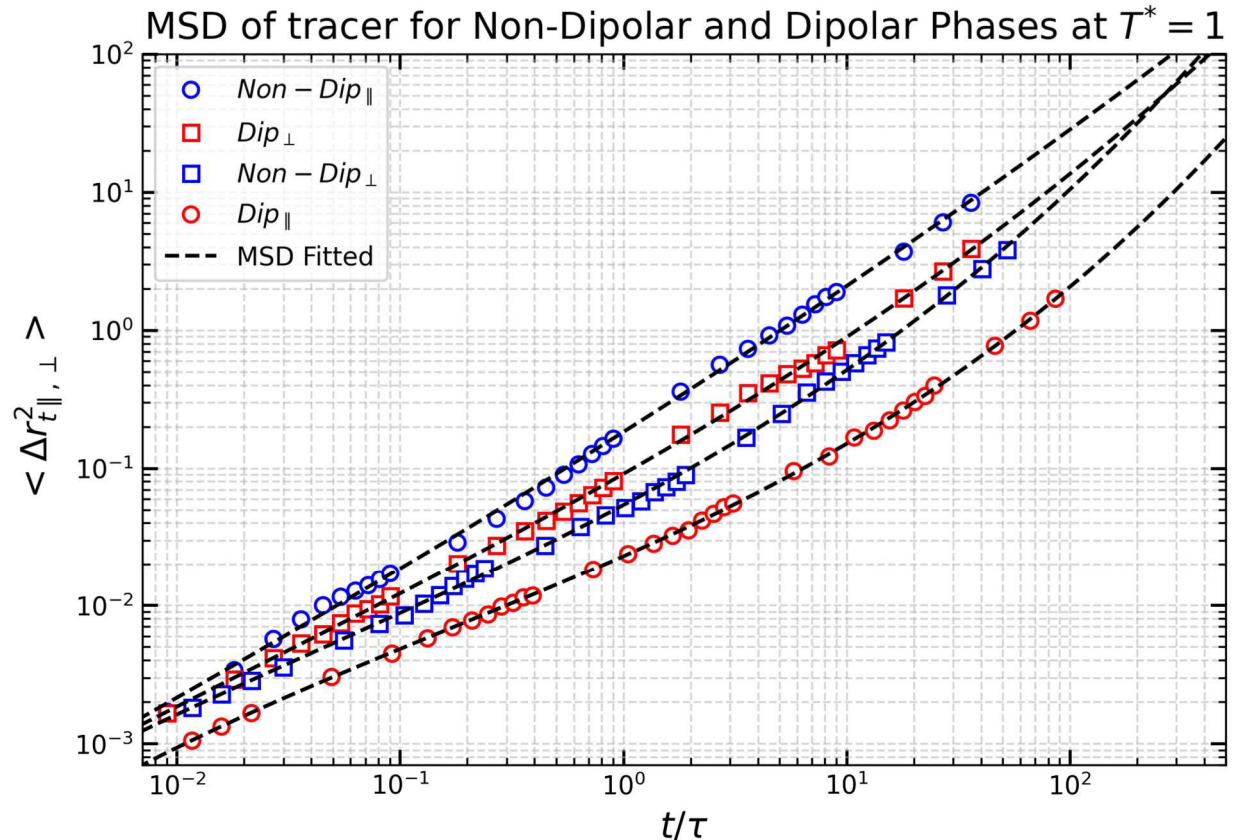


Figure 7.2.6 MSD of tracer particles in parallel and perpendicular directions for dipolar and non-dipolar systems at reduced temperature $T^* = 1$. The blue symbols correspond to the non-dipolar system, while red symbols represent the dipolar one. Circles and squares refer to parallel and perpendicular directions, respectively. The dashed line indicates a polynomial fitting.

As can be seen from Figure 7.2.6, in the non-dipolar system, tracer particles exhibit higher MSD values in both directions, reflecting the fluid-like nature of the nematic phase. When dipolar interactions are present, and the system transitions to a smectic phase, the tracer MSD decreases, especially in the parallel direction. This reduction indicates restricted mobility along the director, consistent with the presence of smectic layers that confine the tracer and hinder its movement

between layers. In contrast, the difference in MSD between dipolar and non-dipolar systems in the perpendicular direction is smaller, suggesting that lateral diffusion is less impacted by layering.

To quantitatively assess the viscoelastic response of the system, we computed the storage and loss moduli using the Mason method [4.7]. As described in chapter 6, this method is based on the generalized Stokes-Einstein relation, where the frequency-domain moduli are calculated directly from the tracer MSD using the Gamma function, avoiding explicit Fourier transforms.

Figure 7.2.7 presents the computed $G'(\omega)$ and $G''(\omega)$ in parallel and perpendicular directions for dipolar and non-dipolar systems at $T^* = 1$.

In the parallel direction, the dipolar system exhibits significantly higher values of $G'(\omega)$ and $G''(\omega)$ across all frequencies compared to the non-dipolar system. This is attributed to the smectic layering induced by dipolar interactions, which increases the rigidity and viscous resistance along the director. The formation of layers hinders tracer motion and enhances the elastic and viscous response.

Conversely, in the perpendicular direction, the non-dipolar system shows higher values of both, $G'(\omega)$ and $G''(\omega)$, than the dipolar system. This can be explained by the differences in phase structure: in the nematic non-dipolar system, the disordered arrangement leads to more frequent collisions and steric hindrance as the tracer moves laterally, thereby increasing the viscoelastic response. In contrast, the dipolar smectic phase presents well-organized layers that may offer less resistance to lateral tracer motion, facilitating smoother diffusion across layers.

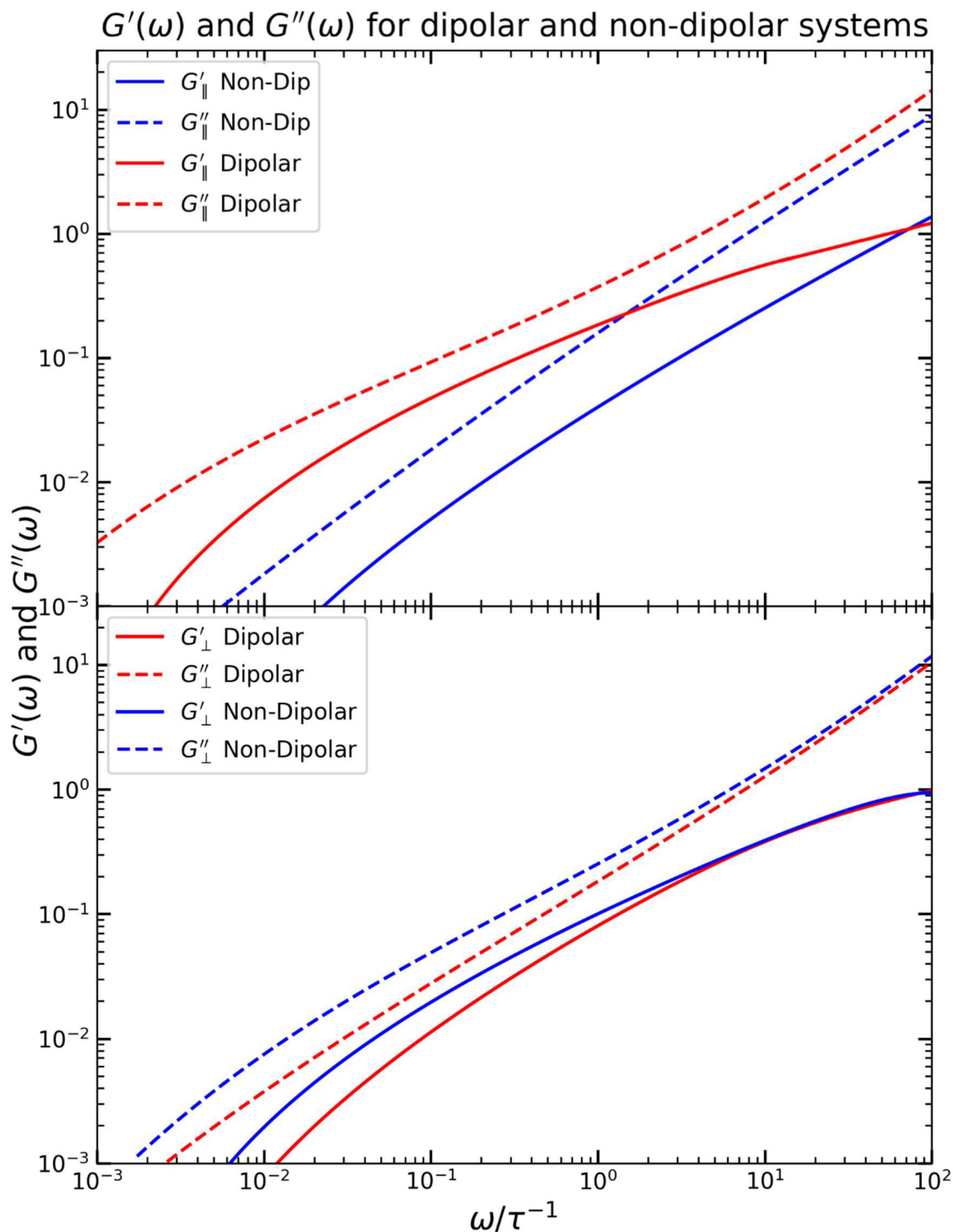


Figure 7.2.7 $G'(\omega)$ and $G''(\omega)$ calculated from tracer MSD using the Mason method for dipolar (red) and non-dipolar (blue) systems at $T^* = 1$. In the parallel direction, the dipolar system exhibits higher viscoelastic moduli due to smectic layering. In the perpendicular direction, the non-dipolar system shows higher moduli, reflecting increased hindrance to lateral tracer motion in the nematic phase.

The directional contrast in viscoelastic moduli underscores the anisotropic mechanical response induced by dipolar interactions and confirms the formation of a more rigid structure along the director and a more compliant response perpendicular to it in the dipolar system.

To facilitate a direct comparison of the viscoelastic moduli across different systems and directions, we present all calculated values of $G'(\omega)$ and $G''(\omega)$ for dipolar and non-dipolar systems, in both \parallel and \perp directions, on a single graph (Figure 7.2.8). This allows us to assess how the phase transition from nematic to smectic, induced by dipolar interactions, affects the frequency-dependent mechanical response.

In all cases, the loss modulus $G''(\omega)$ is consistently larger than the storage modulus $G'(\omega)$ across the frequency range studied. This behavior is characteristic of liquid crystal phases, which generally exhibit viscous-dominated responses at these scales, particularly in rod-like systems.

The highest moduli values are observed for the dipolar system in the parallel direction, i.e., along the director of the smectic phase. Both $G'(\omega)_{\parallel}$ and $G''(\omega)_{\parallel}$ for the dipolar case show a pronounced increase, especially at higher frequencies. This is attributed to the formation of smectic layers, which restrict tracer motion along the director, thereby enhancing the elastic resistance and energy dissipation, reflected in the higher moduli.

In contrast, the moduli for the perpendicular direction $G'(\omega)_{\perp}$ and $G''(\omega)_{\perp}$ are comparable between dipolar and non-dipolar systems. However, the non-dipolar system displays slightly higher values, especially in $G''(\omega)$, indicating that x-y (perpendicular) motion in the nematic phase is more constrained. This can be explained by the lack of defined in-plane ordering in the nematic phase, which introduces fluctuations and local obstacles to lateral diffusion, increasing the viscous resistance. Conversely, in the smectic phase, well-defined x-y plane ordering can facilitate smoother tracer displacement across the layers, slightly reducing $G''(\omega)_{\perp}$.

Finally, the lowest moduli across all cases are observed for the non-dipolar system in the parallel direction, i.e., $G'(\omega)_{\parallel}$ and $G''(\omega)_{\parallel}$ for the nematic phase. This is expected, as the absence of positional order in the nematic phase allows for relatively unrestricted tracer motion along the director, resulting in lower viscoelastic resistance.

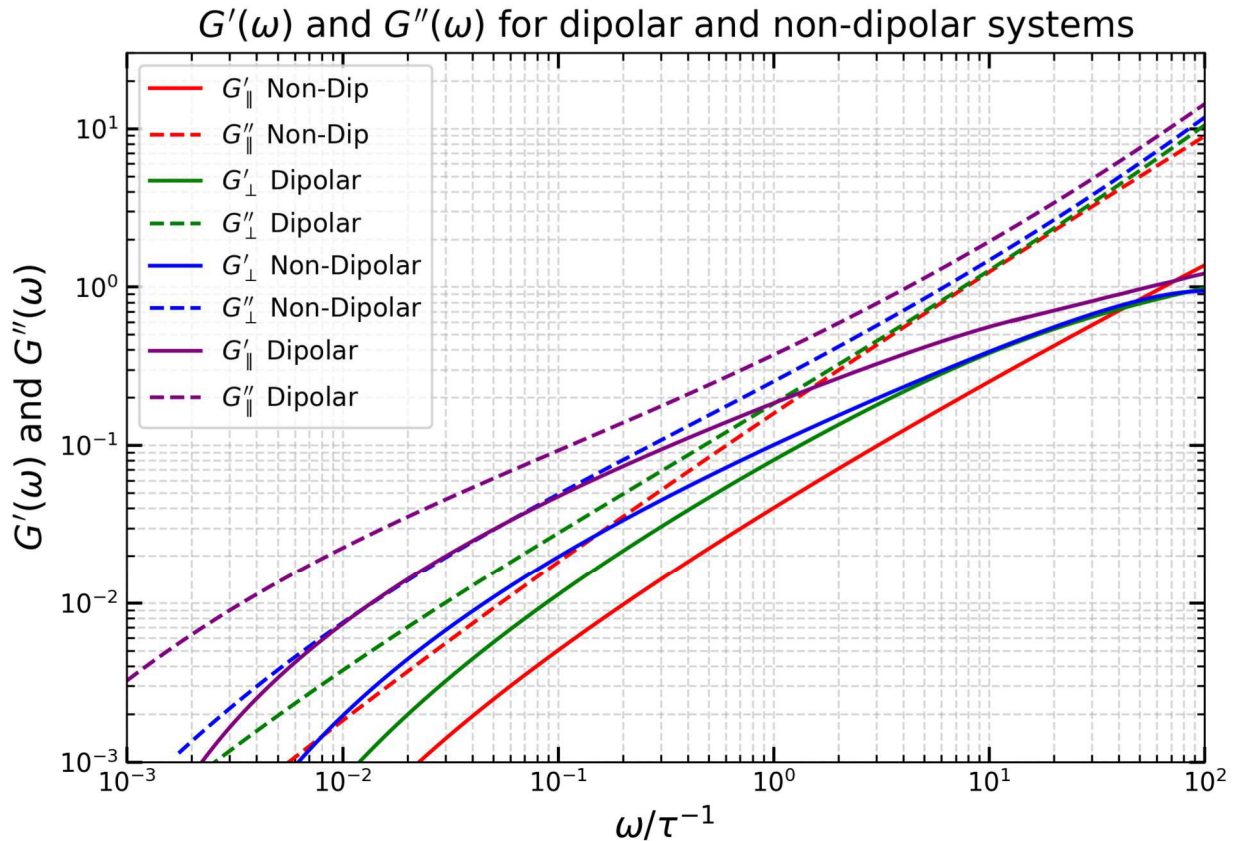


Figure 7.2.8. Viscoelastic moduli $G'(\omega)$ and $G''(\omega)$ calculated from tracer MSDs for dipolar and non-dipolar systems at $T^* = 1$, in parallel and perpendicular directions. All moduli show $G''(\omega) > G'(\omega)$, typical of liquid crystals. The highest values correspond to the parallel direction in the dipolar system, while the lowest are observed in the parallel direction of the non-dipolar system. Slightly higher $G(\omega)_\perp$ values for the nematic phase indicate increased lateral resistance due to lack of in-plane order.

7.3 Nm and Sm at temperature 1.46

Having established the significant impact of dipolar interactions on phase behavior, structure, and viscoelastic response at $T^* = 1$, we extended our investigation to a slightly higher temperature, $T^* = 1.46$, to explore whether these effects persist or evolve under reduced thermal constraints. At this temperature, we performed simulations for both nematic and smectic phases, with and without dipolar interactions, following a similar analytical framework as before.

In contrast to the behavior observed at $T^* = 1$, where dipolar interactions induced a clear phase transition from nematic to smectic ordering, no phase transitions occurred at $T^* = 1.46$. Each system remained in its initial phase throughout the simulation duration. The nematic systems maintained orientational order, while the smectic systems preserved their layered structures. This

provided an opportunity to assess the structural and dynamical modifications induced by dipolar interactions without the phase change.

Figures 7.3.1 and 7.3.2 show snapshot configurations for all systems. In the nematic systems (top), the non-dipolar system exhibits moderate alignment, while the dipolar system shows slightly increased ordering due to the aligning effect of the dipoles. In the smectic systems (bottom row), layering is clearly visible in both cases, with more defined and stable layers in the dipolar system, suggesting enhanced positional order.

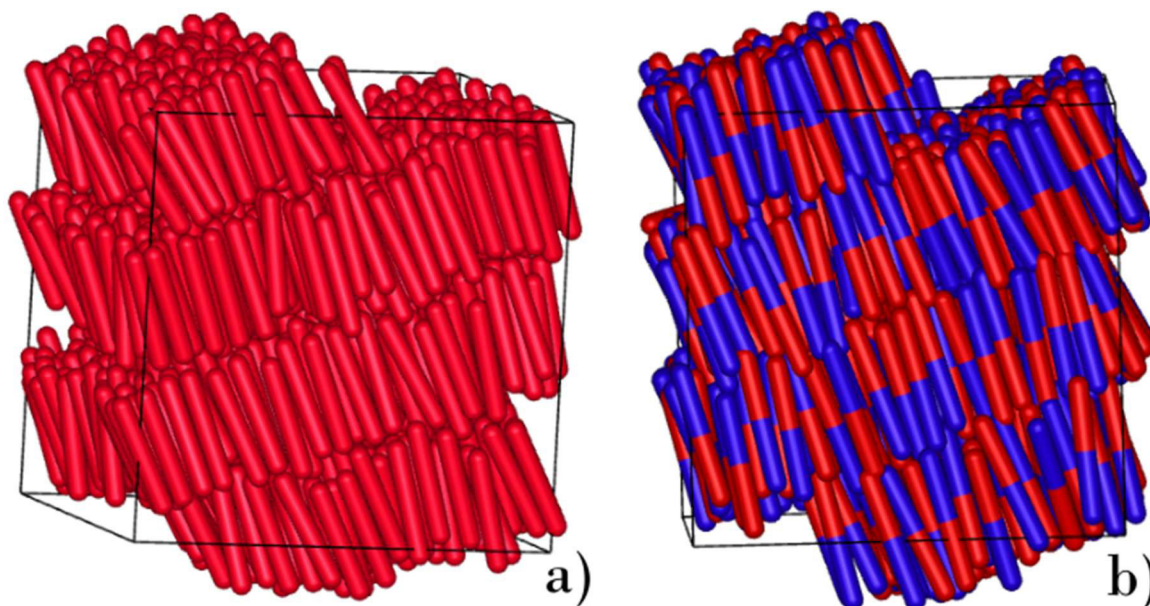


Figure 7.3.1 Snapshot configurations at $T^* = 1.46$. a) Sm phase without dipolar interactions. b) Nematic phase with dipolar interactions.

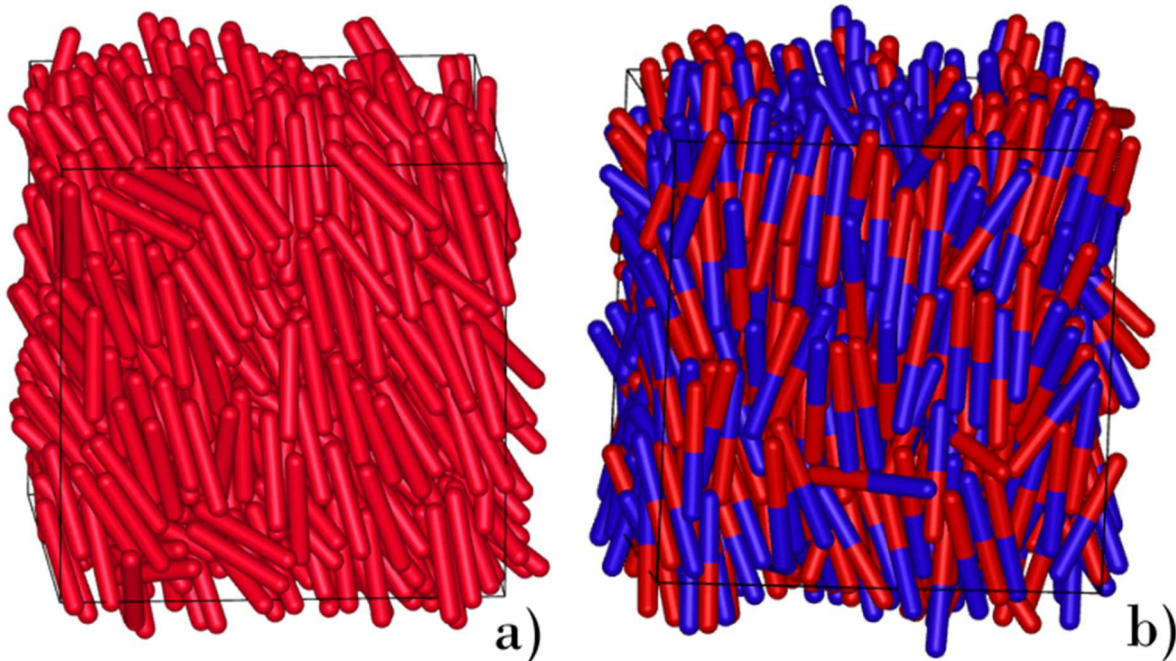


Figure 7.3.2 snapshot configurations at $T^* = 1.46$ a) Nm phase without dipolar interactions., b) Smectic phase with dipolar interactions.

To quantify the structural differences observed in the snapshots, we analyzed the pair distribution functions along and perpendicular to the director. These functions provide insight into how dipolar interactions influence positional correlations and the degree of local order within each phase.

In the nematic phase, dipolar interactions induce the appearance of small oscillations in $g(z)_{\parallel}$, which are absent in the non-dipolar system. These subtle features indicate the onset of positional correlations along the director, reflecting a tendency toward smectic-like ordering, but it is insufficient to drive a full phase transition. In contrast, in the smectic phase, dipolar interactions lead to sharper and more pronounced peaks in $g(z)_{\parallel}$ revealing enhanced layer definition and increased positional stability. The perpendicular distribution function shows only minor changes between dipolar and non-dipolar systems in both phases, suggesting that lateral correlations are less sensitive to dipolar effects and that the primary structural impact of dipoles is exerted along the director.

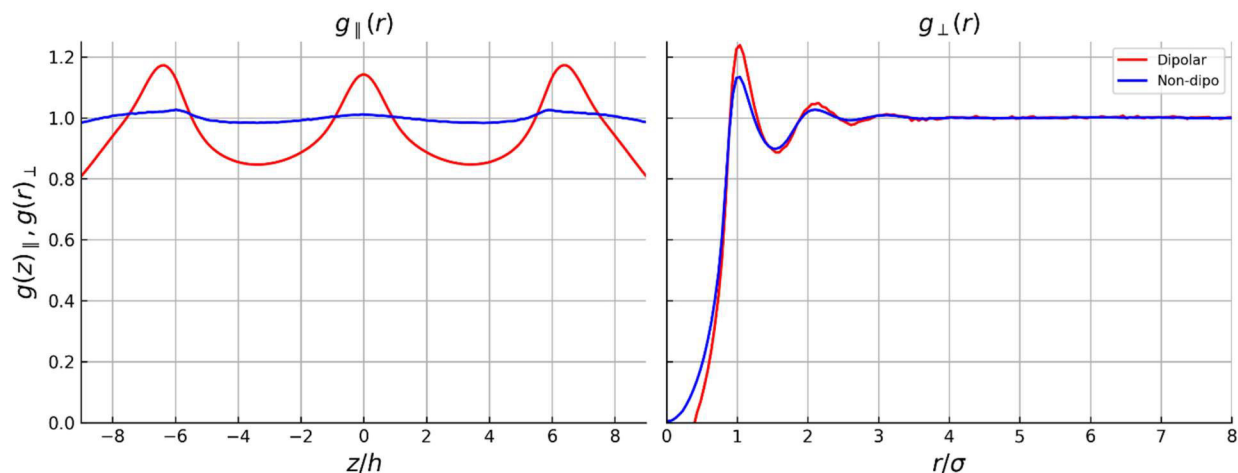


Figure 7.3.3a) Pair correlation functions $g(z)_{\parallel}$ and $g(r)_{\perp}$ for Nm phase at $T^* = 1.46$

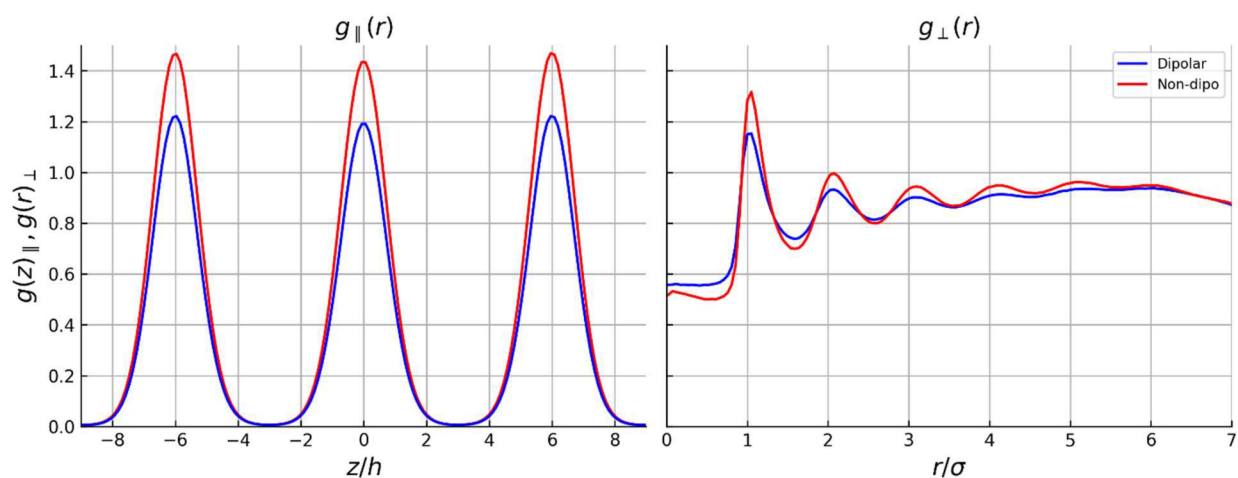


Figure 7.3.3b) Pair correlation functions $g(z)_{\parallel}$ and $g(r)_{\perp}$ for Sm phase at $T^* = 1.46$

To complement the structural analysis, the nematic order parameter S_2 was computed for both phases to quantify the degree of orientational alignment. In the nematic phase, the presence of dipolar interactions increases S_2 from approximately 0.7 in the non-dipolar system to around 0.8, indicating improved alignment along the director, as shown in Figure 7.3.4. In the smectic phase, a similar effect is observed, with S_2 rising from about 0.92 to nearly 0.97 in the dipolar system, approaching high orientational order. This result is consistent with previous findings that dipolar interactions can reinforce orientational order by promoting alignment along the molecular axis [7.6].

These results confirm that dipolar interactions enhance orientational alignment in both phases. This strengthening of local alignment, together with the previously discussed increase in positional correlations, demonstrates that dipolar forces act to reinforce both types of order, even in the absence of a phase transition at this temperature.

transition.

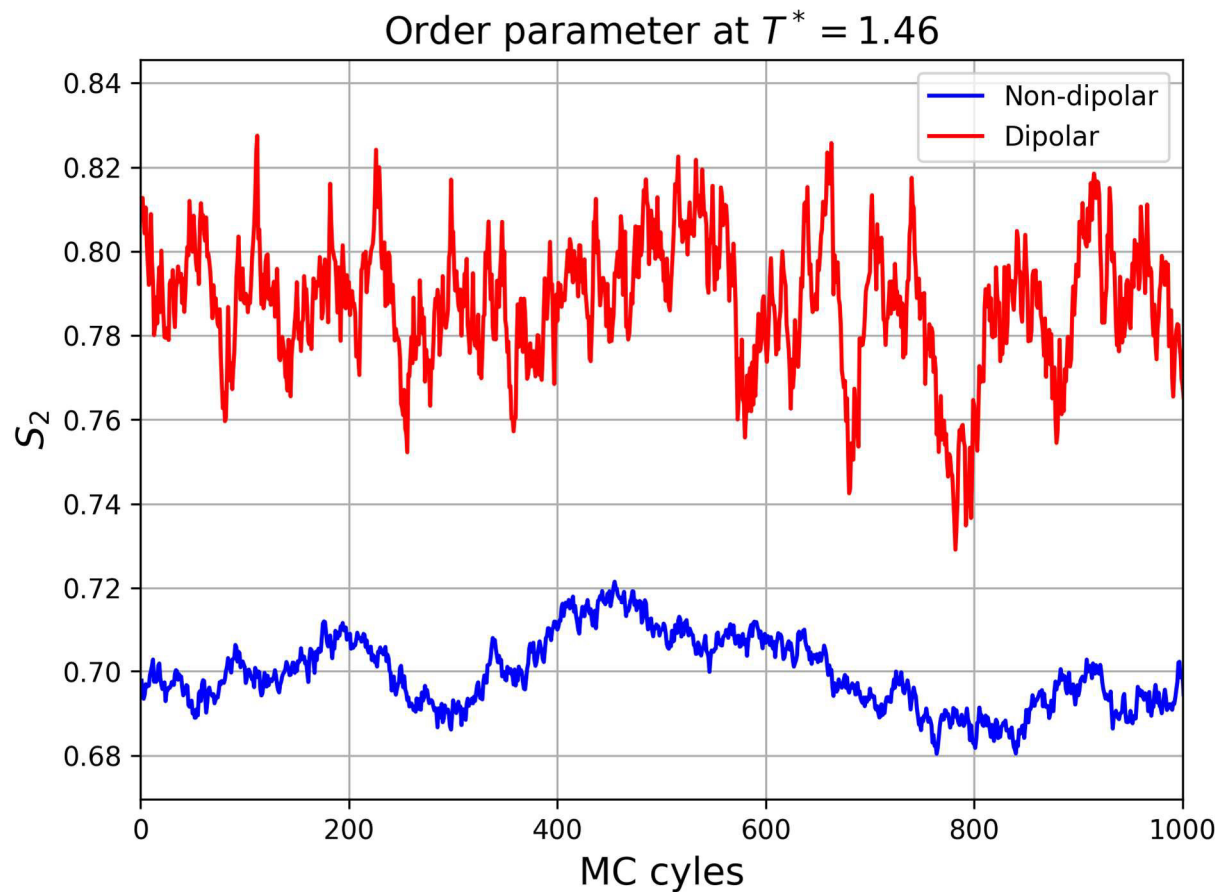


Figure 7.3.4 Nematic order parameter S_2 in the nematic phase at $T^* = 1.46$. The dipolar system shows enhanced orientational order, reaching values around 0.8.

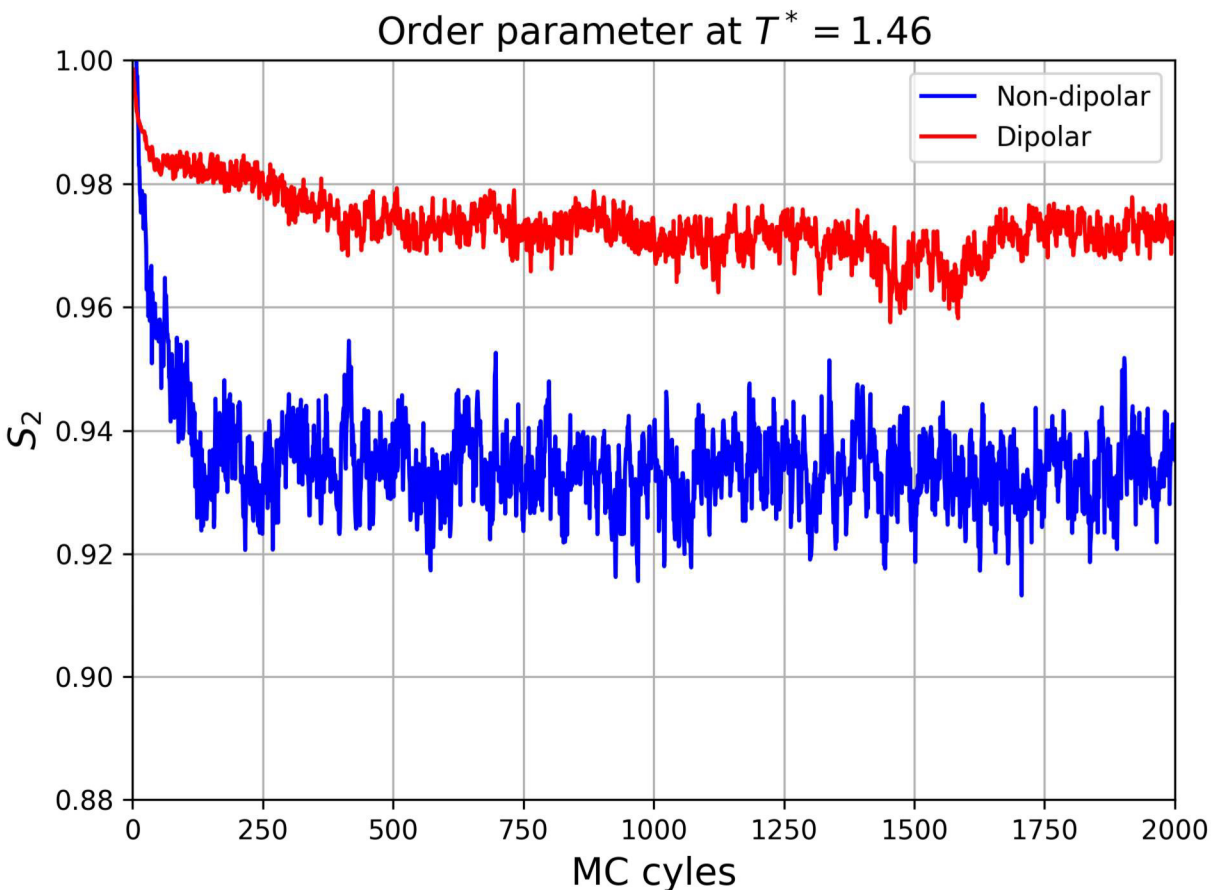


Figure 7.3.5 Nematic order parameter S_2 in the smectic phase at $T^* = 1.46$. Dipolar interactions increase S_2 from 0.938 to 0.98, indicating stronger alignment along the director.

Similar to the observations made at the lower temperature, the smectic dipolar snapshots at $T^* = 1.46$ also suggest the presence of a spontaneous alternation in rod orientation across layers, raising the possibility of ferro- or antiferroelectric behavior. To explore this phenomenon quantitatively, we computed the angular distribution of rod orientations relative to the director \mathbf{n} , defined by the angle θ between the rod axis and \mathbf{n} .

Figure 7.3.6 shows the resulting angular probability density function for the smectic phase at $T^* = 1.46$. In the non-dipolar system, a narrow peak centered at $\theta = 0^\circ$ is observed, indicating strong alignment of all rods with the director. In contrast, the dipolar system displays two distinct symmetric peaks at $\theta \approx 0^\circ$ and $\theta \approx 180^\circ$, confirming an equal distribution of rods pointing in opposite directions. This bimodal distribution highlights the dipolar-induced alternation in orientation, potentially indicative of local ferroelectric or antiferroelectric arrangements.

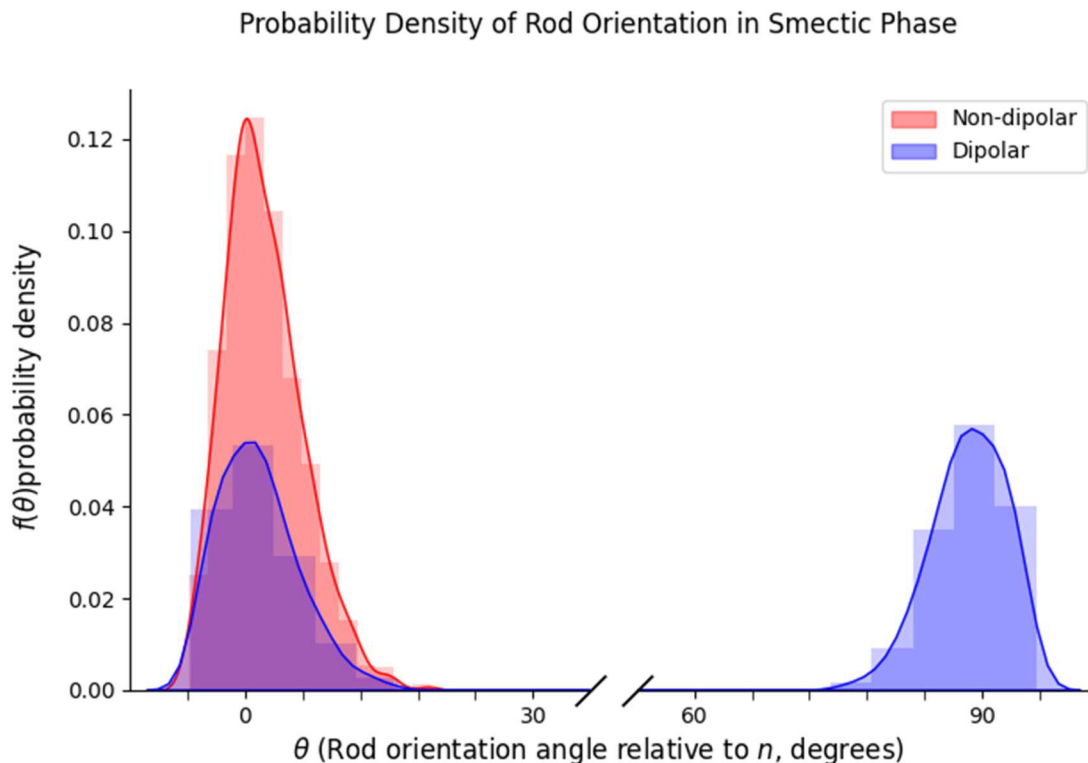


Figure 7.3.6 Probability density function of rod orientation relative to the director \mathbf{n} in the smectic phase at $T^* = 1.46$. The non-dipolar system (red) exhibits a narrow peak at $\theta \approx 0^\circ$, indicating strong alignment with the director. In contrast, the dipolar system (blue) shows a bimodal distribution with peaks at $\theta \approx 0^\circ$ and $\theta \approx 180^\circ$, suggesting equal populations of rods pointing in opposite directions.

To determine whether the observed bimodal orientation leads to any long-range polar order, we computed the first and third Legendre correlation functions, $S_1(r)$ and $S_3(r)$. As stated, a non-zero $S_1(r)$ would indicate net dipole alignment characteristic of ferroelectric order, while a significant $S_3(r)$ would suggest alternating dipole orientations consistent with antiferroelectric behavior.

As shown in Figure 7.3.7, both $S_1(r)$ and $S_3(r)$ remain near zero across all distances for dipolar and non-dipolar smectic systems, confirming the absence of long-range polar ordering. These results demonstrate that although local alternation of dipole orientation occurs, evidenced by the angular distribution, this does not translate into macroscopic ferroelectric or antiferroelectric phases under the simulated conditions. The dipolar interactions instead promote local orientational patterns without leading to global polar order.

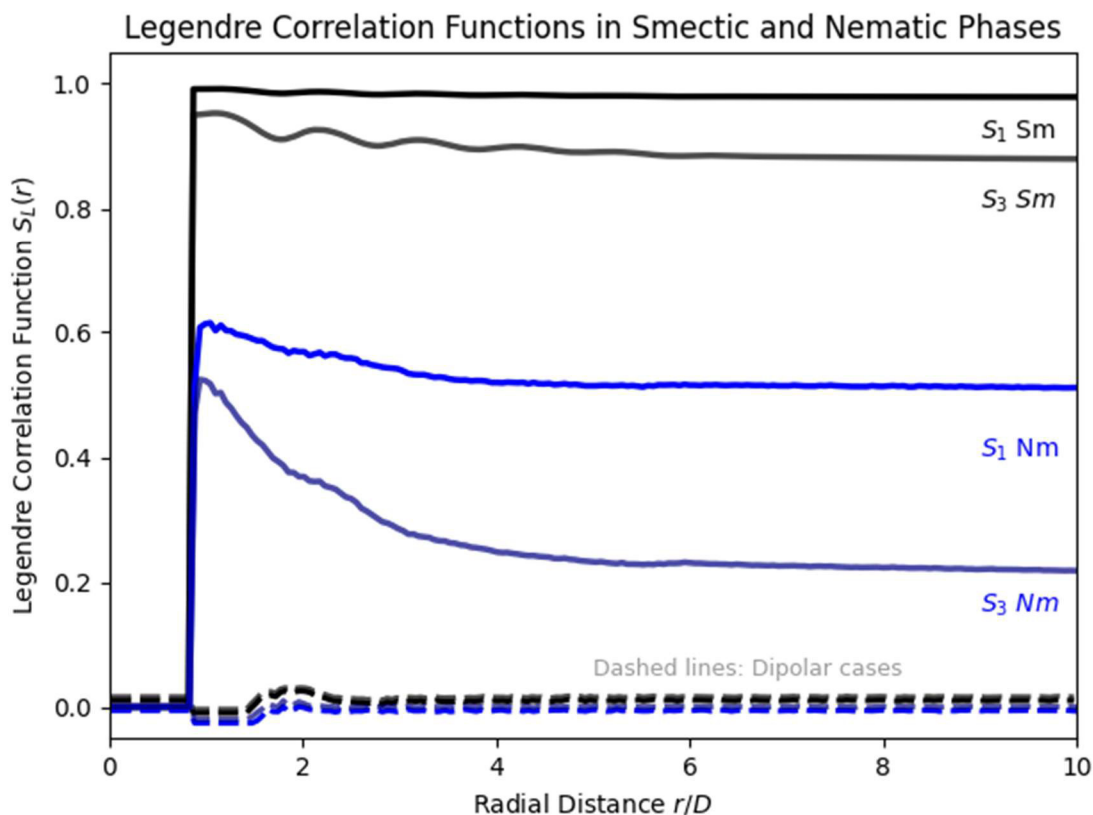


Figure 7.3.7 Legendre correlation functions $S_1(r)$ and $S_3(r)$ for dipolar and non-dipolar in smectic (black) and nematic (blue) systems at $T^* = 1.46$. In all cases, $S_1(r)$ and $S_3(r)$ remain near zero, indicating the absence of ferroelectric or antiferroelectric ordering.

To complement the structural analysis and assess how dipolar interactions impact the local mechanical environment, we investigated tracer dynamics through the calculation of the mean squared displacement in both parallel and perpendicular directions relative to the director. Figure 7.3.8 presents the MSD curves for tracer particles embedded in the nematic phase at $T^* = 1.46$ for both dipolar and non-dipolar systems.

Consistent with the anisotropy of the phase, the largest tracer displacements occur along the parallel direction. However, the presence of dipolar interactions leads to a notable reduction in parallel MSD, highlighting increased hindrance to motion along the director due to enhanced structural order induced by dipoles. In contrast, the perpendicular MSD displays only minor differences between dipolar and non-dipolar systems, suggesting that dipolar interactions have a less significant influence on tracer mobility in directions orthogonal to the director. These results confirm that dipolar-induced ordering restricts tracer motion primarily along the director axis, reflecting anisotropic viscoelastic resistance in the medium.

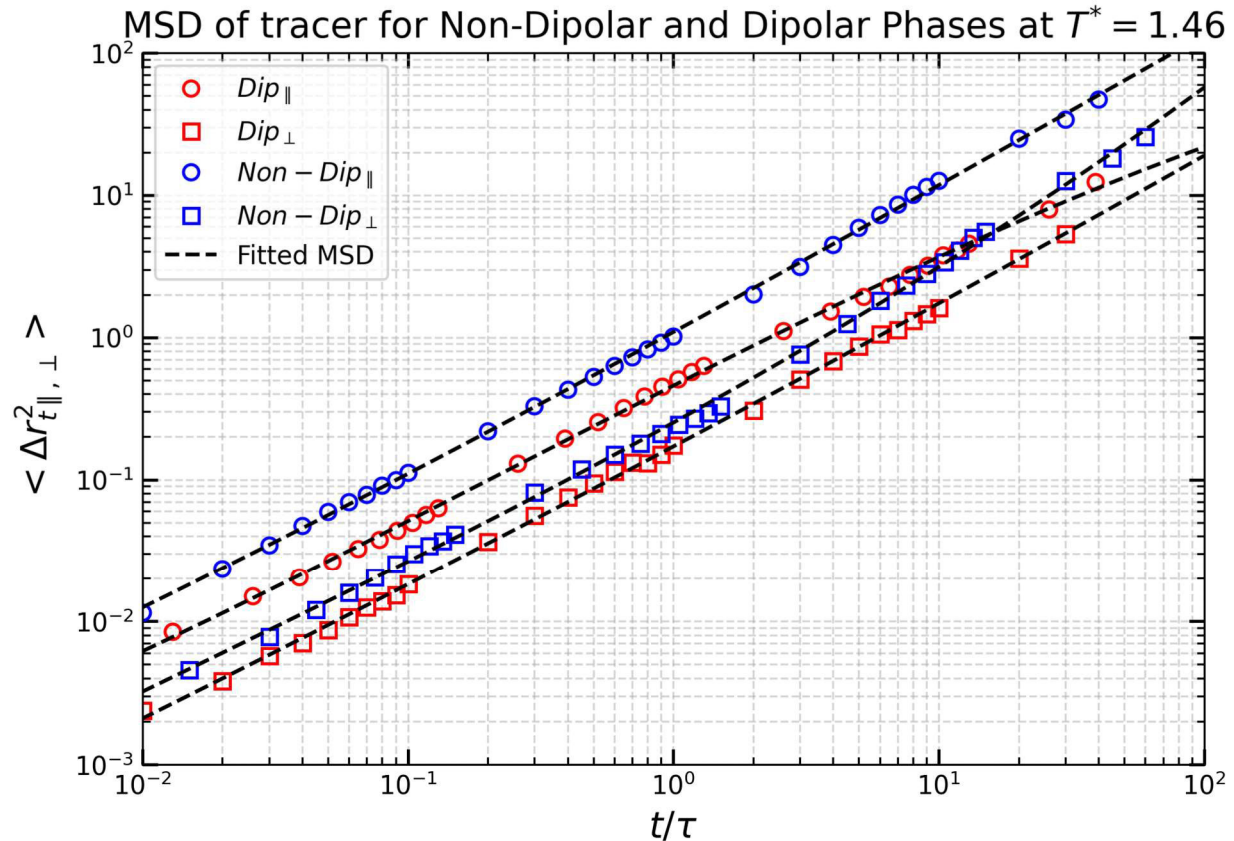


Figure 7.3.8 MSD of tracer particles in Nm phase in parallel and perpendicular directions for dipolar and non-dipolar systems at reduced temperature $T^* = 1.46$. Blue symbols correspond to the non-dipolar system, while red symbols represent the dipolar one. Circles and squares refer to parallel and perpendicular directions, respectively. The dashed line indicates a polynomial fitting.

The corresponding viscoelastic moduli $G'(\omega)$ and $G''(\omega)$ computed from tracer MSD using the Mason method, are shown in Figure 7.3.9. In the perpendicular direction, only modest differences arise between dipolar and non-dipolar systems, suggesting that while dipolar interactions introduce a slight increase in in-plane order, they do not significantly hinder lateral tracer motion.

In contrast, in the parallel direction, the viscoelastic moduli are substantially higher in the dipolar system across the frequency spectrum. This reflects the enhanced positional order and stiffness along the director due to dipolar interactions, which impede tracer motion and strengthen the material's elastic response. This effect becomes particularly pronounced at high frequencies, indicating an elastic-dominated regime associated with smectic-like layering that constrains motion along the director.

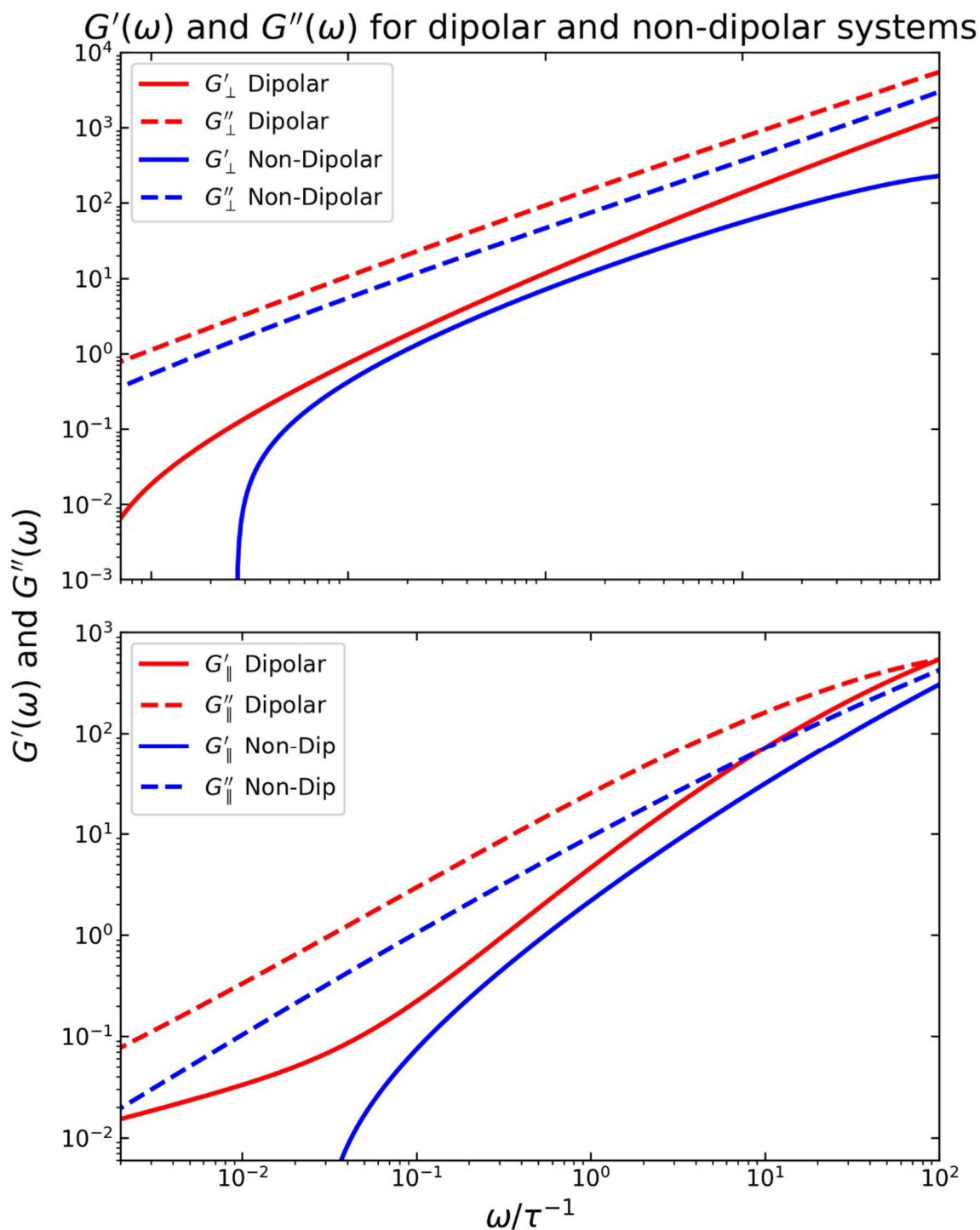


Figure 7.3.9 Viscoelastic moduli $G'(\omega)$ (continuous lines) and $G''(\omega)$ (dashed lines) for Nm phase calculated from tracer MSD using the Mason approach for nematic phases at $T^* = 1.46$ for non-dipolar (blue) and dipolar (red) systems. Top: perpendicular direction; bottom: parallel direction.

The MSD analysis for tracer particles in the smectic phase at $T^* = 1.46$ revealed a distinct anisotropic behavior. Contrary to what is observed in the nematic phase, where tracers move more freely along the parallel direction, in the smectic phase the displacements are larger in the perpendicular direction. This is evident from the increased slope of the MSD curve for the perpendicular direction compared to the parallel one. The confinement within smectic layers, combined with the highly ordered structure, restricts movement along the director axis, while allowing relatively easier diffusion across the layers. Similar behavior, showing enhanced tracer mobility in the direction perpendicular to the layers, has been reported in experimental and theoretical studies of smectic systems, and is attributed to the energetic barriers that arise from layer stacking and positional order [7.7]

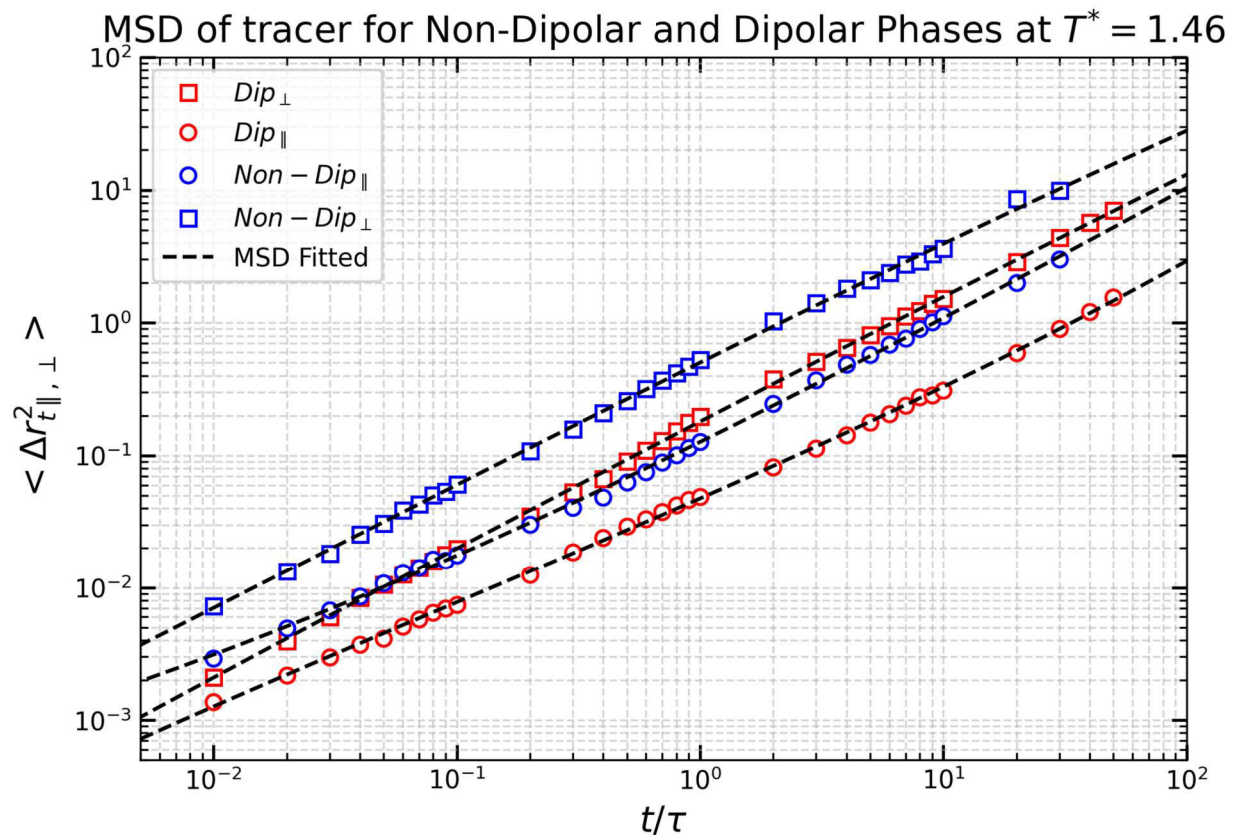
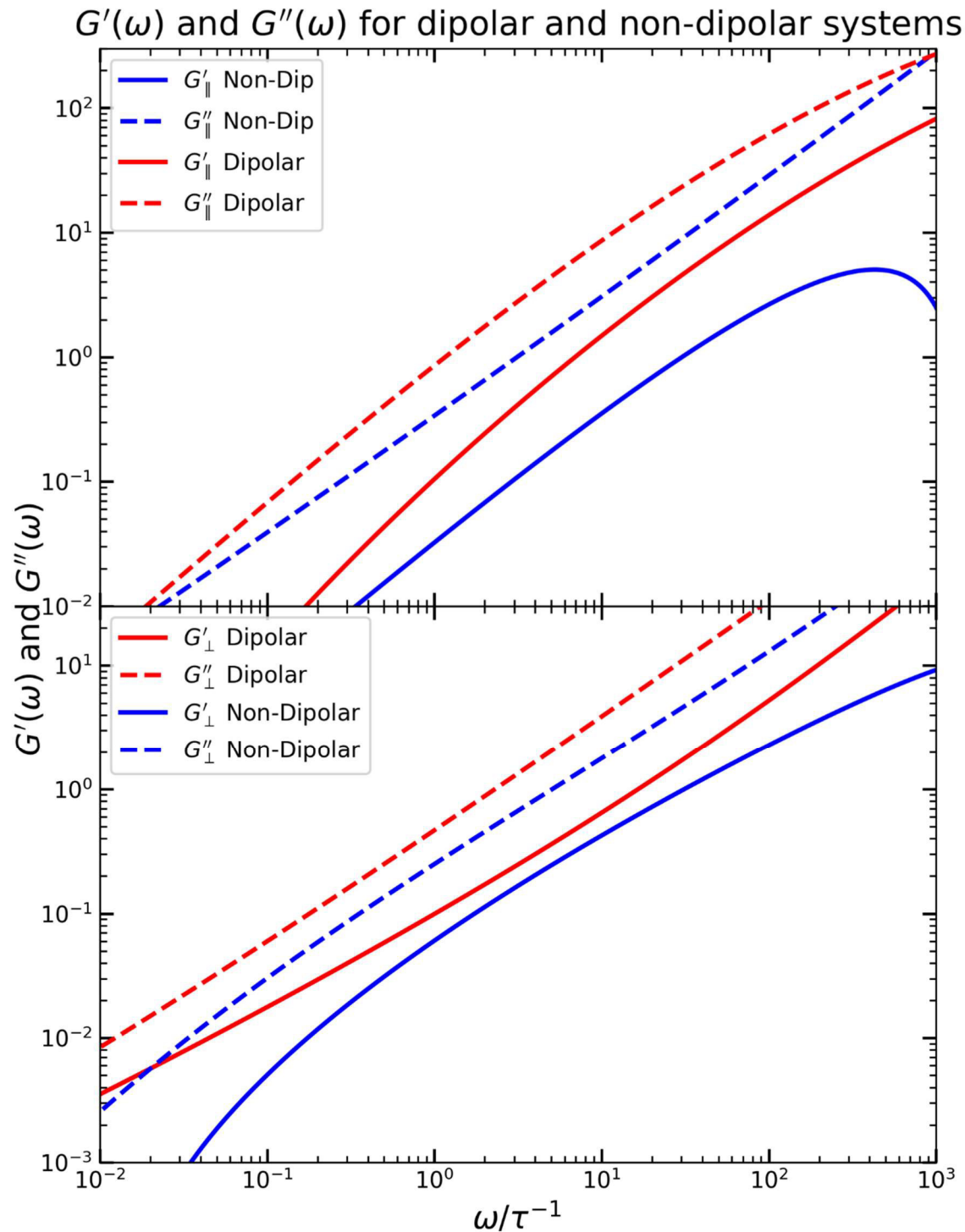


Figure 7.3.10 MSD of tracer particles in Sm phase in parallel and perpendicular directions for dipolar and non-dipolar systems at reduced temperature $T^* = 1.46$. Blue symbols correspond to the non-dipolar system, while red symbols represent the dipolar one. Circles and squares refer to parallel and perpendicular directions, respectively. The dashed line indicates a polynomial fitting.

We also computed the loss and storage moduli using microrheology analysis for both dipolar and non-dipolar systems. The results show that in the smectic phase, both moduli are significantly higher in the dipolar system, in both the parallel and perpendicular directions. This indicates that

the introduction of dipolar interactions increases the system's resistance to deformation, making it more viscoelastic. The presence of permanent dipoles enhances the rigidity of the system, suppresses tracer mobility, and increases energy dissipation under deformation, consistent with the observed MSD suppression in the parallel direction.



f

Figure 7.3.11 Viscoelastic moduli $G'(\omega)$ (continuous lines) and $G''(\omega)$ (dashed lines) for Sm phase calculated from tracer MSD using the Mason approach for nematic phases at $T^* = 1.46$ for non-dipolar (blue) and dipolar (red) systems. Top: perpendicular direction; bottom: parallel direction.

In the smectic phase, the impact of dipolar interactions is even more pronounced. The values of $G'(\omega)$ and $G''(\omega)$ are substantially higher than in the nematic case, especially in the parallel direction (along the layers). This reflects the combined effects of layered positional order and dipolar alignment, which reinforce mechanical rigidity. The storage modulus $G'(\omega)$, in particular, shows a steeper slope at low frequencies in the dipolar smectic system, highlighting its more solid-like behavior.

Interestingly, the gap between dipolar and non-dipolar systems widens in the smectic phase compared to the nematic one, indicating that dipolar interactions have a stronger influence when positional order is present. This confirms that dipoles enhance viscoelasticity not only by orientational effects but also by stabilizing and stiffening the layered structure.

Moreover, both directions, parallel and perpendicular, show increased $G'(\omega)$ and $G''(\omega)$ in the dipolar smectic phase, but the difference is more noticeable in the parallel direction, consistent with the observed confinement of tracers and suppression of motion along the director.

These results confirm that dipolar interactions contribute to increased viscoelasticity in both nematic and smectic phases, although their influence is more pronounced in systems where positional order, such as layering, plays a dominant role.

Finally, to gain further insight into the local dynamics of tracer particles in the nematic phase at $T^* = 1.46$ we analyzed their individual trajectories along the x, y, and z directions over time (Figure 7.3.12). The results reveal a clear anisotropy in tracer motion. Substantial fluctuations are observed in both the x and y directions, indicating relatively unrestricted in-plane diffusion. In contrast, displacement along the z-axis is markedly limited. The tracer remains largely confined within a single smectic-like layer, exhibiting only one transition to an adjacent layer approximately at the midpoint of the simulation.

This behavior highlights the presence of energy barriers that impede inter-layer movement, likely arising from the enhanced positional order and structural constraints imposed by dipolar interactions. The increased order along the director (z-direction) fosters the formation of well-defined layers, which restrict vertical tracer mobility, effectively trapping it within a layer for extended durations.

As a result, tracer motion becomes highly constrained along the z-axis, leading to elevated viscoelastic resistance in this direction. This is directly reflected in the significantly higher values of $G'(\omega)$ and $G''(\omega)$ observed for the dipolar system in the parallel case. The confinement and ordering induced by dipolar interactions enhance the system's elastic stiffness along the director,

establishing a direct connection between microscopic structural organization and the macroscopic viscoelastic response.

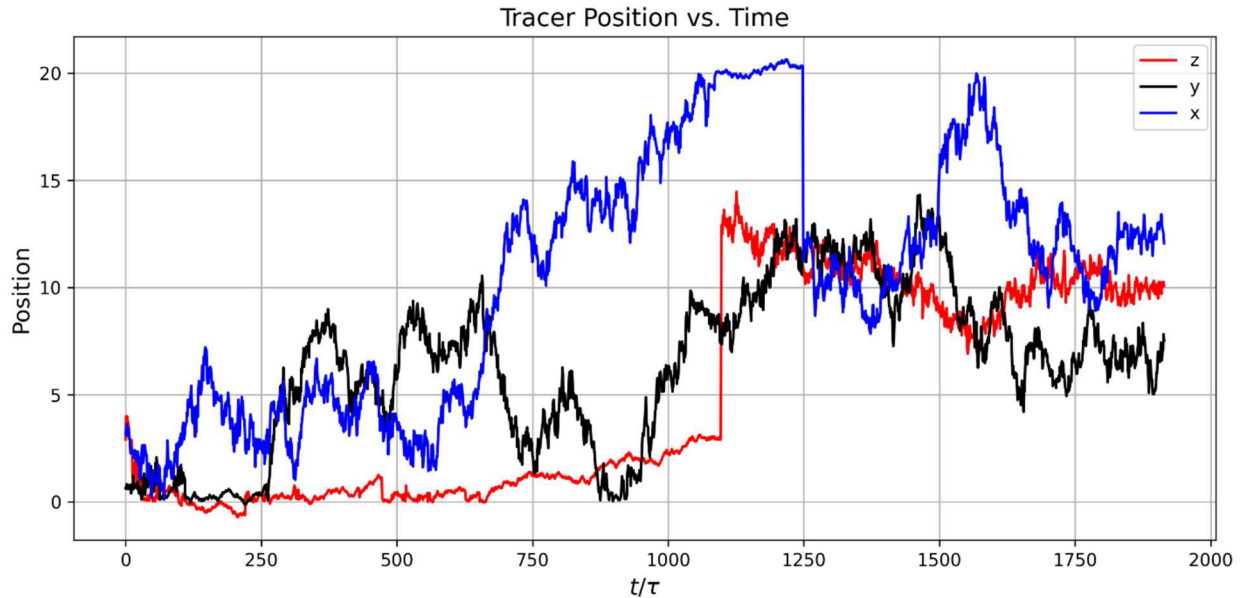


Figure 7.3.12 Trajectories of a tracer particle along x (black), y (blue), and z (red) directions in the nematic dipolar system at $T^* = 1.46$. The tracer exhibits significant movement in the x and y directions but remains confined along z, indicating layer localization. Only one layer transition is observed during the simulation. The restricted z-motion suggests energy barriers due to dipolar-induced layering, contributing to enhanced viscoelastic resistance in the parallel direction.

The analysis of tracer particle displacement along the z-axis revealed a clear confinement within a single smectic-like layer for most of the simulation time, as shown in figure 7.3.12. The displacement graph shows that the tracer remains in one layer with minimal fluctuation, followed by a sudden transition to a neighboring layer, after which it becomes confined again. These rare inter-layer jumps suggest the presence of energy barriers associated with the layered structure. This behavior is consistent with the experimental observations described by Fujii et al., who reported that the smectic layering imposes significant resistance to motion perpendicular to the layers due to structural constraints and energy barriers [7.7].

8 Applications of liquid crystals and practical experience during internship

In this chapter, we reflect on the broader relevance of liquid crystal research and its intersection with industrial applications.

While the focus of this thesis is on the theoretical and computational study of colloidal liquid crystals, particularly in nematic and smectic phases, the physical principles governing liquid crystal behavior is also central in many practical technologies.

To complement the fundamental work presented in this dissertation, a research internship was undertaken at AlphaMicron Inc., a company that develops and manufactures liquid crystal-based optical devices. This experience provided valuable insights into how liquid crystal materials are engineered and integrated into functional systems such as smart eyewear and displays.

The following sections describe two specific applications of liquid crystals studied during the internship: guest-host systems for adaptive lenses and the use of photoalignment techniques. Though distinct from the simulation-based work of this thesis, these technologies are grounded in the same physical phenomena and illustrate the real-world relevance of liquid crystal science.

8.1 Applications of liquid crystals in the industry

Liquid crystals (LCs) have enabled a wide range of technological innovations across various industries. Historically, their unique optical and electro-optical properties have been widely exploited in the development of display devices such as televisions, watches, and calculators. In recent years, their applications have expanded to include advanced systems such as virtual reality (VR) lenses, eyewear, and smart windows.

The importance of the research in liquid crystals relies in the fact that it is necessary to understand and characterize the behavior of the particles that compose the liquid crystals to be able to modify them to achieve suitable optical, dielectric and rheological properties depending on the application.

Here we will focus on two specific applications. The first one is guest-host liquid crystal cells used in dynamic eyewear, and the second application is LC devices that employ photoalignment techniques for enhanced optical control.

These two applications were studied during an internship at at the company AlphaMicron Inc. (Kent, Ohio, USA), a leading developer of LC-based technologies for commercial and defense-related applications.

8.2 Applications of liquid crystals in eyewear

There are some situations where the human eye needs to be protected against rapid changes in environmental lighting conditions and guest-host liquid crystals are particularly suitable for this purpose due to their unique optical properties. They can adjust the opacity of the films, enabling the creation of variable transmission lenses that enhance visual clarity and reduce glare.

At AlphaMicron, a sophisticated method is employed to adjust the transmission of the LC cells, that contain a mixture of liquid crystals and dichroic dyes. When a voltage is applied, the orientation of the LC molecules changes, which in turn alters the alignment of the dye molecules. Since these dyes absorb light anisotropically, the system's optical transmission can be precisely controlled by the applied field.

There are various studies that model how the dipole aligns with the molecular axis of the dye particles. These studies are crucial for understanding and optimizing the interaction between the dye molecules and the liquid crystal host, which directly impacts the efficiency and performance of the liquid crystal cells. By analyzing these alignments, researchers can design more effective systems for applications such as adaptive eyewear, where precise control over light absorption and transmission is essential. [21]

Here, we describe liquid crystal cells fabricated through a process learned at AlphaMicron, which utilizes a mixture of dyes and chiral nematic liquid crystals. These cells are specifically designed for use in eyewear applications. The devices operate on the principle that the dye guest aligns with the liquid crystal host. By applying an electric field, the orientation of the liquid crystal matrix can be switched between a high transmission and lower transmittance colored states. This occurs because the anisotropic absorption of dichroic dyes follow the electro-optical response of the liquid crystal molecules. Such guest-host devices do not necessarily require polarizers or color filters, as the absorption properties are defined by the guest dye molecules and their alignment. Consequently, they may provide more robust devices with higher optical efficiencies and lower power consumption compared to some conventional polarized based liquid crystal eyewear. This innovative technology in smart eyewear offers enhanced visual comfort and protection by dynamically adapting to changing light conditions.

The process of making these liquid crystal cells is described in the following chapter.

8.3 Internship experience: Liquid crystals eyewear

During my internship at AlphaMicron, I was trained in the complete fabrication process of guest-host LC cells for eyewear applications.

The fabrication process begins with the preparation of empty LC cells made of polycarbonate substrates coated with ITO (indium tin oxide), which acts as a conductor. The cells also contain small spherical spacers which are used to maintain uniform cell thickness, as depicted in the following diagram

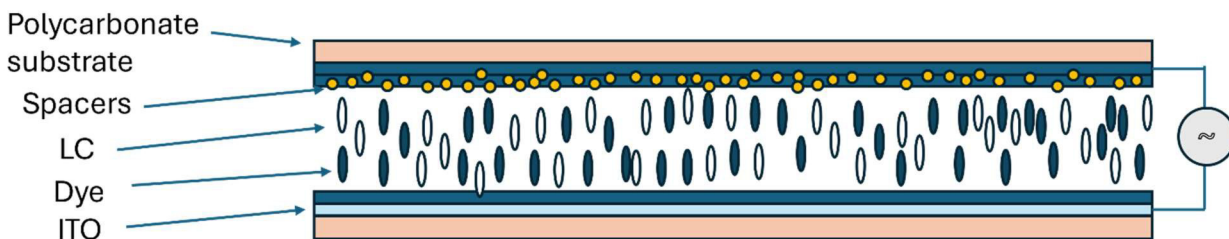


Figure 8.3.1. Schematic representation of a guest–host liquid crystal cell. The cell consists of two polycarbonate substrates, each coated with a transparent Indium Tin Oxide (ITO) electrode. These electrodes allow an electric field to be applied across the cell. Between the substrates, a mixture of liquid crystals (LC) and dichroic dyes is confined. Small polymer spacer beads are dispersed across the substrates to maintain a uniform cell gap, ensuring consistent alignment. The LC molecules, along with the dye guests, reorient in response to the applied electric field.

A UV-curable glue is applied along the perimeter to form a sealed rectangular enclosure, as shown in Figure 8.3.2, into which the LC-dye mixture will later be injected.

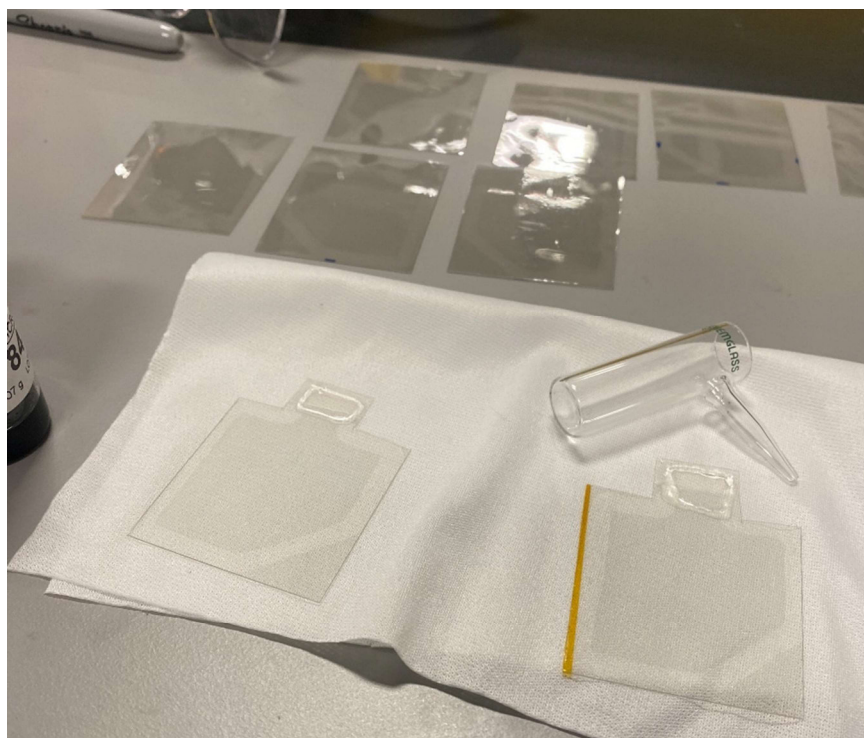


Figure 8.3.2 Two empty cells containing indium tin oxide (ITO) and spacers. On top, a rectangular seal of glue has been applied to define the filling area.

After this, the cell is placed inside a vacuum chamber, where the mixture of liquid crystals and dyes is poured into the rectangular enclosure formed by the UV glue.

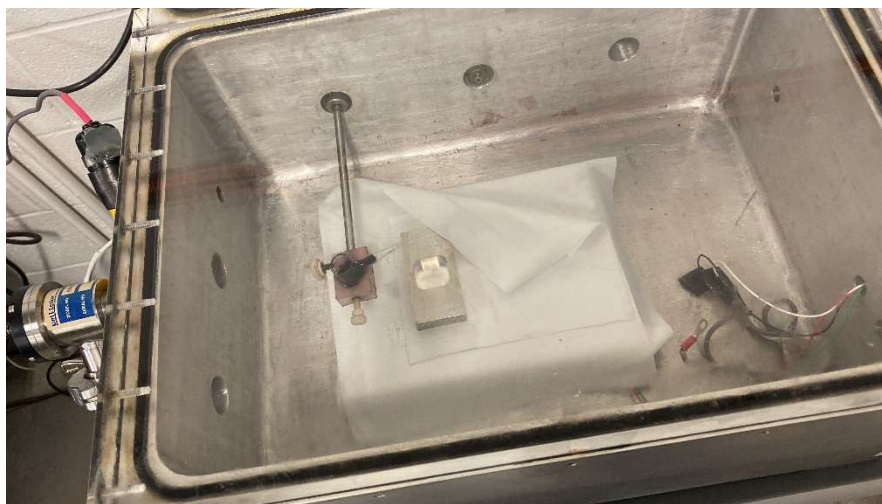


Figure 8.3.3 LC cell inside the vacuum chamber.

In this step, the cell is positioned within the vacuum chamber, where the surrounding air is evacuated to create a low-pressure environment. This low-pressure condition enhances the capillary action, allowing the dye solution to infiltrate the cell more effectively.

Once the vacuum chamber is turned off, the mixture of liquid crystals and dyes fills the polycarbonate cell through a capillary action, as illustrated in the following image.

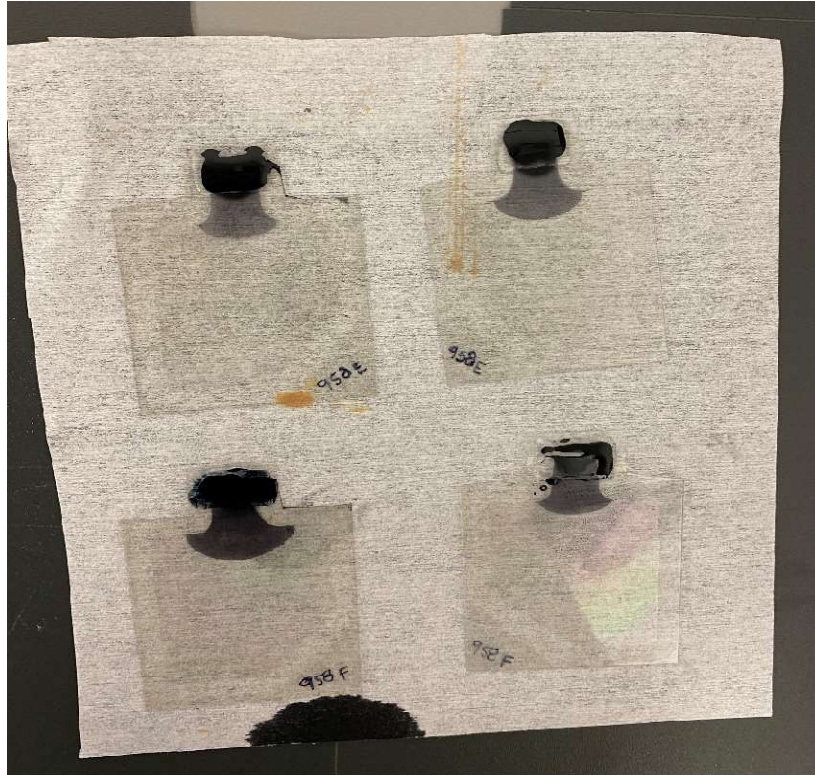


Figure 8.3.4. The process of filling a cell with dyes through capillarity after the cell has been placed inside a vacuum chamber.

As capillary action takes effect, the dye solution is drawn into the cell, gradually filling it from the bottom up.

The capillarity filling process takes approximately 5 hours and continues until all empty spaces within the cells are fully occupied, as shown in the following figure.

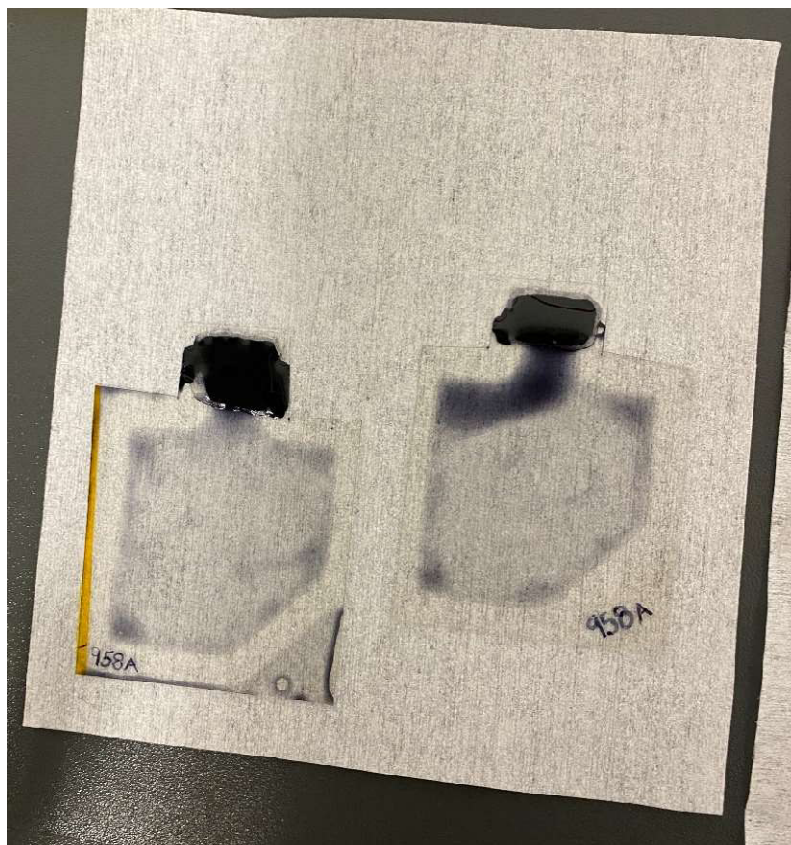


Figure 8.3.5. Capillary filling process completed. The liquid crystal cells have been successfully filled with liquid crystals and dyes through capillary action. The filled regions are visible, indicating uniform infiltration of the material inside the sealed area.

Once the cells are completely filled, they must be cleaned to remove any excess material, ensuring a homogeneous film inside. After this, the cells are sealed with UV glue to prevent air from entering. Once sealed, the cells are placed in a holder and taken to the spectrometer for characterization of their absorption and transmission properties.



Figure 8.3.6. Placement of the cell in a holder for optical characterization

After fabrication, the liquid crystal cell is mounted on a holder and characterized using a spectrometer. This process involves comparing the cell's light absorption with and without an applied voltage.

As discussed in the previous section, applying voltage alters the elastic response of the liquid crystal, causing the dye molecules to reorient into a planar twisted configuration, resulting in increased light absorption and making the cell appear darker, as depicted in the following diagram

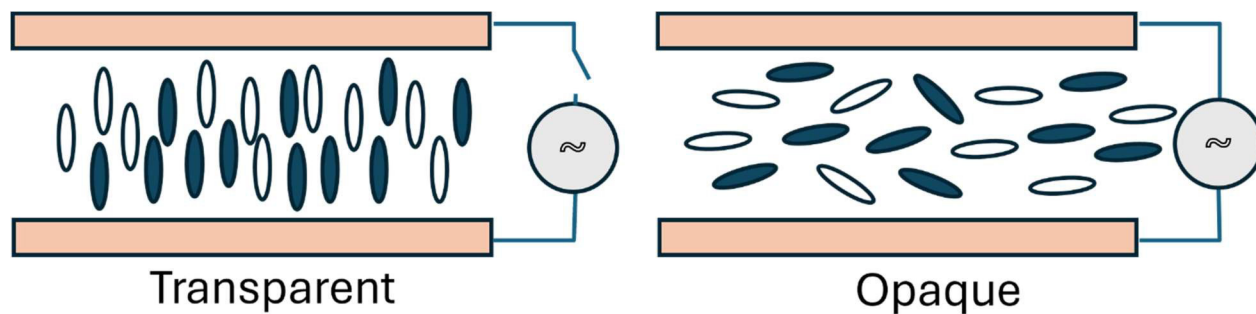


Figure 8.3.8 Optical states of a guest–host liquid crystal cell under different electrical conditions.

In the absence of an electric field (left), the liquid crystals and dye molecules align uniformly, minimizing light absorption and resulting in a transparent state. When an electric field is applied (right), the alignment is disturbed. The dye molecules no longer follow a uniform orientation, increasing light absorption and scattering. This leads to an opaque appearance. The optical response of the system is thus controlled by the alignment of the dichroic dye molecules within the liquid crystal host, which responds to the applied voltage.

The perceived darkness and final color of the cell depend on the specific dye used and its concentration. By selecting different dyes, a variety of optical effects can be achieved, enabling custom tuning of the device's transmittance and color properties to meet specific eyewear applications.

The image below displays cells filled with different types and concentrations of dyes, allowing for a variety of colors and optical properties.



Figure 8.3.9. Example of liquid crystal cells filled with different dyes. Each cell contains a different dye mixture, resulting in variations in color and light absorption. The selection of dyes influences the optical properties of the cells, which can be tailored for specific applications.

The following picture displays a different type of cell used to create a specific kind of eyewear. In this example, it can be noticed that the cell resembles more the cells used to fabricate eyewear and the dye used is a mixture of blue dyes, chosen to achieve particular optical properties. This selection of dyes allows for customized color performance and light absorption characteristics, tailored to the intended application of the glasses.

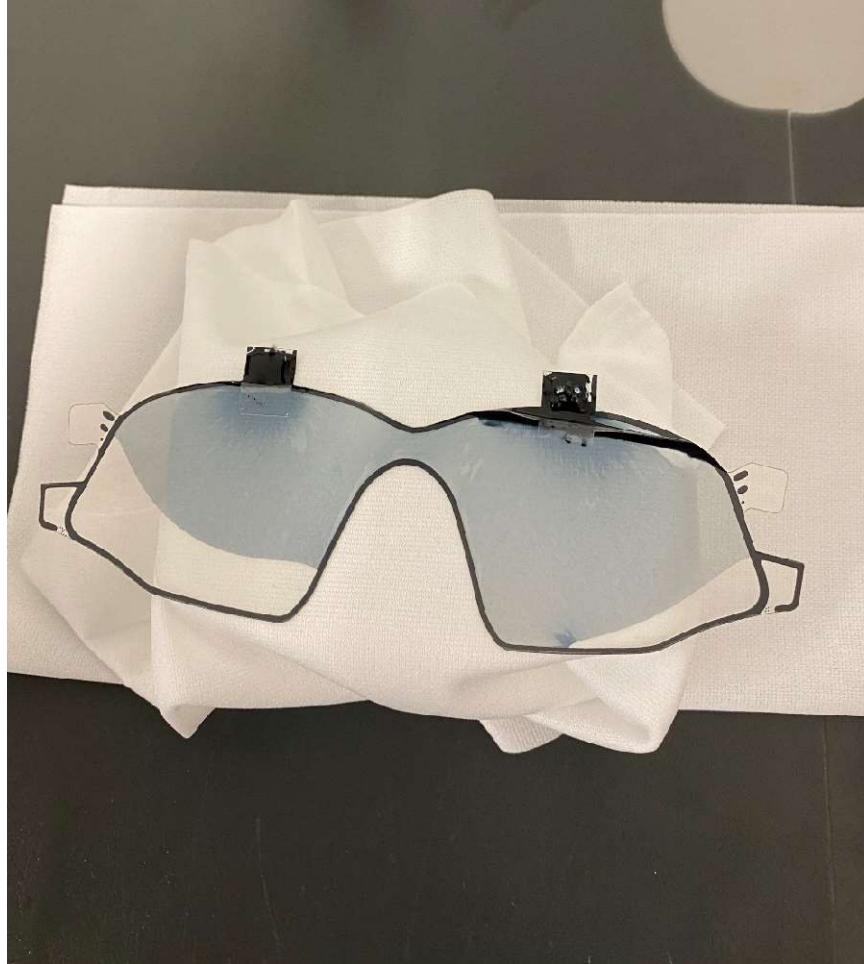


Figure 8.3.10. Example of a different model of cell filled with a mixture of blue dyes.

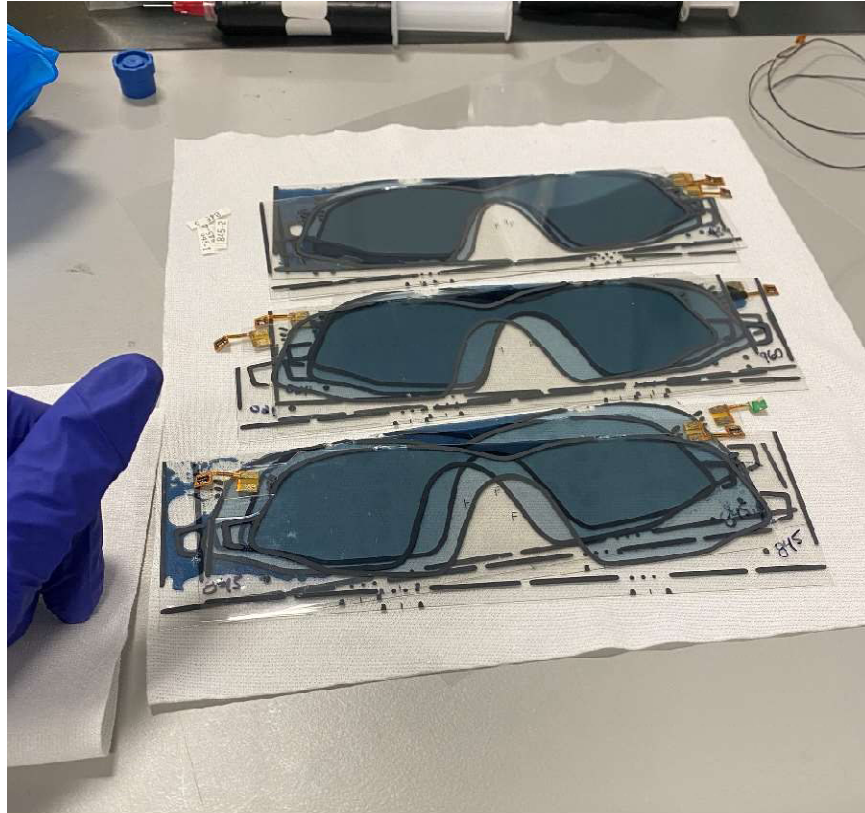


Figure 8.3.11. Liquid crystal cells filled with a mixture of blue dyes and equipped with flexible connectors (flexes). The flexes allow for electrical connections to apply voltage to the cells and control the liquid crystal alignment. These completed eyewear-shaped cells are now ready for optical characterization and performance testing.

In figure 8.3.11 we show the result once we completed all the steps presented in this chapter. The cells are prepared for use with uniform dye distribution and are ready for optical characterization.

8.4 Internship experience: Liquid crystals photoalignment

Liquid crystals are also widely used in advanced optical devices, and photoalignment techniques play a crucial role in their performance. During my internship at Alphamicon I was also involved into the development of different liquid crystal devices requiring photoalignment techniques. Azobenzene is a compound frequently used in photoalignment applications due to its ability to undergo reversible photoisomerization when exposed to ultraviolet (UV) light. In the photoalignment process, this material is exposed under a UV laser and its molecules can change their orientation in response to light, thereby influencing the alignment of liquid crystal layers. This process aligns the AZO molecules in a precise pattern, which in turn dictates the orientation of the liquid crystal molecules. Such controlled alignment is essential for optimizing the optical properties of LC cells. The ability to precisely manipulate the liquid crystal alignment enables the development of high-performance devices with applications in areas such as virtual reality (VR)

glasses, where accurate light modulation and display quality are critical. This technology also benefits other advanced optical systems, including high-resolution displays and adaptive lenses, by improving their functionality and versatility.

The process of photoalignment of the LCs consists of various steps which are described in the following paragraphs.

First, a layer of photoalignment material is applied to one side of a polycarbonate substrate containing indium tin oxide (ITO) using spin coating. Then it is baked briefly for 30 seconds. Once the photoalignment material is evenly coated, the substrate is exposed to a UV laser to create a specific photoalignment pattern. This pattern determines the orientation of the liquid crystal molecules.

After the photoalignment process, a layer of UV glue is applied to the substrate. A drop of liquid crystal is then dispensed onto the glue. We rub the other substrate mechanically and apply spacers. The assembly of the cell is completed using a vacuum filling process, which creates a vacuum to sandwich the two sides of the substrate together and ensure the liquid crystal is evenly distributed throughout the cell. This process is summarized in the following diagram.

Photoalignment of LC cell

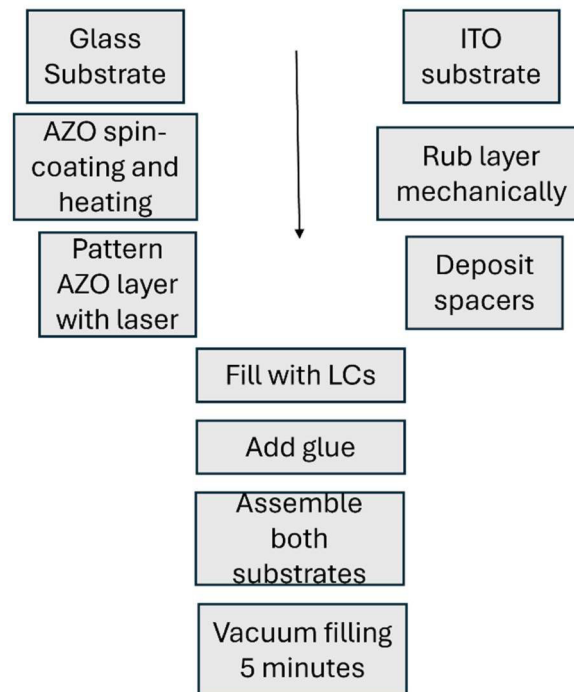


Figure 8.4.1. Step-by-step fabrication process of a liquid crystal cell using photoalignment and guest–host configuration. The left path describes the preparation of the substrate with the AZO photoalignment layer, which is spin-coated, baked and optically patterned using a polarized laser. The right path shows the preparation of the counter-substrate, which includes an ITO layer and its mechanical rubbing.

Once the cell has been assembled and filled with the liquid crystal mixture, it is possible to verify the photoalignment pattern by observing the cell under a polarizer. The alignment of the liquid crystals can produce visible birefringence effects, which manifest as colorful patterns when viewed between crossed polarizers. These patterns result from the optical anisotropy of the aligned nematic phase and can indicate whether the photoalignment was successful and uniformly transferred across the substrate.

In the example shown below (figures 8.4.2 and 8.4.3), the cell fabricated during the internship exhibits a clearly visible interference pattern, confirming the presence of photoinduced alignment within the material

It is possible to see the polarization of the material making use of a linear polarizer. The polarizer is rotated and the polarization of the material inside the cell can be observed.

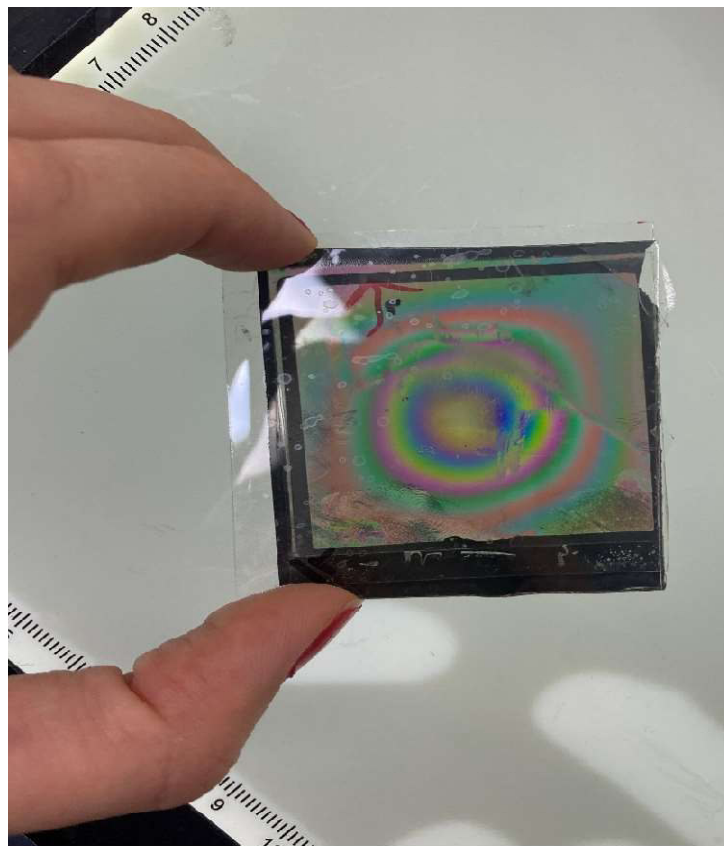


Figure 8.4.2 Photoaligned glass cell filled with nematic liquid crystal analyzed under a linear polarizer at position 1, highlighting the patterned molecular alignment induced during fabrication.

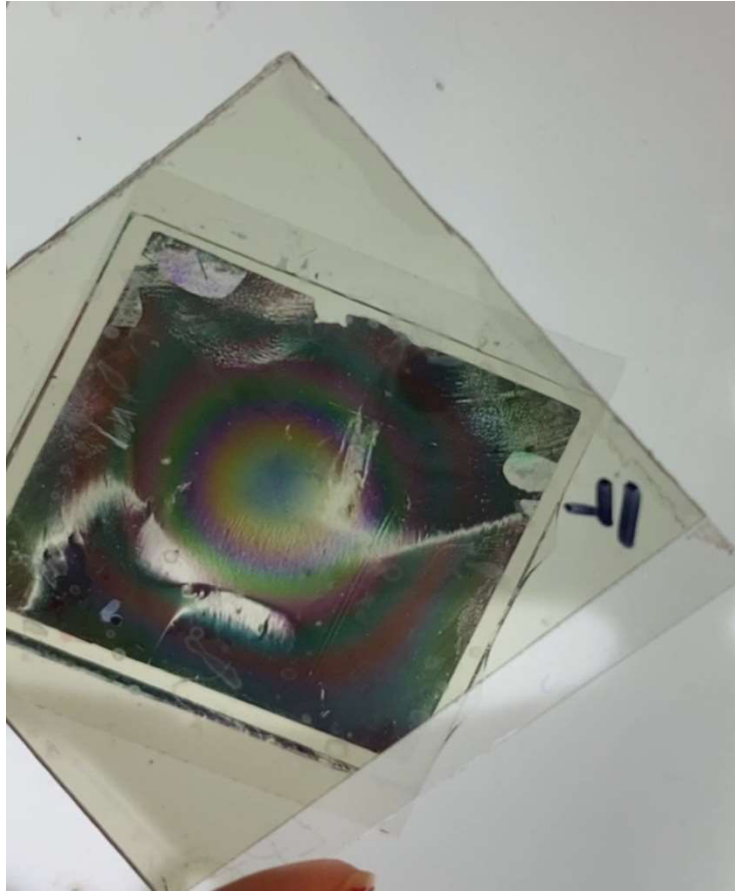


Figure 8.4.3 Photoaligned glass cell filled with nematic liquid crystal analyzed under a linear polarizer at position 2.

The sample cell is then examined using crossed polarized illumination under the microscope using a linear polarizer to verify that the photoalignment pattern has been correctly made and that the pattering lines created with the UV laser are not overlapping, creating undesired effects. Confirmation of the photoalignment is achieved by observing a gradient of color within each pattern, as illustrated in the following picture.

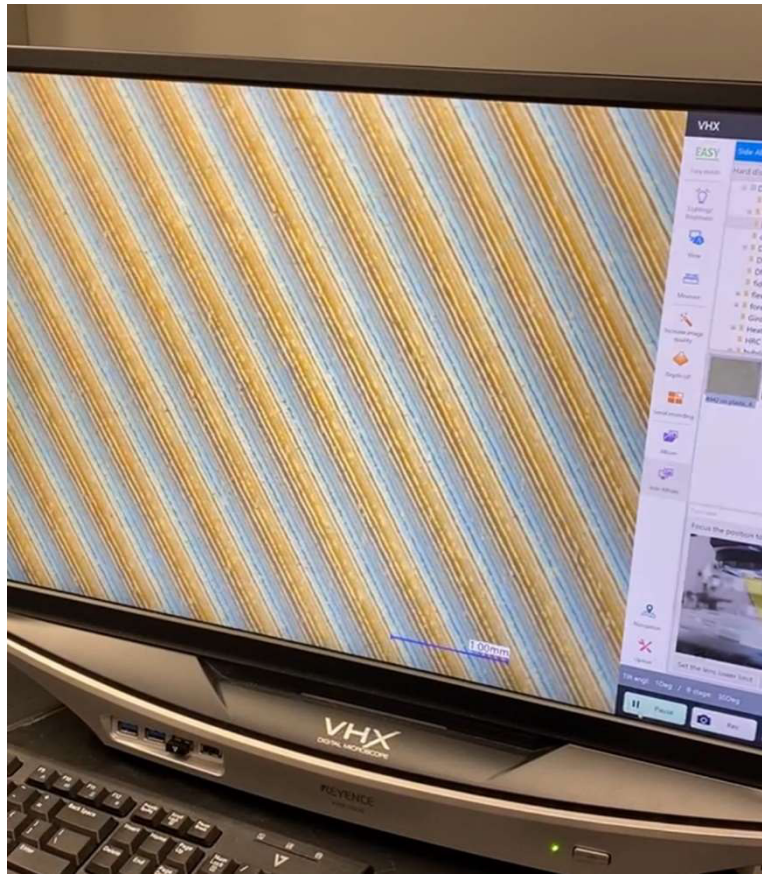


Figure 8.4.4 Picture of a photoaligned nematic liquid crystal cell under the crossed-polarized light microscope.

9 Conclusions and Perspectives

In summary, this thesis has explored the dynamics of soft-repulsive rod-like particles within nematic and smectic liquid crystals through Dynamic Monte Carlo (DMC) simulations. We calculated a comprehensive spectrum of dynamical properties that characterize the long-time relaxation behavior both along and perpendicular to the nematic director. Key findings include the calculation of mean square displacements (MSD), which were essential in determining self-diffusion coefficients and understanding their temperature dependence. Our analysis unveiled the existence of particles capable of displacing significantly longer distances than the average over the same time frame, shedding light on the complex dynamics within these systems.

We calculated a range of dynamic properties to characterize the long-time relaxation behavior both parallel and perpendicular to the nematic director. Specifically, the MSD was key in determining the self-diffusion coefficients and assessing their dependence on temperature. The static structure factor (s-VHF) highlighted the presence of particles that can cover significantly greater distances compared to most particles over the same period, while the iSF provided insights into the timescales of structural fluctuation decay. Moreover, we investigated the temperature-dependent behavior of the intermediate scattering functions, revealing distinct dynamics between the nematic and smectic phases.

The incorporation of dipolar interactions through the reaction field method allowed us to investigate their profound effect on structural organization and microrheological response. At $T^* = 1$, we observed that dipolar interactions strongly promote orientational and positional order, inducing a nematic-to-smectic phase transition. This was supported by enhanced peaks in the parallel distribution function, increased S_2 and the formation of well-defined smectic layers. Despite the visual alternation in dipole orientation, no macroscopic ferroelectric or antiferroelectric ordering was found, as confirmed by angular distributions and the parameters $S_1(r)$ and $S_3(r)$, which remained near zero.

Dipolar interactions also strongly suppressed rod and tracer mobility along the director, leading to increased viscoelastic moduli $G'(\omega)$ and $G''(\omega)$ in the parallel direction. This indicates higher elastic resistance due to dipole-induced layering, particularly at high frequencies where $G'(\omega)$ dominates. Conversely, in the perpendicular direction, only modest changes in viscoelastic moduli were observed, suggesting that dipoles have less influence on lateral dynamics.

At $T^* = 1.46$, a similar analysis showed that dipolar interactions no longer induce a phase transition, and both nematic and smectic systems retained their original phase. Nevertheless, dipoles still enhanced structural ordering: in nematic systems, small oscillations appeared in $g(z)_{\parallel}$ while in smectic phases, peaks in $g(z)_{\parallel}$ became sharper. The nematic order parameter S_2 increased in both phases (from 0.7 to 0.8 in nematic; 0.92 to 0.98 in smectic), confirming stronger alignment. In the smectic dipolar system, a bimodal angular distribution ($\theta \approx 0^\circ$ and 180°) was again observed, but $S_1(r)$ and $S_3(r)$, confirmed the absence of global polar order.

Microrheological analysis in the nematic phase at $T^* = 1.46$ showed anisotropic tracer dynamics. Tracer particles exhibited greater displacement in the parallel direction, with dipolar interactions reducing mobility along this axis. The perpendicular MSD curves were similar between dipolar and non-dipolar systems, indicating limited dipolar influence laterally. The viscoelastic moduli $G'(\omega)$ and $G''(\omega)$ calculated from tracer MSD reflected these trends, with significantly higher values in the parallel direction for dipolar systems, consistent with enhanced rigidity and layered confinement.

Trajectory analysis of tracer particles further confirmed layered confinement along the z-axis, with tracers remaining within a smectic-like layer and only rare transitions between layers. This behavior highlights energy barriers imposed by dipolar-induced ordering, explaining the increased viscoelastic resistance along the director.

In conclusion, dipolar interactions have a strong influence on both structural and viscoelastic properties in liquid crystal phases, particularly at lower temperatures. They enhance phase order, restrict motion along the director, and increase mechanical rigidity, especially in smectic-like systems. These results offer insight into how dipolar interactions influence structure and viscoelastic behavior in anisotropic systems, which could be relevant for understanding or guiding the design of materials used in optical, display, or biological applications.

Looking to the future, there are several possible directions for extending this research. One immediate step is to explore the effects of varying particle shapes and sizes on the rheological properties of liquid crystals. It would also be worth exploring refinements in the modeling of dipolar interactions, for example by incorporating higher-order multipoles or flexible dipoles, as suggested in recent studies of polar fluids and soft matter systems (Cifelli et al., *Soft Matter* 2020; Vanakaras & Photinos, *Liq. Cryst.* 1995). This could offer a more realistic description of anisotropic colloidal suspensions or organic mesogens, especially in biological or electro-optic applications.

Another important direction is to expand the range of temperatures, densities, and dipole strengths explored in the simulations. This would help map out the full phase behavior of dipolar spherocylinder systems and could reveal new mesophases, such as twist-bend nematics or ferroelectric smectics, which have been reported in experimental studies (Chen et al., *Nature* 2013).

Future studies could also couple microrheology simulations with external fields, such as magnetic or electric fields, to mimic conditions in active systems and smart materials. These fields are known to influence viscoelastic properties and alignment and studying them in simulations could be relevant for understanding liquid crystal elastomers, responsive gels, or biological tissues where external stimuli play an important role.

Finally, combining this simulation approach with machine learning techniques could help identify hidden structure–property relationships, such as clustering formation, or enable faster prediction of optimal parameters for mechanical or dynamic behavior in soft matter systems. These directions could significantly contribute to the understanding of dipolar interactions in anisotropic fluids and

open new opportunities for applications in physics, chemistry, and materials science, from biological systems to advanced soft materials.

Appendix I

In this appendix, we present two examples of the Metropolis algorithm applied to probability sampling. The first example demonstrates the generation of a normalized histogram following an exponential distribution, while the second example applies the method to a Gaussian distribution. The histograms obtained from the Metropolis sampling are compared with the corresponding analytical distributions to validate the implementation.

The following figures depict the results obtained from the Metropolis method. The corresponding code written in python is listed in Appendix II.

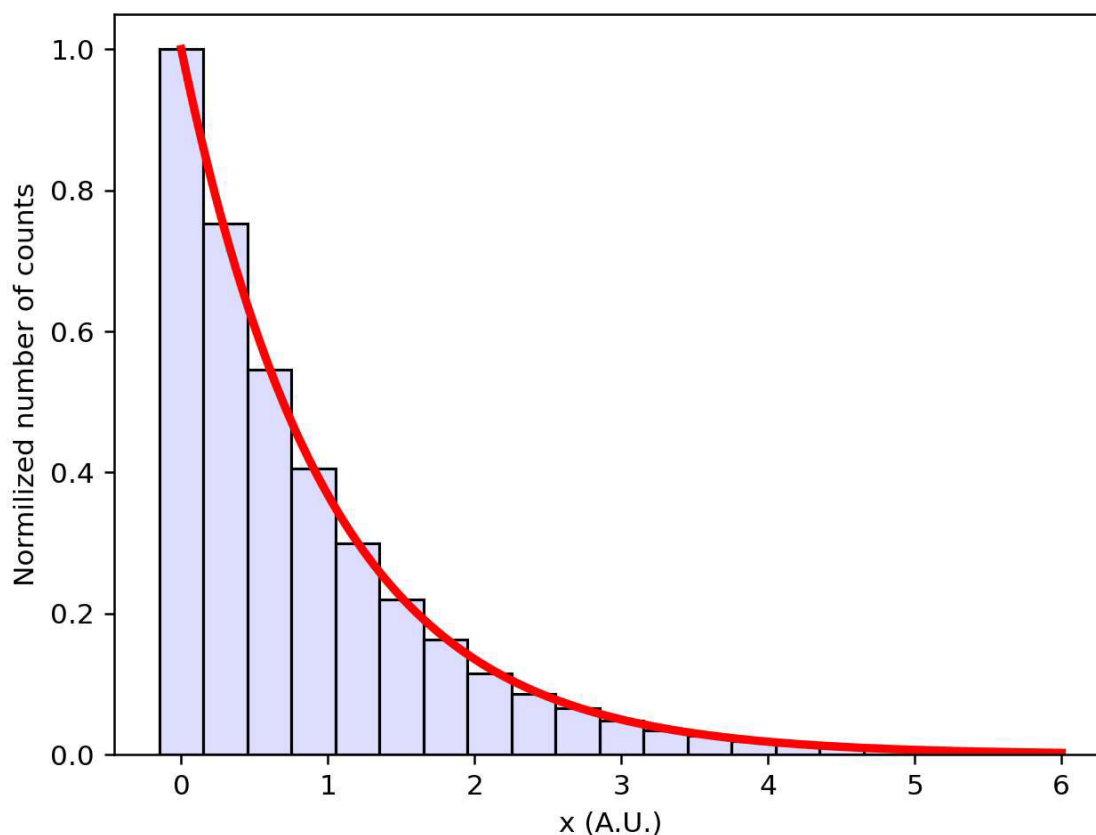


Figure A1. Normalized histogram obtained with Metropolis compared with the analytical target distribution $\exp(-x)$

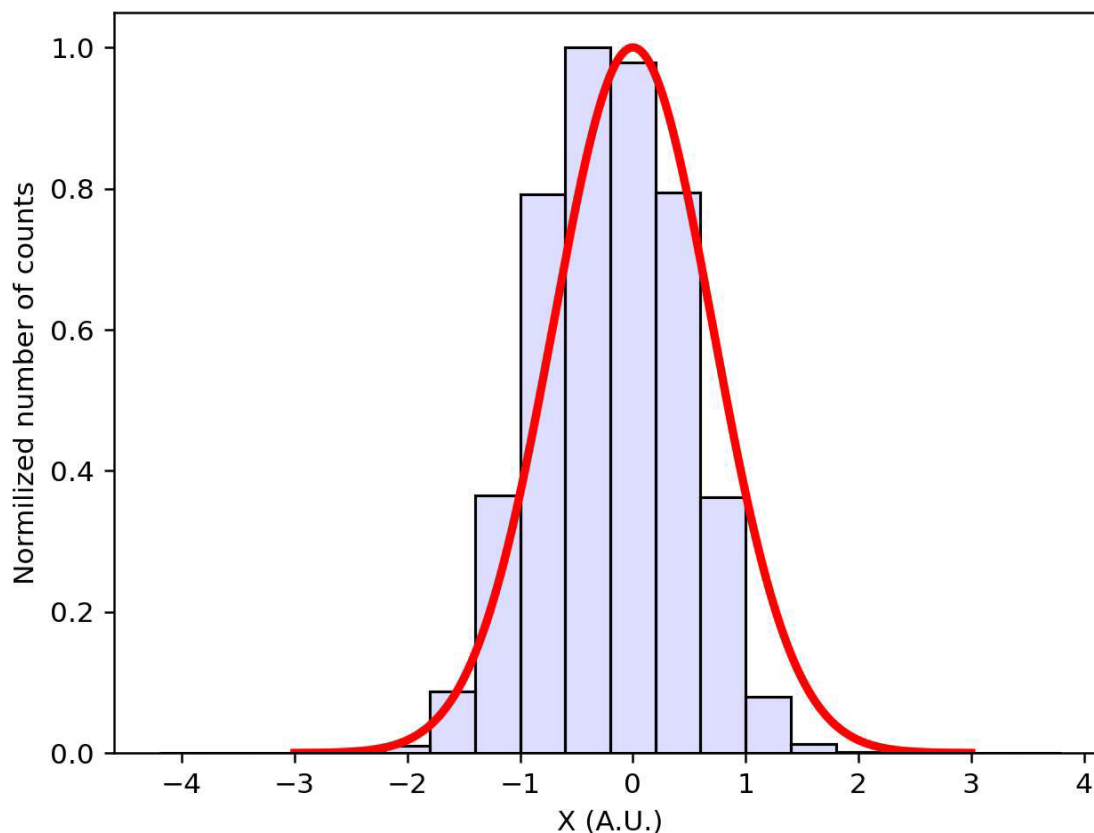


Figure A2. Normalized histogram obtained with Metropolis compared with the analytical target distribution $\exp(-x^2)$

The histograms in Figures A1 and A2 show the distributions obtained from the Metropolis algorithm. The red line represents the expected analytical distribution, and the blue bars depict the sampled data. The agreement between the sampled and analytical distributions confirms that the Metropolis method accurately reproduces the desired probability densities. Minor deviations at the tails may be attributed to statistical noise due to finite sample size.

These examples demonstrate the effectiveness of the Metropolis method for probability sampling. Beyond this simple application, the algorithm is widely used in Monte Carlo simulations for more complex systems, such as molecular dynamics and statistical physics models.

*Appendix II**Metropolis Algorithm Code*

Metropolis Algorithm

```

r0=1.0
def Target(x):
    if(x<0):
        return 0
    else:
        return np.exp(-((x-3)**2)/r0**2)

N=4000;
x=np.zeros(N+1);
x[0]=3; # Initial Value
for n in range(1,N+1):
    a=x[n-1];
    b=a+ np.random.normal(0,1); #
    p=np.random.rand(1)*1; # Generate number between 0 and 1
    A=Target(b)/Target(a);
    if (p<A):
        x[n]=b; # Accept value
    else:
        x[n]=a; # Don't accept value and repeat value a

s=np.zeros(N+1)
f=np.zeros(N+1)
for n in range (0,N+1):

    s[n]=(n-(N/2))/N*6+3

    f[n]=np.exp(-((s[n]-3)**2)/r0**2)

Histo=np.histogram(x,bins=10)
XX=Histo[1][0:10]

Fig1=plt.figure(1);
#plt.hist(x, bins=30);
plt.plot(s,f, linewidth=3.0, color='r')
plt.bar(XX,Histo[0]/1050)
Fig1.show();

```

Appendix III

Radial distribution function pseudocode

Here, we describe the algorithm used to compute the radial distribution function $g(r)$ in our simulations. Unlike the theoretical definition, where $g(r)$ is expressed as a sum over Dirac delta functions, numerical implementations require discretization using histograms. The algorithm is as follows.

Let N_p represent the total number of particles in the system and N_B the number of bins in the histogram that will represent $g_{\perp}(r)$ or $g_{\parallel}(r)$, which, for simplicity, will be represented only by $g(r)$.

The bins will be separated a radial distance Δr . Therefore $\Delta r = N_B/L$. The parameter L represents the dimensions of the box, which, for simplicity, are considered equal.

With the above conditions, $g(r)$ is composed by N_B discrete variables, $g[0], g[1], g[2] \dots g[N_B - 1]$.

The program first initializes to zero the histogram as follows.

For $i=0$ to N_B-1 :

$$g[i] = 0;$$

Now, we compute the distance between the particles and fill the histogram with the following pseudocode.

For $i=0$ to N_B-2 :

For $j=i+1$ to N_B-1 :

$$r = |\mathbf{r}_i - \mathbf{r}_j|;$$

$$x' = x - L * \text{int}(x'/L); \quad y' = y - L * \text{int}(y'/L). \quad \# \text{ Periodic boundary conditions as described in 3.3.1.}$$

$$r' = \sqrt{x'^2 + y'^2}$$

$$m = \text{int}(r' / \Delta r); \quad \# \text{ Choose the correct bin.}$$

$$g[m] = g[m] + 2; \quad \# \text{ Found two particles in this bin.}$$

The above pseudocode counts the number of particles in each bin.

We have to normalize the histogram. This is done as follows.

We compute the volume of each bin as follows.

$$Volume[i] = 4/3\pi(\mathbf{r}_{i+1}^3 - \mathbf{r}_i^3), \text{ with } \mathbf{r}_{i+1} = (i+1)\Delta r, \text{ and } \mathbf{r}_i = i\Delta r.$$

Therefore, the volume of the i -bin is given as, $Volume[i] = 4/3\pi\Delta r^3((i+1)^3 - i^3)$.

With this condition, each normalized bin, is written as, $g[i] = g[i]/(2 * N_p * Volume[i])$.

Appendix VI

Visualization of the rods configurations

We can visualize the configurations of the particles contained in the colloidal phases calculated by the Monte Carlo simulations by creating a program to place each of the spherocylinders at their corresponding spatial coordinates within a cubic box. While this task may be extensive, there are various open-access codes already available to accomplish this task. We will utilize the VISUAL COLLOIDS tool, developed by Michiel Hermes, and can be accessed through the link in reference [8.1]. This tool enables us to draw different geometrical shapes such as spheres, cylinders, spherocylinders, and others. We have chosen this tool due to its friendly useability and in the following lines we describe the parameters required by the program in order to render the spherocylinders in their positions inside a specific cubic box.

To accomplish the task mentioned above, we will refer to figure VI.1. It is necessary to provide the program with the coordinates of the centers of mass of each rod, denoted as (x_0, y_0, z_0) . In our case, the centers of mass of the rods coincide with their geometrical centers and, pointed and depicted by the vector \mathbf{A} in the figure. Additionally, to establish the orientation of the rods, we define a unit vector, denoted as $\hat{\mathbf{u}} = (u_x, u_y, u_z)$, aligned with the major axis of the spherocylinder. This vector must be unitary, and it will be multiplied by a scalar L to set the length of the rod to this value. Finally, two additional vectors, $\mathbf{V} = (V_x, V_y, V_z)$ and $\mathbf{W} = (W_x, W_y, W_z)$, perpendicular to each other and both orthogonal to vector $\hat{\mathbf{u}}$, forming a triad, need to be provided. The lengths of \mathbf{V} and \mathbf{W} determine the rod's diameters along their respective directions, as depicted in Figure VI.1.

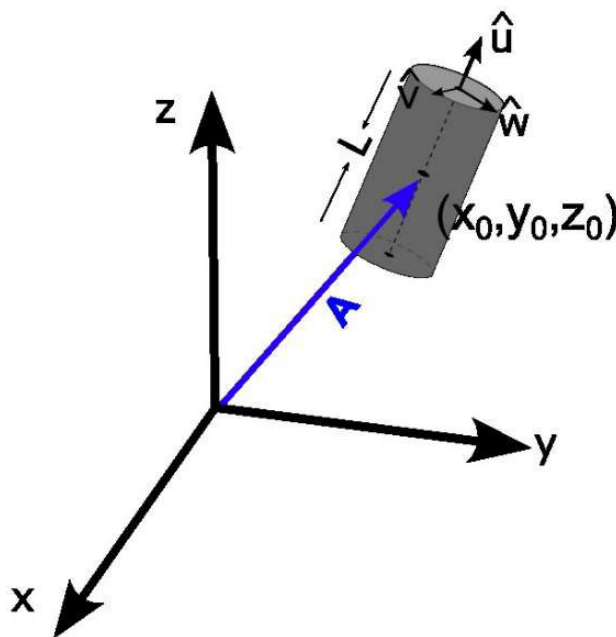


Figure VI.1. Physical parameters that need to be provided to the program in order to place the spherocylinders inside a cubic box of determined dimensions.

To accomplish the process described above, we take the value of the coordinates of the $\hat{\mathbf{u}}$ vector for each spherocylinder obtained from the Monte Carlo simulations. Now, to find the coordinates of the other two vectors, \mathbf{V} and \mathbf{W} , we proceed as follows according to the next cases. If the three coordinates of the vector $\hat{\mathbf{u}}$ are different from zero, we generate two random values between 0 and 1. These values will be assigned to V_x and V_y of the \mathbf{V} vector. For the remaining coordinate, V_z , the value is obtained by imposing the perpendicular condition given by

$$u_x V_x + u_y V_y + u_z V_z = 0 \quad (\text{VI. 1})$$

Having assigned the values of the components V_x and V_y the value of V_z can be calculated by the following

$$V_z = -\frac{U_x V_x + U_y V_y}{U_z} \quad (\text{VI. 2})$$

In the case that one of the coordinates of the vector $\hat{\mathbf{u}}$ vanishes, then, finding the vector \mathbf{V} is straightforward.

We still need to generate the \mathbf{W} vector. To do this, we use the cross product as

$$\mathbf{W} = \hat{\mathbf{u}} \times \mathbf{V} \quad (\text{VI. 3})$$

As mentioned above the lengths of the vectors \mathbf{V} and \mathbf{W} which will define the diameters in their corresponding directions, which will be denoted as D_V and D_W , respectively. Therefore, we adjust their magnitudes as follows.

$$|\mathbf{V}| = D_V \quad (\text{VI. 4a})$$

$$|\mathbf{W}| = D_W \quad (\text{VI. 4b})$$

As an illustration, the parameters of the vectors $\hat{\mathbf{u}}$, \mathbf{V} and \mathbf{W} corresponding to a rod centered at the origin, pointing in z direction, with length $L=6$ and diameter 1, will be

$$\hat{\mathbf{u}} = (0,0,1); L = 6; \mathbf{V} = 1,0,0; \mathbf{W} = (0,0,1)$$

Using the previews parameters the program will exhibit the following image.

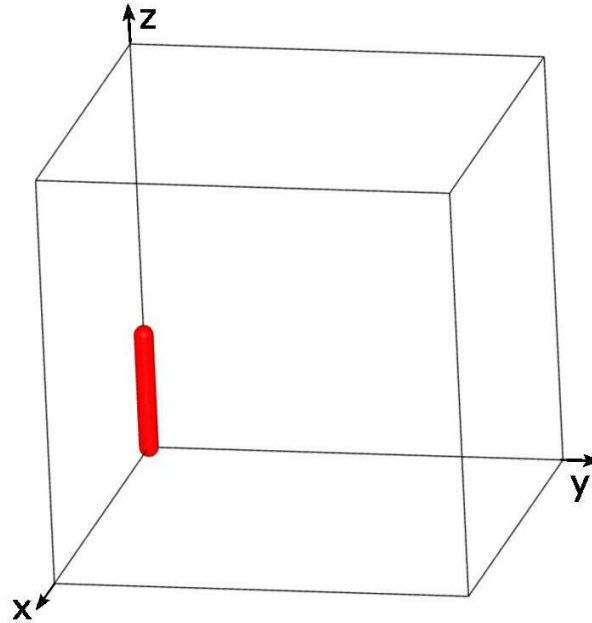


Figure VI.2. Spherocylinder exhibited by the program using the above parameters.

In figure VI.2 we have introduced a box of lengths $23 \times 23 \times 23$ units.

As in our calculations the direction of the dipoles is considered, it is necessary to visually indicate the direction of the rods. To depict this direction, we will indicate by means of red and blue colors, the positive and the negative charges of the dipoles, respectively. This is accomplished as follows.

To accomplish this, we will draw two overlapped cylinders, displaced a small distance Δ one with respect to the other in the \hat{u} direction, creating the illusion of a single spherocylinder, showing the two mentioned colors.

To accomplish the above task, we will refer to figure VI.3.

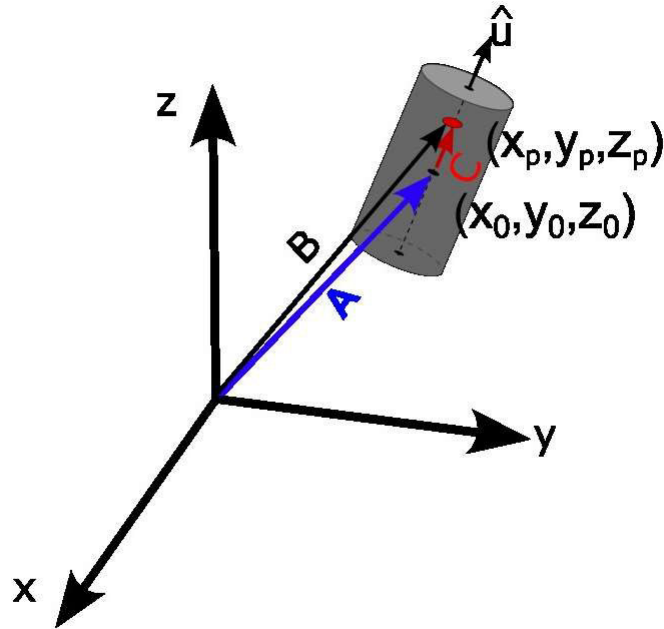


Figure VI.3. Displacement of the rod from the position (X_0, Y_0, Z_0) to the new position (X_p, Y_p, Z_p) , in the direction of $\hat{\mathbf{u}}$

To displace one of the cylinders a quantity Δ in the direction of the vector $\hat{\mathbf{u}}$ from the point (X_0, Y_0, Z_0) , pointed by vector \mathbf{A} to the new position (X_p, Y_p, Z_p) , pointed by vector \mathbf{B} , as depicted in the figure VI.3, we define a new vector \mathbf{C} , of magnitude Δ , pointing in the direction of $\hat{\mathbf{u}}$, as

$$\mathbf{C} = \Delta \hat{\mathbf{u}} \quad (\text{VI. 5})$$

From the figure we notice the following relation between the three vectors

$$\mathbf{A} + \mathbf{C} = \mathbf{B} \quad (\text{VI. 6})$$

From equation (VI.6) we then observe that to displace the rod a distance Δ in the direction of $\hat{\mathbf{u}}$ we only need to add to the initial point (X_0, Y_0, Z_0) the components of the new vector \mathbf{C} as

$$\mathbf{B} = (X_0 + \Delta u_x, Y_0 + \Delta u_y, Z_0 + \Delta u_z) \quad (\text{VI. 7})$$

Now, we need to displace the other spherocylinder a distance Δ in the $\hat{\mathbf{u}}$ direction. Therefore, the negative charged part of the rod, will be given accordingly by a vector \mathbf{B}' as

$$\mathbf{B}' = (X_0 - \Delta u_x, Y_0 - \Delta u_y, Z_0 - \Delta u_z) \quad (\text{VI. 8})$$

As an example of the above procedure, in figure VI.4, we exhibit two displaced spherocylinders, slightly overlapped, one blue and the other red, giving the above mentioned desired illusion.

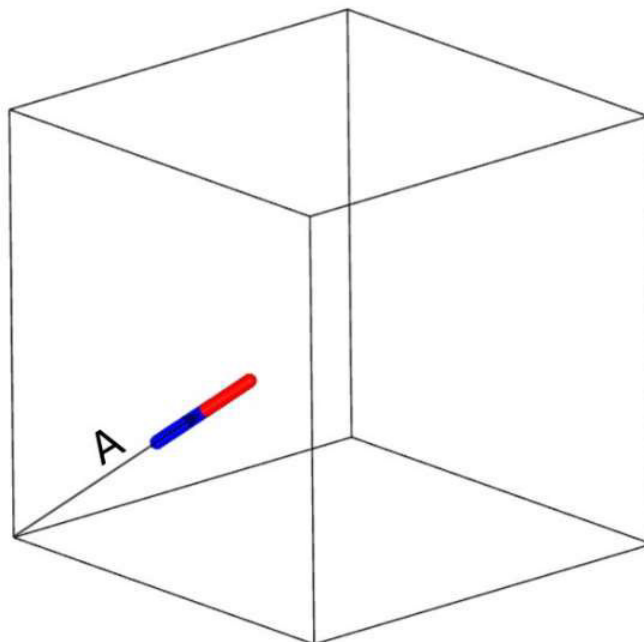


Figure VI.4. Two displaced spherocylinders slightly overlapped, one blue and other red, giving the illusion of only one rod exhibiting two colors.

The method described in this section will allow us to show our results showing the dipolar direction of each rod as will be shown in the results section. The following figure shows a preliminary illustration applied to 1000 rods.

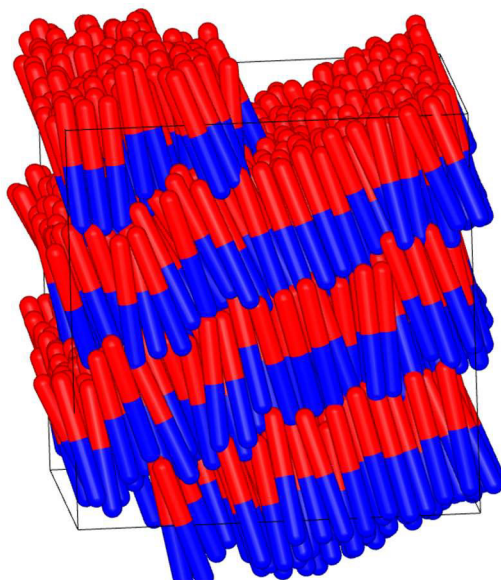


Figure VI.5. Snapshot of 1000 rods applying the described method to represent the dipoles orientation. The red half represents the positive part of the dipole, while the blue half represents the negative part, illustrating the scheme used to visualize dipoles in the simulation.

9.1 Bibliography

- [1.1] Talapin, D. V., Lee, J.-S., Kovalenko, M. V., & Shevchenko, E. V. (2010). Prospects of colloidal nanocrystals for electronic and optoelectronic applications. *Chemical Reviews*, 110(1), 389–458.ss
- [1.2] Sacanna, S., Pine, D. J., & Yi, G.-R. (2013). Engineering shape: The novel geometries of colloidal self-assembly. *Soft Matter*, 9(30), 8096-8106.
- [1.3] Fraden, S., Maret, G., Caspar, D. L. D., & Meyer, R. B. (1989). Isotropic-nematic phase transition and angular correlations in suspensions of virus particles. *Physical Review Letters*, 63(19), 2068-2071.
- [1.4] Dogic, Z., & Fraden, S. (2006). Ordered phases of filamentous viruses. *Current Opinion in Colloid & Interface Science*, 11(1), 47-55.
- [1.5] Huber, L., Suzuki, R., Krüger, T., Frey, E., & Bausch, A. R. (2018). Emergent complexity of the cytoskeleton: From single filaments to tissue mechanics. *Science*, 361(6403), 255-260.
- [1.6] Ermak, D. L., & McCammon, J. A. (1978). Brownian dynamics with hydrodynamic interactions. *The Journal of Chemical Physics*, 69(4), 1352-1360
- [1.7] Frazier, Z., & Alber, F. (2012). A computational approach to increase time scales in Brownian dynamics-based reaction-diffusion modeling. *Journal of Computational Biology*, 19(6), 606–618.
- [1.8] Berthier, L. (2007). Revisiting the slow dynamics of a silica melt using Monte Carlo simulations. *Physical Review E*, 76(1), 011507
- [1.9] Ramos, L., & Cipelletti, L. (2001). Ultraslow dynamics and stress relaxation in the aging of a soft glassy system. *Physical Review Letters*, 87(24), 245503.
- [1.10] Lee, J. S. S. L., Teoh, J. X. T., Ling, A. L. O., Chong, J., Loo, Y. S., Azmi, I. D. M., Zahid, N. I., Bose, R. J. C., & Maheshwaran, T. (2023). Recent advances in the development of liquid crystalline nanoparticles as drug delivery systems. *Pharmaceutics*, 15(5), 1421
- [1.11] Mao, Y., Nielsen, P., & Ali, J. (2022). Passive and active microrheology for biomedical systems. *Frontiers in Bioengineering and Biotechnology*, 10, 916354.
- [1.12] Squires, T. M., & Mason, T. G. (2010). Fluid Mechanics of Microrheology. *Annual Review of Fluid Mechanics*, 42, 413-438
- [1.13] Wehrman, M. D., Mistrely, M. J., Lindberg, S., & Schultz, K. M. (2018). Combining microfluidics and microrheology to determine rheological properties of soft matter during repeated phase transitions. *Journal of Visualized Experiments*, 134, 57429

- [2.1] Dhont, J. K. G. *An Introduction to Dynamics of Colloids*. van 't Hoff Laboratory for Physical and Colloid Chemistry, University of Utrecht, Utrecht, The Netherlands.
- [2.2] Mokrushin, S. (1962). Thomas Graham and the Definition of Colloids. *Nature*, 195, 861. <https://doi.org/10.1038/195861a0>
- [2.3] Norde, W. *Colloids and Interfaces in Life Sciences*. Wageningen University, Wageningen and University of Groningen, Groningen, The Netherlands.
- [2.4] de Gennes, P. G., & Prost, J. (1993). *The Physics of Liquid Crystals* (2nd ed.). Oxford University Press.
- [2.5] Chandrasekhar, S. F.R.S. (1993). *Liquid Crystals*. Cambridge University Press.
- [2.6] Chaikin, P. M., & Lubensky, T. C. (1995). *Principles of Condensed Matter Physics*. Cambridge University Press.
- [2.7] Bahadur, B. (1992). *Liquid Crystals: Applications and Uses*, Vol. 3.
- [2.8] Collings, P. J., & Hird, M. (1997). *Introduction to Liquid Crystals: Chemistry and Physics*. London: Taylor & Francis.
- [2.9] A. G. Chmielewski (1086). *Viscosity Coefficients of Some Nematic Liquid Crystals. Molecular Crystals and Liquid Crystals*, vol. 132, no. 3-4, pp. 339-352, 1986.
- [2.10] Orr, R., & Pethrick, R. A. (2011). *Viscosity coefficients of nematic liquid crystals: I. Oscillating plate viscometer measurements and rotational viscosity measurements: K15. Liquid Crystals*, 38(9), 1169–1181
- [2.11] Sluckin, T. J., Dunmur, D. A., & Stegemeyer, H. (2004). *Crystals That Flow: Classic Papers from the History of Liquid Crystals*. Taylor & Francis.
- [2.12] Gray, G. W., & Goodby, J. W. (1984). *Smectic Liquid Crystals: Textures and Structures*. Leonard Hill
- [2.13] Brock, J. D., Birgeneau, R. J., & Litster, J. D. (1989). Hexatic ordering in liquid crystal films. *Contemporary Physics*, 30(5), 321-340.
- [2.14] Dierking, I. (2003). *Textures of Liquid Crystals*. Wiley-VCH.
- [2.15] Zannoni, C. (2022). *Liquid Crystals and Their Computer Simulations*. Cambridge University Press
- [2.16] Hänggi, P., & Marchesoni, F. (2005). Introduction: 100 years of Brownian motion. *Chaos*, 15(2), 026101

- [2.17] Karatzas, I., Shreve, S.E. (1998). Brownian Motion. In: Brownian Motion and Stochastic Calculus. Graduate Texts in Mathematics, vol 113. Springer, New York, NY
- [2.18] Chowdhury, D. (2005). 100 years of Einstein's theory of Brownian motion: From pollen grains to protein trains —2. *Resonance*, 10, 42-54
- [2.19] Einstein, A. (1905). Über die von der molekularkinetischen Theorie der Wärme geforderte Bewegung von in ruhenden Flüssigkeiten suspendierten Teilchen. *Annalen der Physik*, 322(8), 549-560.
- [2.20] Atkins, P., & De Paula, J. (2010). *Physical Chemistry* (9th ed.).
- [2.21] Landau, L. D., & Lifshitz, E. M. (1958). *Statistical Physics*. Pergamon, London.
- [2.22] McQuarrie, D. (1976). *Statistical Mechanics*. Harper & Row.
- [2.23] García Colin, L. (1990). *Introducción a la Termodinámica Clásica* (4th ed.).
- [2.24] Stidham, H. D. *Statistical Thermodynamics for Beginners*. University of Massachusetts Amherst, World Scientific Publishing Co.
- [3.1] McQuarrie, D. (1976). *Statistical Mechanics*. Harper & Row.
- [3.2] Metropolis, N., Rosenbluth, A. W., Rosenbluth, M. N., Teller, A. H., & Teller, E. (1953). Equation of state calculations by fast computing machines. *Journal of Chemical Physics*.
- [3.3] Navarro, D. J. *Notes from a data witch - The Metropolis-Hastings algorithm*. djenavarro.net.
- [3.4] Ritvik Math. (n.d.). [YouTube Video].
https://www.youtube.com/watch?v=yCv2N7wGDCw&ab_channel=ritvikmath.
- [3.5] Allen, M. P., & Tildesley, D. J. (1987). *Computer Simulation of Liquids*. Oxford: Oxford University Press.
- [3.6] Landau, D. P. (2015). *A Guide to Monte Carlo Simulations in Statistical Physics* (4th ed.). Cambridge University Press.
- [3.7] Frenkel, D., & Smit, B. (2001). *Understanding Molecular Simulation: From Algorithms to Applications* (2nd ed.). Computational Science Series Vol. 1.
- [3.8] Löwen, H. (1994). Brownian dynamics of hard spherocylinders. *Physical Review E*, 50(2), 1232
- [3.9] Patti, A., & Cuetos, A. (2012). *Phys. Rev. E*, 86, 011403.
- [3.10] Vega, C., & Lago, S. (1994). *Computers & Chemistry*, 18, 55.

- [3.11] Cueto, A., & Haya, J. (2014). *Liquid crystal phase diagram of soft repulsive rods and its mapping on the hard repulsive reference fluid*.
- [3.12] de Gennes, P. G., & Prost, J. (1993). *The Physics of Liquid Crystals* (2nd ed.). Oxford: Clarendon Press.
- [3.13] Helfrich, W. (1978). "Smectic-A phases of liquid crystals: Static and dynamic properties." *Physical Review Letters*, 41(12), 712-715.
- [3.14] M. Chiappini, A. Patti, and M. Dijkstra, *Phys. Rev. E* 102, 040601 (2020).
- [3.15] F. A. García Daza, A. Cuetos, and A. Patti, *Phys. Rev. E* 102, 013302 (2020).
- [3.16] F. A. García Daza, A. M. Puertas, A. Cuetos, and A. Patti, *Journal of Colloid and Interface Science* 605, 182 (2022).
- [3.17] Avalos, Josep & Rubi, J. & Bedeaux, Dick & Van der Zwan, Gert. (1994). Friction coefficients of axisymmetric particles in suspension. *Physica A Statistical and Theoretical Physics*. 211. 193-217. 10.1016/0378-4371(94)00176-6.
- [4.1] Janmey, P. A., & Schliwa, M. (2008). Rheology. *Current Biology*, 18(15), R639–R641.
- [4.2] Cicuta, P & Donald, M (2007) Microrheology: a review of the method and applications.
- [4.3] García Daza, F. A., Puertas, A. M., Cuetos, A., & Patti, A. (2022). Microheology of colloidal suspensions via dynamic Monte Carlo simulations. *Journal of Colloid and Interface Science*, 605, 182-192.
- [4.4] Mason, T. G. (2006). Rheology of soft materials. *Boulder School for Condensed Matter and Materials Physics Lecture Notes*.
- [4.5] Ramli, H., Zainal, N. F. A., Hess, M., & Chan, C. H. (2022). Basic principle and good practices of rheology for polymers for teachers and beginners. *Chemistry Teacher International*, 4(4), 307–326
- [4.6] Bird, RB, Armstrong RC, Hassager O (1977) Dynamics of polymeric liquids. Wiley, New York
- [4.7] Mason, T. G. (2000). Estimating the viscoelastic moduli of complex fluids using the generalized Stokes-Einstein equation.
- [4.8] García Daza, F. A., Puertas, A. M., Cuetos, A., & Patti, A. (2022). Microrheology of isotropic and liquid-crystalline phases of hard rods by dynamic Monte Carlo simulations.

- [5.1] Frenkel, D., & Smit, B. (2001). *Understanding Molecular Simulation: From Algorithms to Applications* (2nd ed.).
- [5.2] Sadus, R. J. (2004). *Molecular Simulation of Fluids: Theory, Algorithms, and Object-Oriented*.
- [5.3] Reitz, J. R., & Milford, F. (n.d.). 2d ed, pp 36-39, *Addison Wesley*.
- [5.4] S. W. de Leeuw, J. W. Perram, and E. R. Smith, (1980) "Simulation of Electrostatic Systems in Periodic Boundary Conditions. I. Lattice Sums and Dielectric Constants," Proceedings of the Royal Society of London. Series A, Mathematical and Physical Sciences, vol. 373, no. 1752, pp. 27–56
- [5.5] Gil-Villegas, A., McGrother, S. C., & Jackson, G. (1997). Reaction-field and Ewald summation methods in Monte Carlo simulations of dipolar liquid crystals.
- [5.6] S. C. McGrother, D. C. Williamson, and G. Jackson, *J. Chem. Phys.* 104, 6755 (1996).
- [5.7] S. C. McGrother, A. Gil-Villegas, and G. Jackson, *Mol. Phys.* 95, 657 (1998).
- [6.1] Cywiak, D., Gil-Villegas, A., & Patti, A. (2022). Long-time relaxation dynamics in nematic and smectic liquid crystals of soft repulsive colloidal rods. *Physical Review E*, 105(1).
- [6.2] Morillo, N., Patti, A., & Cuetos, A. (2019). Long-time self-diffusion in monolayers of dipolar hard spheres. *The Journal of Chemical Physics*, 150(20), 204905.
- [6.3] Cuetos, A., & Martínez-Haya, B. (2015). Structural properties of liquid crystals of hard helices. *Molecular Physics*, 113(9-10), 1137-1145.
- [6.4] Lettinga, M. P., Barry, E., & Dogic, Z. (2005). Self-diffusion of rod-like viruses in the nematic phase. *EPL (Europhysics Letters)*, 71(5), 692-698.
- [6.5] Cifelli, M., Cinacchi, G., & De Gaetani, L. (2006). Structure and dynamics of a biaxial liquid crystal from molecular dynamics simulations. *The Journal of Chemical Physics*, 125(16), 164912.
- [6.6] van Roij, R., Bolhuis, P., Mulder, B., & Frenkel, D. (1995). Transverse interlayer order in lyotropic smectics. *Physical Review E*, 52(2), R1277-R1280.
- [6.7] Duijneveldt, J. S., & Allen, M. P. (1997). Computer simulations of freely rotating hard ellipsoids. *Molecular Physics*, 90(2), 243-253.
- [6.8] Lettinga, M. P., & Grelet, E. (2007). Self-diffusion of rod-like viruses in the nematic phase. *Physical Review Letters*, 99(19), 197802. <https://doi.org/10.1103/PhysRevLett.99.197802>

- [6.9] Bier, M., van Roij, R., Dijkstra, M., & van der Schoot, P. (2008). Self-assembly of rodlike particles into smectic phases: The role of attractive interactions. *Physical Review Letters*, *101*(21), 215901.
- [6.10] Patti, A., El Masri, D., van Roij, R., & Dijkstra, M. (2009). Influence of external fields on the structure and dynamics of colloidal liquid crystals. *Physical Review Letters*, *103*(24), 248304.
- [6.11] Patti, A., El Masri, D., van Roij, R., & Dijkstra, M. (2010). Smectic phase formation in suspensions of colloidal rods. *The Journal of Chemical Physics*, *132*(22), 224907.
- [6.12] Brambilla, G., El Masri, D., Pierno, M., Berthier, L., Cipelletti, L., Petekidis, G., & Schofield, A. B. (2009). Probing the ideal glass transition in colloidal suspensions. *Physical Review Letters*, *102*(8), 085703.
- [6.13] Matena, R., Dijkstra, M., & Patti, A. (2010). Smectic and columnar phases in rods: A Monte Carlo study. *Physical Review E*, *81*(2), 021704.
- [6.14] Belli, S., Patti, A., van Roij, R., & Dijkstra, M. (2010). Polydispersity effects in suspensions of colloidal platelets. *The Journal of Chemical Physics*, *133*(15), 154514.
- [7.1] Gil-Villegas, A., & Jackson, G. (1997). *Phase behavior of dipolar hard rod fluids*. *Molecular Physics*, *92*(2), 303–315.
- [7.2] Janmey, P. A., & McCulloch, C. A. (2007). *Cell mechanics: Integrating cell responses to mechanical stimuli*. *Annual Review of Biomedical Engineering*, *9*, 1–34.
- [7.3] Vanakaras, A. G., & Photinos, D. J. (1995). *Electric dipoles and phase stability in nematic liquid crystals*. *Molecular Physics*, *85*(6), 1089–1104.
- [7.4] Weis, J. J., Levesque, D., & Zarragoicoechea, G. J. (1993). Effect of dipolar interactions on orientational order in hard ellipsoids. *Molecular Physics*, *80*(5), 1005–1014.
- [7.5] Weis, J. J., Levesque, D., & Zarragoicoechea, G. J. (1992). *Structural and dielectric properties of dipolar hard ellipsoids: A Monte Carlo study*. *Molecular Physics*, *80*(5), 1005–1018.
- [7.6] Photinos, D. J., & Samulski, E. T. (1993). *Electric dipole interactions of chain molecules in nematics: The analysis of segmental ordering in α,ω -dibromoalkanes*. *The Journal of Chemical Physics*, *98*(12), 10009–10016. <https://doi.org/10.1063/1.464858>
- [7.7] Fujii, S., Yamanaka, J., & Yokoyama, H. (2017). Structural Rheology of the Smectic Phase. *Frontiers in Materials*, *4*, 19.
- [8.1] Hermes, M. *Viscol*. <https://michihermes.github.io/viscol/>



León Guanajuato a 15 de noviembre del 2024.
Asunto: Aprobación de Tesis doctorado en Física

DR. MODESTO ANTONIO SOSA AQUINO
DIRECTOR DE LA DIVISIÓN DE CIENCIAS E INGENIERÍAS
UNIVERSIDAD DE GUANAJUATO
PRESENTE

Estimado Director:

Por este conducto me permito informarle que he leído minuciosamente la tesis titulada "Effect of long-range interactions in dynamic and transport properties of liquid crystals using DMC simulations and the reaction field method" desarrollada por **M. en F. Daniela Cywiak Córdova** para obtener el grado de Doctora en Física y dirigida por el Dr. Alejandro Gil-Villegas Montiel. Sin duda alguna, la tesis cumple a cabalidad los aspectos deseados en un trabajo de este nivel, por lo que me permito recomendar que **Daniela Cywiak** realice la defensa pública de su trabajo de tesis.

Sin más por el momento, reciba un cordial saludo.

ATENTAMENTE

Dr. Alejandro Martínez Borquez
Director del Departamento de Ciencias, Noroeste
alejandro.martinez.borquez@tec.mx
Phone number: +52 4774099288
Escuela de Ingeniería y Ciencias, Campus León,
Tecnológico de Monterrey

Campus León Eugenio Garza Sada S/N Col. Cerro Gordo, 37190, León, Gto. México



UNIVERSIDAD
DE GRANADA

Dr. Alessandro Patti
Departamento de Física Aplicada
Instituto Carlos I de Física Teórica y Computacional
Universidad de Granada
Av. Fuentenueva s/n, 18071 Granada, España
e-mail: apatti@ugr.es

A la atención del Dr. Modesto Antonio Sosa Aquino, Director de la División de Ciencias e Ingenierías, Universidad de Guanajuato.

En mi calidad de jurado evaluador del trabajo de tesis de la Maestra en Ciencias (Física) Daniela Cywiak Córdova, titulado *“Effect of long-range interactions in dynamic and transport properties of liquid crystals using DMC simulations and the reaction field method”*, me permito comunicarle que estoy de acuerdo en que la estudiante solicite la defensa de dicha tesis.

Considero que el trabajo realizado por Daniela durante su doctorado es de alta calidad y relevancia científica, por lo que reúne los méritos necesarios para proceder con la etapa de defensa.

Sin otro asunto que tratar por el momento, agradezco de antemano su atención y aprovecho la ocasión para enviarle un cordial saludo.

Atentamente,

PATTI
ALESSANDRO
- X5332172J

Digitally signed by
PATTI ALESSANDRO -
X5332172J
Date: 2025.04.07
18:21:17 +02'00'

En Granada, 7 de abril de 2025

Departamento de Física Aplicada, Universidad de Granada
Av. Fuentenueva s/n, 18071 Granada, España
Tel. (0034) 958.248.530
<https://fisicaaplicada.ugr.es>



Dr. Modesto A. Sosa Aquino

Director de la División de Ciencias e Ingenierías

Universidad de Guanajuato

PRESENTE

ASUNTO: Carta aval de Sinodal

León, Gto. noviembre 15, 2024

Por medio del presente hago constar que he revisado la tesis titulada: **“Effect of long-range interactions in dynamic and transport properties of liquid crystals using DMC simulations and the reaction field method”** que presenta la M. F. Daniela Cywiak Córdova para obtener el grado de Doctor en Física, dicho trabajo fue dirigido por el Dr. Alejandro Gil-Villegas Montiel y co-dirigido por el Dr. Alessandro Patti.

Le comunico que he discutido cuidadosamente dicha tesis con la sustentante, a quien le he hecho llegar mis comentarios y correcciones. Le expreso además que en lo general me parece un buen trabajo por lo que avalo su presentación.

Sin más por el momento aprovecho para enviarles un cordial saludo.

ATENTAMENTE

A handwritten signature in blue ink, appearing to read 'Miguel Ángel Vallejo Hernández', written over a horizontal line.

Dr. Miguel Ángel Vallejo Hernández

DEPARTAMENTO DE INGENIERÍA FÍSICA

DIVISION DE CIENCIAS E INGENIERIAS, CAMPUS LEÓN

Lomas del Bosque 103, Fracc. Lomas del Campestre, C.P. 37150 León, Gto., México Tel. (477) 788-5100



Guanajuato, Gto. 15 de noviembre de 2024

Dr. Modesto A. Sosa Aquino
Director de la División de Ciencias e Ingenierías
Campus León, Universidad de Guanajuato

Estimado Dr. Sosa Aquino:

Por medio de la presente le informo que he leído y discutido ampliamente el trabajo de tesis titulado "**Effect of long-range interactions in dynamic and transport properties of liquid crystals using DMC simulations and the reaction field method**", presentada para obtener el grado de Doctora en Física por la *M. en F. Daniela Cywiak Córdova*. El director de la tesis es el Dr. Alejandro Gil-Villegas Montiel, siendo co-director el Dr. Alessandro Patti.

En este trabajo de tesis se investigaron las propiedades dinámicas, el relajamiento estructural y la reología de cristales líquidos en general empleando la técnica Monte Carlo dinámico. En particular, se puso especial énfasis en los efectos que las interacciones dipolares de largo alcance tienen sobre las propiedades viscoelásticas de cristales líquidos.

Los resultados de este trabajo son de interés para una amplia comunidad de investigadores en diferentes áreas relacionadas con la fisicoquímica y el modelaje molecular de cristales líquidos.

Basado en lo anterior, le informo que no tengo ningún inconveniente para que se lleve a cabo la defensa de la tesis en la fecha y hora que se determine.

Sin otro particular, me despido enviándole un cordial saludo.

A T E N T A M E N T E:

Dr. Antonio Martínez Richa
 Profesor Titular C



Departamento de Química
 Noria alta s/n
 Guanajuato, Gto. 36050
 MEXICO



Tel: +52 (473)7320006 and 7326885
 Ext. 1411 and 8135
 Fax: +52 (473)7326885 Ext. 8106
 e-mail: richa@ugto.mx



Noviembre 11, 2024

Director Dr. Modesto A. Sosa Aquino
División de Ciencias e Ingenierías
Universidad de Guanajuato

Estimado Dr. Sosa Aquino:

Por medio de este conducto le informo que he leído y discutido ampliamente el trabajo de tesis titulado "**Effect of long-range interactions in dynamic and transport properties of liquid crystals using DMC simulations and the reaction field method.**" desarrollado por la **M. en F. Daniela Cywiak Córdova** para obtener el grado de Doctora en Física y dirigido por el Dr. Alejandro Gil-Villegas Montiel y co-dirigido por el Dr. Alessandro Patti. En el trabajo de tesis, Daniela investigó las propiedades dinámicas, el relajamiento estructural y la reología de cristales líquidos mediante la aplicación de la técnica denominada Monte Carlo dinámico. En particular, puso énfasis en los efectos que las interacciones dipolares de largo alcance tienen sobre las propiedades viscoelásticas de cristales líquidos. Este trabajo resulta de interés e impacto para la comunidad de física estadística. Finalmente, quiero comentarle que estoy satisfecho con el contenido de la tesis, los resultados obtenidos y, principalmente, por el conocimiento adquirido y generado por Daniela, por lo que no tengo ningún inconveniente para que se lleve a cabo la defensa de la tesis.

Sin otro particular por el momento, me despido enviándole un cordial saludo.

Atentamente,
"La Verdad Os Hará Libres"

A handwritten signature in blue ink, appearing to read 'Ramón Castañeda Priego'.

Dr. Ramón Castañeda Priego
Profesor Titular C

DEPARTAMENTO DE INGENIERÍA FÍSICA
Lomas del Bosque #103,
Lomas de Campestre, León Gto.
C.P. 37150
(477) 788 5100 Ext. 8411 y 8462
Fax. Ext. 8410
www.depif.ugto.mx



Dear *Dr. Sosa Aquino*,

I am writing to formally approve the submission of the Ph.D. dissertation titled “*Effect of long-range interactions in dynamic and transport properties of liquid crystals using DMC simulations and the reaction field method*” authored by *M. en F. Daniela Cywiak Córdova*, as a requirement for the fulfillment of the degree of Doctor of Philosophy in Physics. This dissertation has been conducted under the supervision of *Dr. Alejandro Gil-Villegas Montiel* and co-supervisor *Dr. Alessandro Patti*.

Daniela has demonstrated exceptional commitment, scientific rigor, and intellectual independence in conducting this work. The research presented thoroughly study and analyze the dynamic and rheological properties of different liquid crystal phases through molecular simulation using Montecarlo and other advanced modeling techniques, making significant contributions to the field of soft matter.

I have reviewed the dissertation in detail and discussed its content extensively with Daniela. I am confident that it meets the highest academic and research standards expected of a doctoral-level study. Therefore, I fully support its submission and recommend it for examination.

If you have any questions or require further information, please do not hesitate to contact me.

Sincerely,

Pedro Coutino-Soto, PhD
VP of Technology
Alphamicro Inc.
1950 State Route 59 Suite 100,
Kent OH, 44240, USA.

UNIVERSIDAD DE
GUANAJUATO

León, Guanajuato, a 15 de noviembre de 2024

Dr. Modesto Antonio Sosa Aquino
Director de la División de Ciencias e Ingenierías
Presente

En mi calidad de jurado para evaluar el trabajo de tesis de la **M. en F. Daniela Cywiak Córdova**, titulado **“Effect of long-range interactions in dynamic and transport properties of liquid crystals using DMC simulations and the reaction field method”**, me permito comunicarle mi anuencia para que la estudiante solicite la defensa de la tesis referida considerando la relevancia y calidad del trabajo que Daniela realizó durante su doctorado.

Sin otro particular que tratar por el momento, agradezco su atención a la presente y me despido enviándole un cordial saludo.

ATENTAMENTE**“La Verdad Os Hará Libres”**

Dr. José Jorge Delgado García
Profesor Titular “A”
División de Ciencias e Ingenierías
Universidad de Guanajuato Campus León
jorgedel@ugto.mx

División de Ciencias e Ingenierías Campus León
Loma del Bosque 103, Col. Lomas del Campestre, León, Gto., CP 37150
Tel. (477) 788 5100 ext. 3866
www.dci.ugto.mx